

ACARP

Australian Coal Association Research Program

ACARP PROJECT C13029

INTEGRATED P-WAVE/PS-WAVE SEISMIC IMAGING FOR IMPROVED GEOLOGICAL CHARACTERISATION OF COAL ENVIRONMENTS

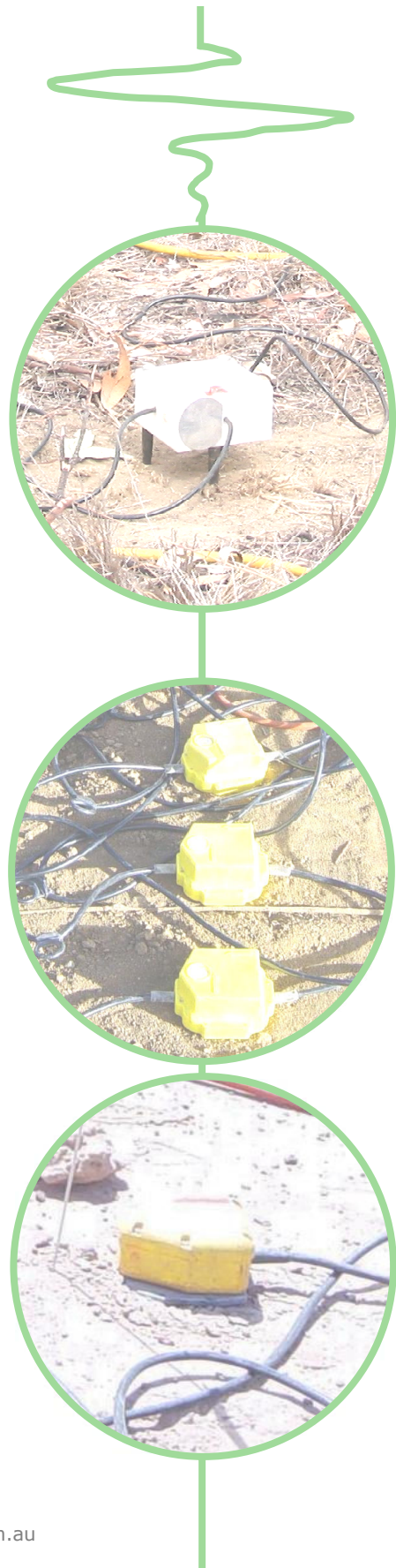
FINAL REPORT
February 2007

Natasha Hendrick
Velseis Pty Ltd



*Integrated Seismic
Technologies*

Velseis Pty Ltd ABN 56 009 809 544
83 Jijaws Street (PO Box 118), Sumner Park, Queensland 4074
Ph: (617) 3376 5544 Fax: (617) 3376 6939 Email: velseis@velseis.com.au



DISCLAIMER

No person, corporation or other organisation (“person”) should rely on the contents of this report and each should obtain independent advice from a qualified person with respect to the information contained in this report. Australian Coal Research Limited, its directors, servants and agents (collectively “ACR”) is not responsible for the consequences of any action taken by any person in reliance upon the information set out in this report, for the accuracy or veracity of any information contained in this report or for any error or omission in this report. ACR expressly disclaims any and all liability and responsibility to any person in respect of anything done or omitted to be done in respect of the information set out in this report, any inaccuracy in this report or the consequences of any action by any person in reliance, whether wholly or partly, upon the whole or any part of the contents of this report.

ABSTRACT

Converted-wave seismic reflection is a novel seismic method that takes advantage of the fact that when a compressional (P) wave from a conventional seismic source (e.g. dynamite, mini-SOSIE) strikes a coal seam, a significant fraction of the energy reflected back to the surface will be converted to shear (S) energy. Multi-component (3C) seismic acquisition measures both the vertical and horizontal components of ground motion at the surface to enable exploitation of both the P and converted P-to-S wave types. Over the past five years, Velseis Pty Ltd has been utilising this technology to yield both conventional P-wave and converted-wave (PS-wave) seismic images of coal seams in the Bowen Basin, Australia.

ACARP Project C10020 (completed June 2003) successfully demonstrated the viability of using converted-wave seismic technology to extract complimentary structural information about target coal seams. This project has focused on examining the lithological information that can be extracted from the integrated interpretation of P and PS data. One new 2D-3C seismic dataset has been acquired, to complement the two datasets previously acquired as part of project C10020. The project has also had access to a number of experimental commercial 3C datasets from the Bowen Basin. These data, together with a series of synthetic converted-wave seismic datasets, have undergone extensive analysis and interpretation to help improve our manipulation of PS seismic data, and determine the relevance and resolution of lithological information recoverable from integrated P/PS seismic interpretation.

Acquisition trials have demonstrated that improvements in our PS seismic sections can be achieved if geophones with a low natural frequency (e.g. 10 Hz or 14 Hz) are used for 3C seismic acquisition. Modifications to our S-wave receiver statics method, CCP-binning algorithm and post-stack noise removal techniques have significantly enhanced the outcomes of our converted-wave imaging. Integrated P/PS interpretation synthetic-data trials have demonstrated that, provided the width of a geological anomaly is greater than the lateral resolution limit of the seismic data, and the lithological variation is significant, the V_p/V_s attribute can give an indication of relative changes in lithology away from borehole locations. However, to date, real-data V_p/V_s analysis experiments have produced mixed results, and further validated trials are required to assess the robustness of this new interpretation tool. A preliminary test to quantify the behaviour of PS energy using the two horizontal components of data suggest that fast S-wave polarisations can be interpreted in terms of local stress fields, and may be useful for locating zones of intense fracturing or minor faulting that cannot be detected using standard seismic interpretation methods.

The overall outcomes of this project have been to enhance PS processing, obtain a greater understanding of the influence of geology on PS-wave propagation, and determine to what extent integrated P/PS interpretation can contribute to our geological knowledge of the sub-surface. The results achieved to date clearly demonstrate that joint use of P and PS sections recovers more geological detail than using P-wave data alone. It remains to be determined how useful this additional lithological information will be to mine-site operations.

EXECUTIVE SUMMARY

Over the past five years Velseis Pty Ltd has conducted the first experiments in Australia to utilise shallow, high-resolution multi-component seismic data and converted-wave technology to image coal seams. This research effort has been driven by the desire of the Australian coal industry to locate and characterise increasingly subtle structures, and enhance the remote geological characterisation of the sub-surface.

Converted-wave seismic reflection is a novel seismic method that takes advantage of the fact that when a compressional (P) wave from a conventional seismic source (e.g. dynamite, mini-SOSIE) strikes a coal seam, a significant fraction of the energy reflected back to the surface will be converted to shear (S) energy. Multi-component (3C) seismic recording measures both the vertical and horizontal components of ground motion to enable exploitation of both the P and converted P-to-S wave types.

ACARP Project C10020 (completed June 2003) successfully demonstrated the viability of using converted-wave seismic technology to yield complementary *structural* images of target coal seams. Project C13029 focuses on improving acquisition and processing methodology, and examining the *lithological* information that can be extracted from the integrated interpretation of P and PS data. One new 2D multi-component seismic dataset has been acquired, to complement the two datasets previously acquired as part of Project C10020. The project has also had access to a number of experimental commercial 3C datasets from the Bowen Basin. These data, together with a series of synthetic converted-wave seismic datasets, have undergone extensive analysis and interpretation to help improve our manipulation of PS seismic data, and determine the relevance and resolution of lithological information recoverable from integrated P/PS seismic interpretation.

Prior to the commencement of this project, all of our 3C seismic datasets had been acquired using geophones with a natural frequency of 40 Hz (i.e. geophone/recording-filter configuration designed to suppress energy with frequencies below 40 Hz). However, the evaluation of more-recently acquired 3C seismic datasets collected using geophone/recording-filter configurations designed to capture energy down to 10 Hz has demonstrated that strong PS signal can be recovered below 40 Hz. This low-frequency PS signal can help reduce the 'ringiness' of reflection events in PS sections that don't contain significant PS signal above 50 – 60 Hz.

It is common to observe anomalous asymmetric moveout of PS reflection events in common-conversion point (CCP) gathers. Investigation into PS-wave propagation behaviour indicates this is related to the sensitivity of S waves to lithological inhomogeneities in the sub-surface. In the case of extreme lateral inhomogeneities, PS reflection events can look significantly different on the positive- and negative-offset stacked PS sections. Recognition of this diodic behaviour of PS waves can assist with the recovery of additional lithological information from our converted-wave seismic data.

The evolution of a robust and efficient PS processing methodology is seen as a key to the future use of converted-wave seismic in the coal environment. This project has contributed to this essential objective through the development of a new S-wave receiver statics method. In addition, CCP-binning and post-stack noise attenuation algorithms have been enhanced. PS images derived for Trial #2 and Line C confirm that these advances have significantly improved the outcomes of our converted-wave imaging. However, processing results from Trials #2 and #3 indicate that we are losing considerable high-frequency PS information during the PS stacking process. There is growing evidence that this may be associated with our current approach of ignoring anisotropy in the sub-surface rather than poor S-wave receiver statics. Implementation of a CCP-binning scheme that accommodates anisotropy, in addition to utilising post-stack PS migration, is seen as a priority to help accommodate an inhomogeneous earth.

Re-processing of Trial Dataset #1 (acquired as part of Project C10020) has tested a new vector-processing method, referred to as Elastic Wavefield Decomposition (EWD). Application of EWD has helped focus the PS reflector and results in slightly better fault definition in the final PS image. However, this experiment has not incorporated the above-mentioned enhancements to the PS processing flow. Thus, the option to routinely use vector processing is still under consideration.

The data from Trial #2 (acquired as part of Project C10020) have been re-processed using our latest PS processing flow. The PS image is significantly improved. Most notably, the new S-wave receiver statics have not erroneously removed the two-way time (TWT) 'pull-up' believed to be associated with a shallow, thick sandstone unit extending part-way along the line. Despite the lower overall resolution of the Trial #2 PS stack compared to the conventional P stack, it contributes structural information along the survey line. Additional, broad-scale lithological information has been extracted via our first attempts at V_p/V_s analysis.

Trial Dataset #3 was acquired in 2005 at a Bowen Basin site characterised by lateral inhomogeneities and multiple coal seams. Despite the raw 3C data suggesting that the PS section would exhibit greater resolution than the P section, the final PS image shows significantly reduced high-frequency content and does not contribute structural information along the survey line. This loss of resolution during the PS stacking process is thought to be associated with our current approach of assuming an isotropic earth. Nevertheless, the PS data do contribute to the geological characterisation of the sub-surface. Diodic illumination signals that a lithological anomaly, interpreted to be a thick sandstone unit, exists at the right edge of the line. Further lithological detail along the line has been extracted via V_p/V_s analysis.

Interpretation trials using synthetic 3C seismic data demonstrate that V_p/V_s interpretation of coal-seismic data is unlikely to recover absolute P-wave to S-wave velocity ratios (or equivalently, Poisson's Ratio). However, it is possible to get an accurate indication of relative lateral variations in lithology provided that P and PS reflection events can be accurately correlated, the width of a geological anomaly is greater than the lateral resolution limit of the seismic data, and lithological variations are significant (e.g. sandstone vs shale rather than subtle lithology changes within one rock type.)

Real-data V_p/V_s interpretation can avoid spurious interpretation results associated with processing artefacts, seismic noise and structures by using only strong coal-seam reflection events and smoothed TWT horizons, and not reading significance into the V_p/V_s attribute about structures or when amplitude variations are very small. V_p/V_s analysis results from Trials #2 and #3 are inconclusive, but suggest that integrated P/PS processing may be able to identify broad geological trends involving significant lithological variation. However, V_p/V_s interpretation cannot extract high-resolution geological detail about the roof and floor of a coal seam. Thus, it remains to be seen whether V_p/V_s analysis can contribute positively to mine design and planning.

Irregular occurrences of coherent PS reflection energy are observed on the crossline components of our 3C data. This crossline PS energy is believed to be the result of shear-wave splitting (SWS) caused by anisotropy in the sub-surface. A preliminary attempt at SWS analysis of a small portion of Line C indicates that the dominant orientation of the local anisotropic fabric is approximately $\pm 10^\circ$ from the inline direction. This is consistent with the fact that dominant thrust structures in the area run perpendicular to the 2D line. An attempt to correlate variations in this general orientation trend with local structures has proven inconclusive. In addition, no useful information could be extracted from the corresponding fast and slow S travel-time delay curve. Further work is recommended to establish the significance of the crossline PS energy we observe.

This project has contributed to improvements in our PS processing methodology and gives an indication of the ability of integrated P/PS interpretation to yield lithological information (i.e. geological details such as rock type, fracturing etc) away from borehole locations. Future research should focus on the continued development of PS processing algorithms – specifically anisotropic CCP binning and PS migration – to improve the resolution and integrity of our PS sections. Subsequent structural and lithological interpretation results are expected to become more robust with improved PS imaging. Higher-resolution PS images may also lend themselves to new and improved integrated interpretation procedures capable of extracting further geological detail from the sub-surface.

Acknowledgements

Velseis Pty Ltd would like to acknowledge that this work could not have been conducted without the support of the Australian Coal Association Research Program (ACARP) and the Australian coal industry. In particular, we thank Anglo Coal Australia Pty Ltd, BMA Coal Operations Pty Ltd, Xstrata Coal – NCA Project (Newlands Mine), and the Bowen Basin Geologists Group. Individuals who have assisted with this research project include: Andrew Willson, Doug Dunn, Mike Reveleigh, Rob Swann, Max Ayliffe, Tim McNally, Shaun Strong, Helen Richmond, Todd Harrington, Troy Peters and Mick Mills. Our monitors for this project were Andrew Willson and Bevan Kathage. Velseis also acknowledges the Centre for Wave Phenomena, Colorado School of Mines, for the development and distribution of Seismic Unix – a free research and seismic processing package. Our apologies for any omissions.

TABLE OF CONTENTS

ABSTRACT	(i)
EXECUTIVE SUMMARY	1
ACKNOWLEDGEMENTS	4
LIST OF FIGURES	8
LIST OF TABLES	10
CHAPTER 1 INTRODUCTION	11
1.1 Introduction	11
1.2 Fundamental Concepts of Converted-Wave Seismology Re-Visited	11
1.3 Project Overview	14
CHAPTER 2 MULTI-COMPONENT GEOPHONES	16
2.1 Introduction	16
2.2 The Influence of the Geophone and Recording Filter on the Seismic Signal	16
2.3 3C Geophone Trials	19
2.4 Discussion	26
CHAPTER 3 PS-WAVE BEHAVIOUR	30
3.1 Introduction	30
3.2 The Propagation of PS Waves in the Sub-Surface	30
3.3 Diodic Moveout	31
3.4 Diodic Illumination	33
3.5 Improving the PS-Wave Stack	35
3.6 Improving PS-Wave Interpretation	35
CHAPTER 4 ADVANCES IN CONVERTED-WAVE PROCESSING METHODOLOGY	38
4.1 Introduction	38
4.2 S-wave Receiver Statics	38
4.3 CCP Binning	42
4.4 Post-Stack Noise Attenuation	43
4.5 Vector Processing	43
4.6 Converted-Wave Processing Flow	46
CHAPTER 5 REAL-DATA TRIAL #1	50
5.1 Introduction	50
5.2 Reprocessing Results	50

CHAPTER 6 REAL-DATA TRIAL #2	54
6.1 Introduction	54
6.2 Reprocessing Results	54
CHAPTER 7 REAL-DATA TRIAL #3	60
7.1 Introduction	60
7.2 Data Acquisition	60
7.3 Trial Results	64
CHAPTER 8 V_p/V_s INTERPRETATION: THEORY AND SYNTHETIC DATA ANALYSIS	68
8.1 Introduction	68
8.2 Methodology	68
8.3 Recovering Absolute V_p/V_s Values	69
8.4 Detection of Lateral Geological Anomalies	74
CHAPTER 9 V_p/V_s INTERPRETATION: REAL DATA EXAMPLES	80
9.1 Introduction	80
9.2 V_p/V_s Interpretation of Real Data	80
9.3 Results from Trial #2	84
9.4 Results from Trial #3	87
9.5 Discussion	88
CHAPTER 10 INTEGRATED PROCESSING OF THE HORIZONTAL COMPONENTS OF DATA	93
10.1 Introduction	93
10.2 Seismic Energy on the Crossline Component	93
10.3 Shear-Wave Splitting (SWS)	94
10.4 Real-Data Analysis	96
10.5 Discussion	97
CHAPTER 11 DISCUSSION AND CONCLUSIONS	102
11.1 Motivation for this Research	102
11.2 Summary of Conclusions	102
11.3 Future Research and Development	104
11.4 Conclusions	105
REFERENCES	106
GLOSSARY	109

APPENDIX A – S-WAVE RECEIVER STATIC CORRECTIONS

APPENDIX B – CCP BINNING

APPENDIX C – POST-STACK EIGENVECTOR FILTERING

APPENDIX D – ELASTIC WAVEFIELD DECOMPOSITION

APPENDIX E – CONVERTED-WAVE PROCESSING OF TRIAL #1

APPENDIX F – CONVERTED-WAVE PROCESSING OF TRIAL #2

APPENDIX G – PROCESSING OF TRIAL DATASET #3

APPENDIX H – SEISMIC RESOLUTION

APPENDIX I – SYNTHETIC SEISMIC MODELLING

LIST OF FIGURES

Figure 1.1	Schematic of multi-component seismic recording.	12
Figure 1.2	Representative 3C shot record.	13
Figure 2.1	Cut-a-way schematic of a geophone.	17
Figure 2.2	The effect of frequency bandwidth on the seismic pulse.	18
Figure 2.3	Representative vertical and inline shot records from Trial Dataset #3.	20
Figure 2.4	Representative raw trace spectra for Trial Dataset #3.	21
Figure 2.5	Frequency spectra for P and PS reflection energy from Trial #3.	22
Figure 2.6	Representative vertical and inline shot records from Line A.	23
Figure 2.7	Representative vertical and inline shot records from Line B.	24
Figure 2.8	Representative raw trace spectra for Line B.	25
Figure 2.9	Representative low-cut filtered vertical and inline shot records from Line B.	27
Figure 2.10	Frequency spectra for P and PS reflection energy from Line B.	28
Figure 2.11	Frequency spectra for P and PS reflection energy from Line A.	29
Figure 3.1	Ground vibrations associated with P and S seismic waves.	30
Figure 3.2	Schematic to illustrate diodic effects of a dipping geological layer on PS reflection events.	32
Figure 3.3	A real NMO-corrected CCP gather acquired over a dipping coal seam.	32
Figure 3.4	Positive- and negative-offset PS sections from Trial #3 demonstrating diodic illumination.	34
Figure 3.5	Schematic illustrating a geological scenario that could result in the diodic illumination observed in Figure 3.4.	35
Figure 3.6	Fault locations on positive- and negative-offset synthetic PS sections.	37
Figure 4.1	Comparison of S-wave receiver statics computed for Line C using original and new statics methods.	39
Figure 4.2	Inline shot record from Line C with no S static corrections, S static corrections derived from original method and S static corrections derived from new method.	40
Figure 4.3	Inline shot record from Line C with no S static corrections, S static corrections derived from original method and S static corrections derived from new method.	41
Figure 4.4	The common-conversion points of a PS wave.	42
Figure 4.5	Line C PS image before and after eigenvector filtering.	44
Figure 4.6	Demonstration of elastic wavefield decomposition on a synthetic multi-component shot record.	45
Figure 4.7	Current PS processing flow.	47
Figure 4.8	Comparison of PS sections generated for Line C in 2004 and 2006.	48,49
Figure 5.1	Demonstration of elastic wavefield decomposition on a real multi-component shot record from Trial #1.	52
Figure 5.2	Comparison of Trial #1 PS sections generated with and without inclusion of vector processing in the PS processing flow.	53
Figure 6.1	P-wave and reprocessed PS-wave seismic images for Trial #2.	56,57
Figure 6.2	Original PS-wave seismic image for Trial #2.	58

Figure 6.3	Comparison of original and new S-wave receiver static corrections for Trial #2.	59
Figure 6.4	Representative trace spectra for P and PS stacks in Figure 6.1.	59
Figure 7.1	Field acquisition of Trial Dataset #3.	61
Figure 7.2	Surface elevation along survey line for Trial #3.	61
Figure 7.3	Representative vertical and inline shot records from Trial Dataset #3.	62
Figure 7.4	Representative raw trace spectra for Trial Dataset #3.	63
Figure 7.5	P- and PS-wave seismic images for Trial #3.	65,66
Figure 7.6	Representative trace spectra for P and PS stacks in Figure 7.5.	67
Figure 8.1	Synthetic earth model used to demonstrate impact of interval thickness on V_p/V_s analysis.	69
Figure 8.2	Synthetic P- and PS-wave seismic sections corresponding to the coal-wedge model given in Figure 8.1.	70
Figure 8.3	TWT picks for the top and bottom coal reflection events in the seismic sections shown in Figure 8.2.	71
Figure 8.4	V_p/V_s measurements computed from the TWT picks in Figure 8.2.	71
Figure 8.5	Synthetic earth models and corresponding V_p/V_s analysis results for geological intervals of varying thickness.	73
Figure 8.6	Synthetic earth model and corresponding V_p/V_s analysis results demonstrating the impact of lateral resolution on integrated P/PS interpretation.	74,75
Figure 8.7	Synthetic earth model and corresponding V_p/V_s analysis results demonstrating the sensitivity of V_p/V_s interpretation to velocity-ratio contrasts.	76
Figure 8.8	Synthetic earth model, corresponding P and PS seismic sections, and derived V_p/V_s attribute demonstrating that reflection events contaminated with noise should not be used for V_p/V_s analysis.	77,78,79
Figure 9.1	Detailed synthetic earth model and RMS V_p/V_s values for a number of defined geological intervals.	81,82,83
Figure 9.2	V_p/V_s interpretation results from Trial #2.	85,86
Figure 9.3	V_p/V_s interpretation results from Trial #3.	89,90,91,92
Figure 10.1	Schematic illustration of shear-wave splitting.	94
Figure 10.2	Representative examples of PS energy on inline and crossline shot records from Line C.	98,99
Figure 10.3	PS images derived from Line C inline- and crossline-component data.	100
Figure 10.4	Polarisation of the fast S wave computed via integrated processing of the inline and crossline PS stacks given in Figure 10.3.	101
Figure 10.5	Traveltime delay between fast and slow S waves derived via shear-wave splitting analysis of data given in Figure 10.3.	101
Figure G.1	Comparison of P and PS receiver static corrections for Trial #3.	G7
Figure H.1	Measuring the dominant frequency of a seismic reflection event.	H1

LIST OF TABLES

Table 3.1	Typical V_p/V_s values.	31
Table 7.1	Field acquisition parameters for Trial #3.	60

CHAPTER ONE INTRODUCTION

1.1 Introduction

The Australian coal industry has a strong motivation, in terms of productivity and safety, to better characterise the sub-surface prior to underground mine planning and development. Seismic reflection has become the geophysical tool of choice to help achieve this, and ongoing research into coal-seismic acquisition, processing and interpretation technologies is driven by the desire to continually improve the geological detail that can be extracted from seismic data.

Based on successes in the petroleum sector, Velseis Pty Ltd has directed significant research effort towards converted-wave seismic methods. Converted-wave seismic reflection in the petroleum industry has enabled independent validation of structures, imaging through gas-filled sediments, imaging beneath basalt bodies, improved lithology classification and detection of reservoir fracture systems (e.g. Granli *et al.*, 1999; Li *et al.*, 1998; DeAngelo *et al.*, 2003; Gaiser and Van Dok, 2001). By analogy, there is considerable opportunity for enhancing remote characterisation of the sub-surface in the coal environment.

ACARP Project C10020 (completed June 2003) included the first attempts in Australia to utilise shallow, high-resolution multi-component seismic data and converted-wave technology to image coal seams. The project successfully developed robust acquisition and processing methodologies, and demonstrated that converted-waves can be utilised for *structural* imaging of coal seams.

This project examines whether integrated application of conventional and converted-wave seismic data can extract richer *lithological* information from the sub-surface. Here, the term 'lithological' is used broadly to describe detailed geological character such as rock type, fracturing, presence of fluids/gases etc. Thus, in addition to the ongoing development of methodologies to enhance PS processing, this project focuses on evaluating to what extent joint use of conventional and converted-wave seismic images (compared to using conventional seismic data alone) can enhance our knowledge of sub-surface geology away from borehole locations.

1.2 Fundamental Concepts of Converted-Wave Seismology Re-Visited

Recall that, seismic reflection involves imaging the sub-surface using artificially-generated sound waves. Typically, small dynamite explosions or vibratory sources (e.g. mini-SOSIE) are used to generate the seismic waves for coal exploration. These seismic sources dominantly produce compressional (P) seismic waves. Downward-propagating P waves will be partially reflected and transmitted as P waves at each geological boundary. At coal seams in particular, a significant fraction of this P energy will also be partially converted to shear (S) energy. As a result, both P and S waves will be reflected back to the surface during a coal-seismic survey. Multi-component seismic exploration measures both the vertical and horizontal components of ground motion to enable exploitation of both the P and converted P-to-S energy arriving at the surface (Figure 1.1).

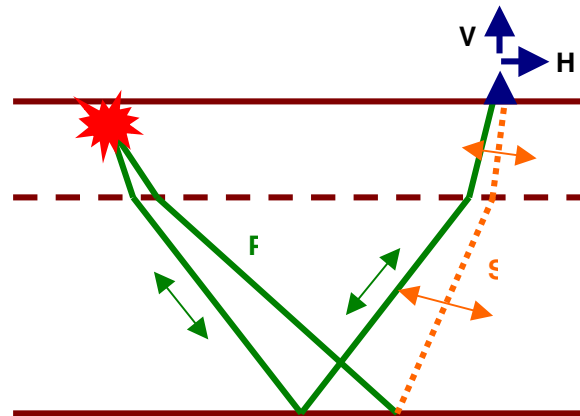


Figure 1.1 Multi-component seismic recording recognises that both P and mode-converted PS waves will arrive at the surface. Since the particle motion of an upward travelling P wave is largely vertical (indicated by green arrows), a vertically-oriented geophone responds well to reflected P waves. The particle motion of an upward travelling S wave is largely horizontal (indicated by the orange arrows). Thus, both the vertical and horizontal components of ground motion must be recorded to take advantage of both wave types. Note that, multi-component recording may also be referred to as three-component (3C) recording, since the vertical and two orthogonal horizontal components (inline and crossline components) of ground motion are generally recorded.

The seismic energy generated at a single seismic source location, and recorded on a number of multi-component geophones, creates a 3C shot record (Figure 1.2). Each seismic trace in the shot record is a measure of the seismic energy that vibrates the ground at the particular receiver location. The distance between the source location and the receiver station is referred to as the offset. Geophones sitting in front of the seismic source have positive offsets, while geophones sitting behind the seismic source have negative offsets.

A seismic survey will typically comprise many hundreds or thousands of shot records. During the course of data processing, the data are re-sorted to gathers of traces that have been reflected from the same sub-surface point. The vertical-component records are processed to produce a conventional P-wave seismic section. The common-reflection point for P waves is referred to as the common midpoint (CMP) (because for horizontally-layered media, the common-reflection point for each trace lies halfway between its source and receiver location) or the common depth point (CDP). The inline-component records are generally processed to produce the PS-wave seismic section. The common-reflection point for PS waves is referred to as the common conversion point (CCP).

Figure 1.2 (next page) (a) Vertical component, (b) inline component and (c) crossline component of a representative coal-seismic 3C shot record acquired using a mini-SOSIE source. The vertical axis is a measurement of the time it takes for the seismic energy to travel from the seismic source (at 0 m offset), down to a geological boundary and back to the surface (also referred to as the two-way time (TWT)). The horizontal axis represents offset, the distance between the source and each receiver station. Note that, seismic energy that travels straight down from the source and back to the surface arrives earlier than energy that travels obliquely to receivers at far offsets. A number of different seismic wave types are indicated.

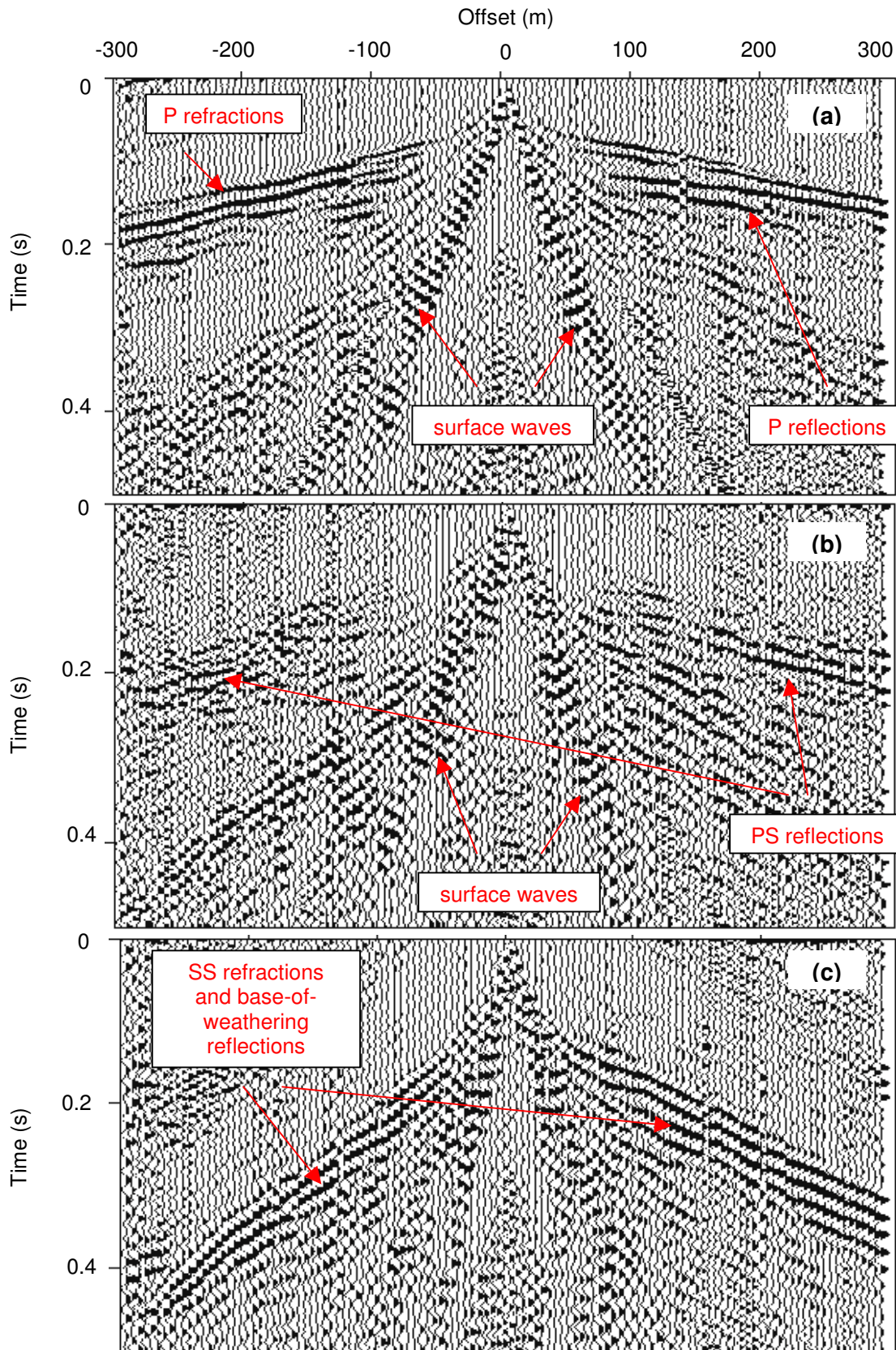


Figure 1.2 (see figure caption on previous page)

1.3 Project Overview

Objectives

The primary objectives of this project, as listed in the original project proposal, have been to:

- Analyse anomalous PS-wave propagation behaviour to determine whether it can be directly interpreted in terms of lateral geological inhomogeneities in the sub-surface;
- Investigate the integration of P and PS seismic attribute information for mapping lithology variations (e.g. sand vs shale); and
- Investigate integrated processing of the two horizontal components of 3C data for detecting and characterising zones of significant fracturing.

Additional research objectives have been added as their necessity has become apparent. Specifically, this project has also addressed:

- Acquisition procedures for optimum PS data collection;
- PS processing algorithms for improving the converted-wave image.

Methodology

The above objectives have been achieved using the following methodology:

- (i) analysis of 2D-3C seismic data acquired using different geophones/recording-filters
- (ii) investigation of PS-wave propagation behaviours
- (iii) development of new and improved PS processing algorithms;
- (iv) re-processing of existing 2D-3C seismic datasets (acquired during ACARP Project C10020);
- (v) acquisition and processing of one new 2D-3C seismic dataset;
- (vi) construction and analysis of synthetic 2D-3C seismic data;
- (vii) development and implementation of V_p/V_s interpretation methodology;
- (viii) integrated processing trial using the two horizontal components of data for a 2D-3C dataset

Note that, it is expected that converted-wave seismic technology will eventually be exploited as an enhancement to 3D seismic exploration. However, the geophysical concepts of converted-wave seismology can be most economically tested via 2D experiments, and this is the approach taken here.

Report Outline

Chapter 2 compares and contrasts various 3C seismic datasets acquired using different geophone/recording-filter configurations. Characteristic PS-wave propagation behaviour and the geological anomalies that cause this behaviour are explored in Chapter 3. Chapter 4 summarises key advances we have made in our PS processing methodology since the completion of ACARP Project C10020. Details of the S-wave receiver statics, CCP-binning and post-stack noise attenuation algorithms are given in Appendices A, B and C. Results from the re-processing of the Trial #1 and Trial #2 datasets (acquired as part of Project C10020) are given in Chapters 5 and 6. The vector-processing method used on Trial Dataset #1 is described in Appendix D, and the PS processing flows used for the Trial #1 and Trial #2 datasets are given in Appendices E and F, respectively. Details of the acquisition, processing and conventional interpretation of the new 3C

seismic dataset (Trial #3) are found in Chapter 7. The P and PS processing flows for Trial #3 are described in Appendix G. Further discussion on seismic resolution is provided in Appendix H. Chapters 8 and 9 investigate the potential for V_p/V_s interpretation to extract lithological information away from boreholes using both synthetic and real 3C seismic data. Details on the construction of the synthetic seismic data used throughout this project are given in Appendix I. The potential for integrated processing of the two horizontal components of data to identify zones of faulting/fracturing is examined in Chapter 10. The significant conclusions drawn from this research, together with recommendations for future research and development, are presented in Chapter 11. A list of references and a glossary of terms complete the report.

Products

This report is available in hardcopy or digital format to all Australian coal producers, Australian researchers and other service providers to the Australian Coal Industry. Contact ACARP (www.acarp.com.au) to purchase a copy.

The multi-component seismic data acquired as part of this research can only be obtained for approved purposes with the permission of the relevant host mine-site and ACARP. Contact Velseis Pty Ltd (www.velseis.com.au) to make arrangements for access to seismic data.

CHAPTER TWO

MULTI-COMPONENT GEOPHONES

2.1 Introduction

We have observed over the past five years, that our PS seismic sections consistently have dominant frequencies in the range 35 – 50 Hz. (In contrast, conventional P-wave seismic sections can have dominant frequencies up to 140 – 180 Hz). The low-frequency range of PS energy is problematic when the geophones and recording filters being used to acquire the 3C seismic data are designed to suppress energy with frequencies less than 40Hz. The effective truncation of energy below 40 Hz, coupled with the fact that our PS sections don't have signal much above 50 Hz, results in the PS energy frequency bandwidths being very narrow. Consequently, our PS reflection events are 'ringy' (i.e. the seismic wavelets have large side-lobes) and create significant interference patterns when imaging thin geological layers. As will be discussed in subsequent chapters, not all of the loss of high- frequency information in the PS stack is believed to be caused by natural attenuation of the upward travelling S energy – improved PS processing has a role to play in helping increase dominant frequencies in the PS sections. Nevertheless, enabling the extension of the PS bandwidth into lower frequencies will help to broaden the PS signal bandwidth and reduce 'ringiness' in our PS sections. A number of experiments have been undertaken to examine the impact of using geophones designed to acquire lower-frequency information. This chapter briefly reviews geophones, and their related recording filters, and the effect these have on seismic events. Results from various 3C seismic surveys, each using different geophone/recording-filter configurations, are compared and contrasted to determine the optimum parameters for acquiring converted-wave seismic data in coal environments.

2.2 The Influence of the Geophone and Recording Filter on the Seismic Signal

The receiving device used to detect ground vibrations during a seismic survey is called a geophone. Geophones consist of a magnetised mass fixed to an external case, and a surrounding coil suspended on springs (Figure 2.1). Vertically suspended systems are sensitive to vertical ground motion. Horizontally suspended systems are sensitive to horizontal ground motion. A 3C geophone comprises one vertical and two orthogonal horizontal geophone elements to record the vertical and horizontal ground vibrations associated with P and PS energy, respectively. When vibration of any sort moves the case of a geophone, the suspended coil remains stationary due to its inertia. The relative movement of the magnetised mass generates an electrical voltage proportional to the velocity of the coil. Note however, that at a certain frequency of ground vibration the oscillation of the geophone becomes extremely large, and spurious voltage readings result. The frequency at which this occurs is called the natural frequency of the geophone. Damping of the geophone up to this natural frequency is necessary to make the geophone oscillate more regularly. Thus, the natural frequency of a geophone typically dictates the lowest frequency that is accurately measured by the geophone. Prior to the commencement of this project, all of our 3C seismic data were acquired using geophones with a natural frequency of 40 Hz. Throughout this research, we have trialed geophones with a natural frequency of 10 Hz.

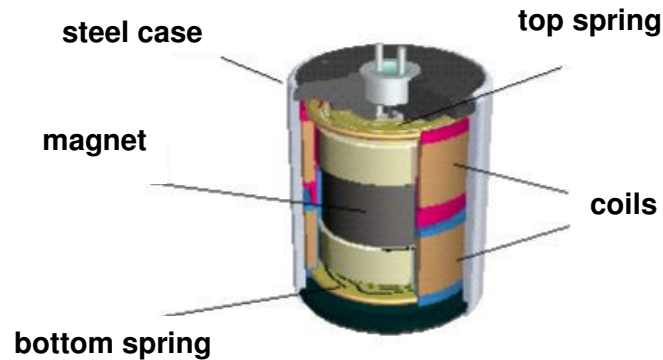


Figure 2.1 Cut-a-way schematic of a geophone.

It is common practice when using all geophone types, to apply both a low-cut and high-cut frequency filter prior to the analog-to-digital conversion of the signal measured by the geophone. The high-cut filter is necessary to prevent aliasing of the seismic signal. The low-cut filter removes low-frequency energy and is often used to help ensure the recording system is not swamped by undesirable low-frequency noise (e.g. groundroll). Velseis currently have three options available with respect to filtering the low-end of the frequency spectrum – no recording filter, a 16 Hz recording filter (i.e. -3 dB at 16 Hz), or a 40 Hz recording filter (i.e. -3 dB at 40 Hz). Typically, the 40 Hz recording filter is used with geophones that have a natural frequency of 30 Hz or 40 Hz (i.e. the low-cut filter is being applied to frequencies already being damped by the geophone, and preserves frequencies not affected by damping). For geophones with a lower natural frequency (e.g. 10 Hz or 14 Hz), the 16 Hz recording filter is used. We have also trialed using 10 Hz geophones with no recording filter.

The effects of various geophone/recording-filter configurations on seismic reflection events are demonstrated in Figure 2.2 using synthetic seismic data. For typical P-wave reflection energy, using a geophone with a natural frequency of 40 Hz, together with a 40 Hz recording filter, results in a nice, sharp seismic pulse (Figure 2.2(a)). This is because the P-wave signal typically extends beyond 100 Hz, and the resultant signal bandwidth exceeds one octave. In contrast, stacked PS reflection events generally only contain strong signal up to approximately 60 Hz. When a 40 Hz low-cut recording filter is used, the PS signal has an extremely narrow bandwidth (in this instance only $\frac{1}{2}$ an octave). The corresponding seismic wavelet suffers from large side lobes and is described as ‘ringy’ (Figure 2.2.(b)). If a geophone with a natural frequency of 10 Hz and a 16 Hz recording filter is used instead, the PS reflection events will effectively have a frequency bandwidth that extends approximately 2 octaves (from approximately 15 Hz to 60 Hz). The resultant PS seismic pulse will no longer be affected by high-amplitude side lobes (Figure 2.2(d)), and will result in a much simpler seismic image. Note that, the same effect (although more subtle) is observed for the P seismic wavelet when the 10 Hz geophone / 16 Hz recording-filter configuration is emulated (Figure 2.2(c)). Based on our real-data observations, and simple synthetic experiments like this one, we believe that extending the low-frequency content of our seismic recordings should have a discernible effect on the PS seismic section and improve the ability of our PS data to image the sub-surface.

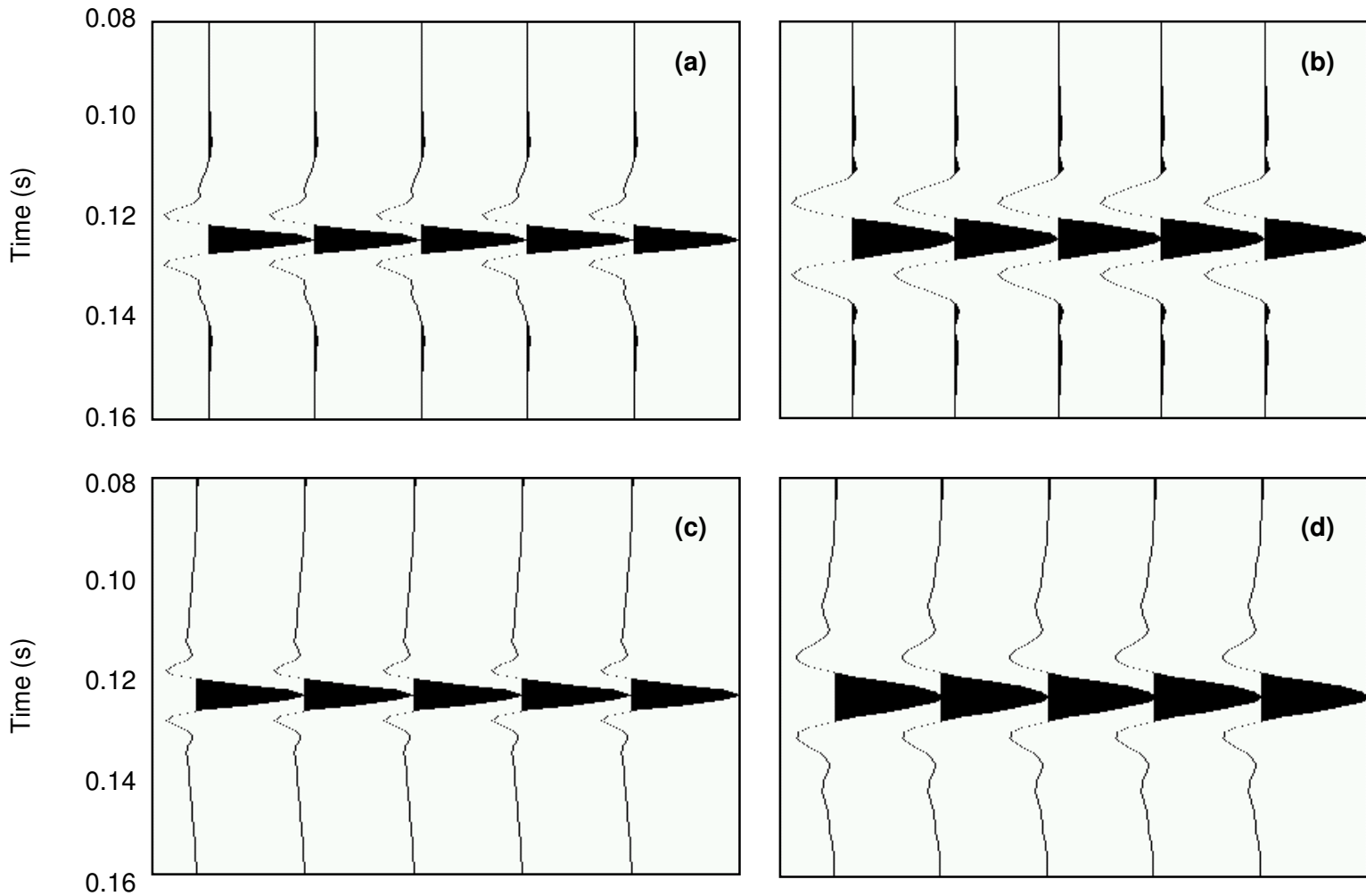


Figure 2.2 The effect of frequency bandwidth on the seismic pulse. (a) P and (b) PS seismic pulses typically recorded using a 40 Hz geophone with a 40 Hz low-cut recording filter. The PS wavelet is broad and 'ringy' (i.e. has large side lobes). (c) P and (d) PS seismic pulses typically recorded using a 10 Hz geophone with a 16 Hz low-cut recording filter. Most notably, the broader frequency bandwidth that results from the capture of lower frequencies helps to reduce the amplitude of the PS-pulse side lobes in (d).

2.3 3C Geophone Trials

10 Hz Geophone (16 Hz recording filter)

As noted above, prior to the commencement of this research project, all of our 3C seismic data were acquired using our purpose-built 40 Hz 3C geophones (Velseis, 2003). Our third ACARP trial dataset (Trial #3) however, was acquired using 3C geophones with a natural frequency of 10 Hz and a 16 Hz low-cut recording filter. Figure 2.3 shows a representative shot record from this dataset. Both the vertical and inline records contain significantly more low-frequency energy than data from Trials #1 and #2 (compare Figure 2.3 with data records shown in Velseis (2003)). Corresponding representative raw-trace frequency spectra (Figure 2.4) highlight that, in fact, the strongest energy in the Trial #3 data lies at the low-frequency end of the spectrum. This dominant energy has a bandwidth of approximately 10 – 20 Hz, and has been identified as the groundroll energy that is prominent in Figure 2.3. Less obvious is the fact that the 10 Hz geophones have also enabled acquisition of significant PS energy below 40 Hz. Frequency analysis of the actual P and PS reflection energy (Figure 2.5) reveals that the P signal dominantly comprises energy in the 50 – 100 Hz range. Thus, the P section for this trial is expected to be independent of the type of geophone (10Hz or 40Hz) used to acquire the seismic data. In contrast, the dominant PS energy lies in the frequency range 20 – 100 Hz (Figure 2.5(b)). Taking into consideration that, currently, the PS processing of this dataset appears to truncate frequencies above approximately 50 – 60Hz (Section 7.3), a 40 Hz low-cut recording filter would remove a significant portion of the desired PS signal. Ensuring that the PS signal bandwidth extends below 40 Hz gives us the best chance to reduce ‘ringiness’ in the final Trial #3 PS section.

40 Hz Geophone (40 Hz recording filter) vs 10 Hz Geophone (no recording filter)

Velseis has conducted a number of commercial 2D-3C seismic experiments in the Bowen Basin in parallel to our ACARP research. These trials represent the first efforts in Australia to acquire converted-wave coal seismic data using a surface mini-SOSIE source (all of our ACARP trials have been acquired using a buried dynamite source). Our mini-SOSIE experiments have included testing two geophone/recording-filter configurations. We are able to include the results of these trials here.

Figure 2.6 shows the vertical- and inline-components of a shot record acquired along a 2D line (Line A) in 2004. These data were recorded using our purpose-built 40 Hz 3C geophones and a 40 Hz low-cut recording filter. In 2006 an intersecting line of data (Line B) was acquired using geophones with a natural frequency of 10 Hz and no recording filters. Figure 2.7 shows the shot record from Line B acquired at the same location as the shot record given in Figure 2.6.

First note that, data from Line B have been acquired using an off-end spread (i.e. all geophones are on one side of the source point) compared to the split-spread used for Line A. This is part of another experiment to determine optimum offset distribution for converted-wave imaging. The outcomes of using these different acquisition geometries are still under consideration.

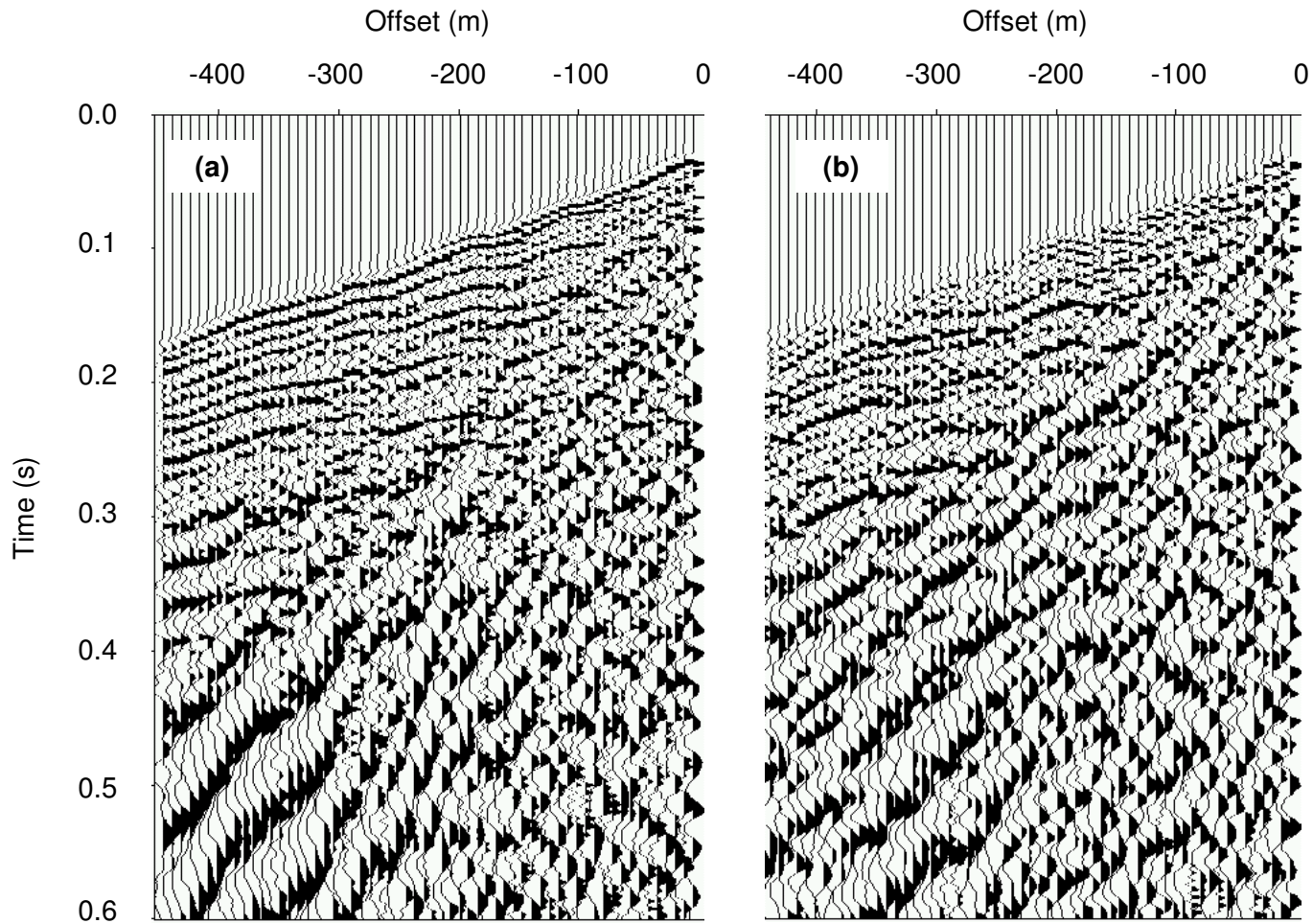


Figure 2.3 Representative (a) vertical-component and (b) inline-component shot records from Trial Dataset #3. These data have been acquired using a geophone with a natural frequency of 10 Hz and a 16 Hz low-cut recording filter. Data from Trial #3 contain significantly more low-frequency energy than data from Trials #1 and Trials #2 (Project C10020). Most notably, the Trial #3 records contain strong groundroll energy (steeply-dipping wavefield covering lower-left portion of both records).

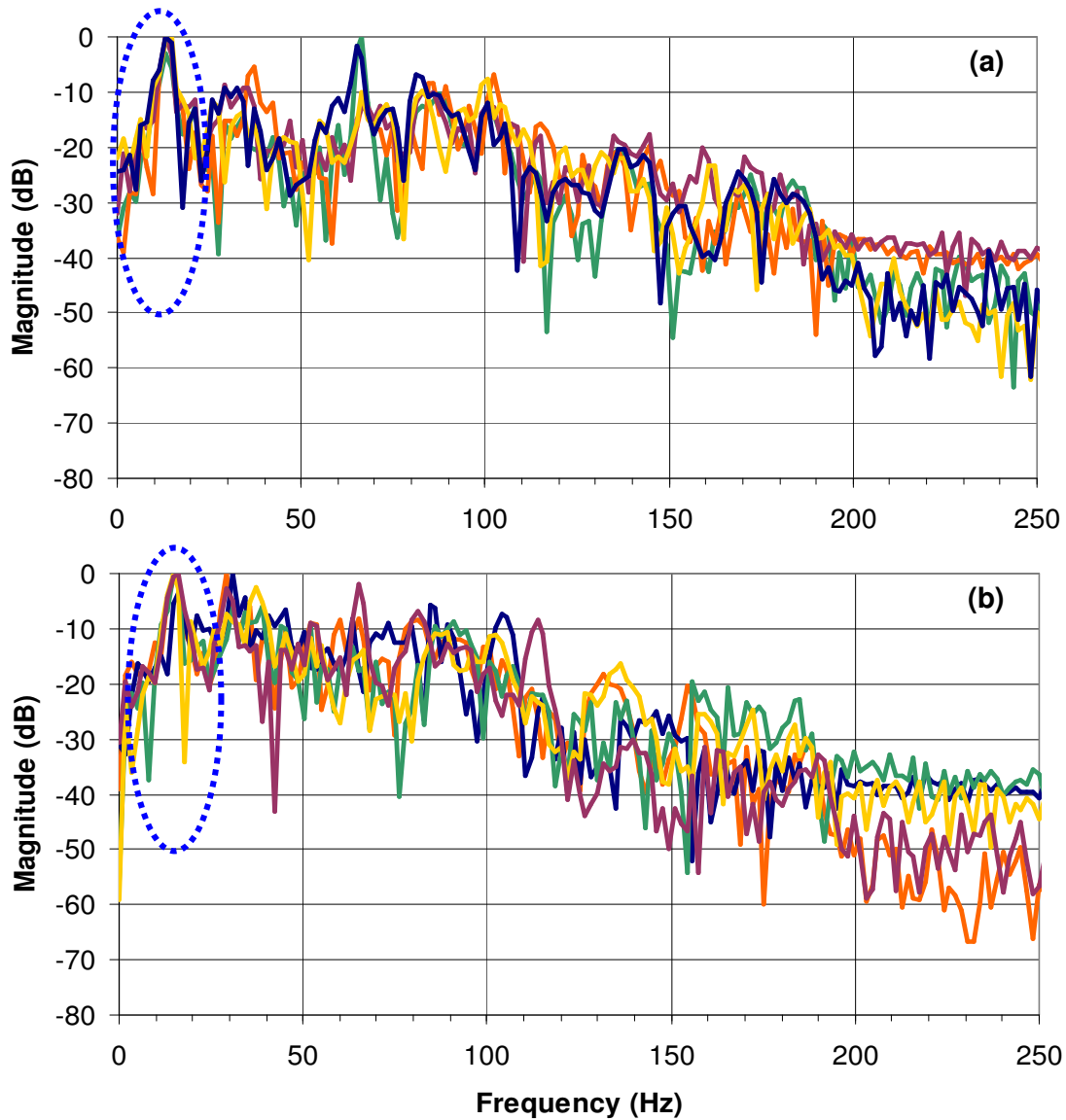


Figure 2.4 Representative trace spectra from the (a) vertical-component and (b) inline-component records given in Figure 2.3. The dotted blue circles highlight the extremely strong, low-frequency energy contained in these data. The bandwidth of this dominant energy is approximately 10 – 20 Hz, and has been identified as the steeply-dipping groundroll energy in the corresponding seismic records.

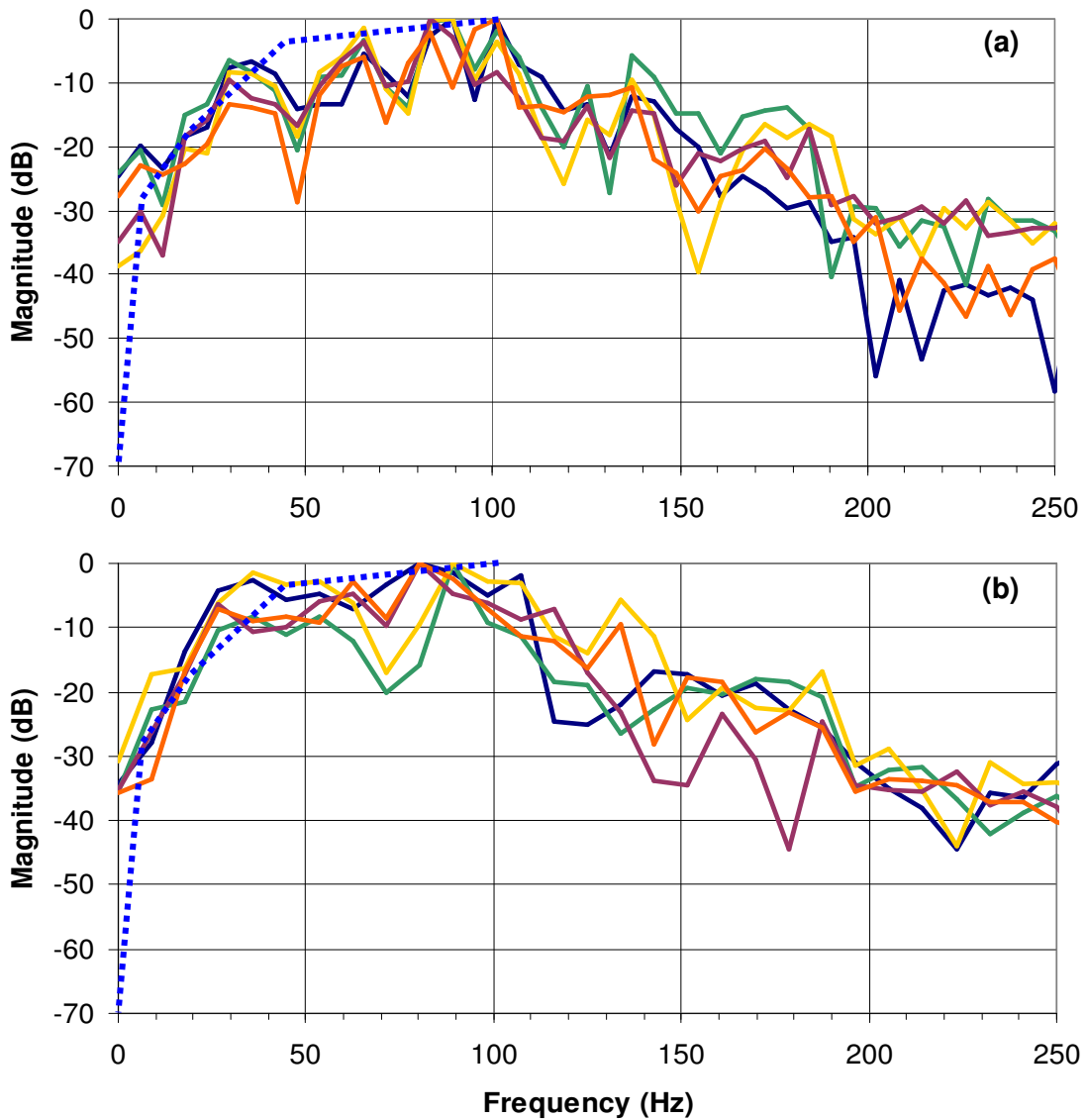


Figure 2.5 Representative (a) P-wave and (b) PS-wave signal spectra for Trial #3 determined by conducting frequency analysis over small windows of desired signal not contaminated by the low-frequency groundroll energy identified in Figure 2.3. The dotted blue line indicates the lower frequency limit of energy that would have been captured if 40 Hz geophones with a 40 Hz low-cut recording filter had been used. Acquisition using the 10 Hz geophones with a 16 Hz low-cut filter has enabled significant PS reflection energy to be recovered below 40 Hz.

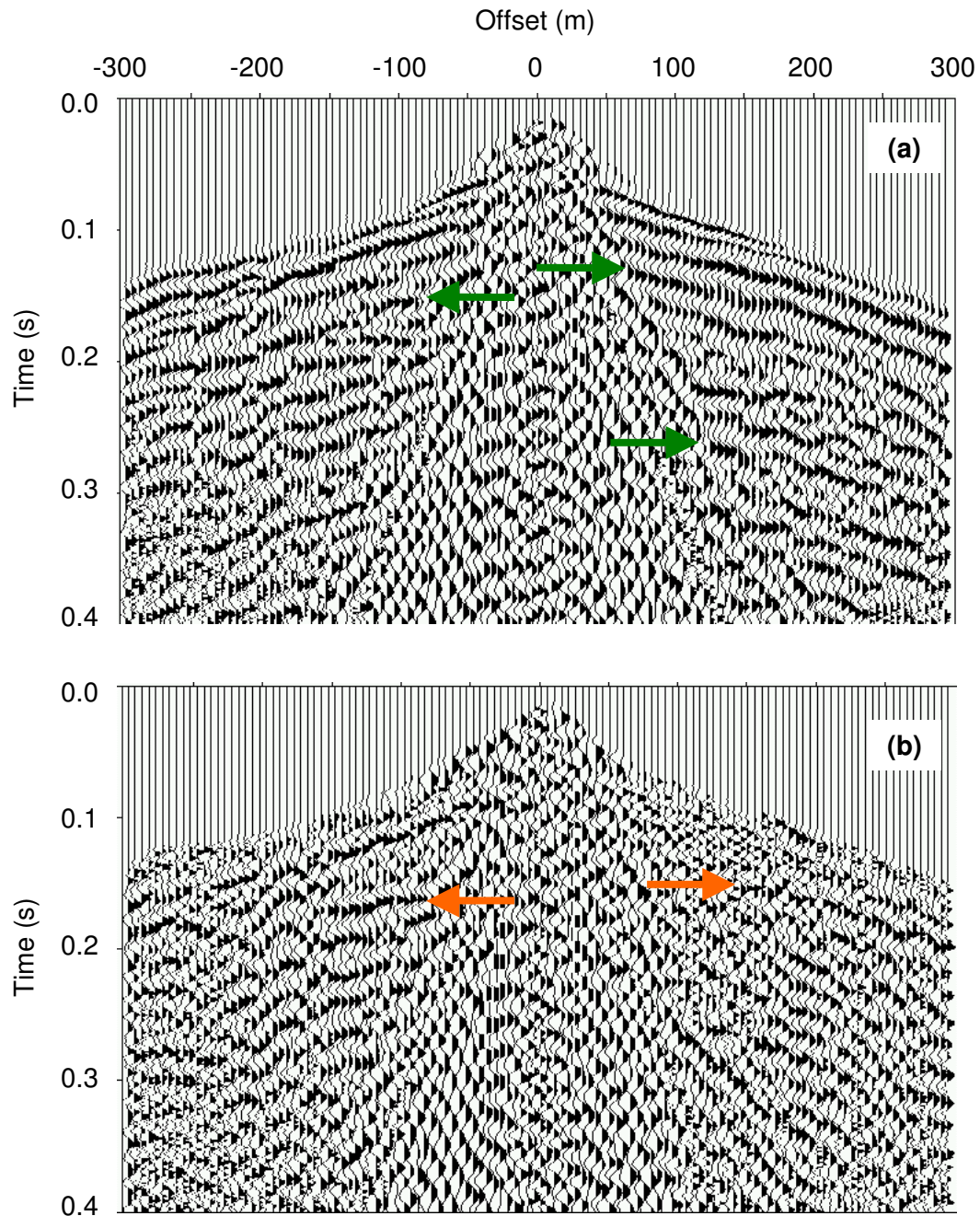


Figure 2.6 Representative (a) vertical-component and (b) inline-component shot records from Line A. These data were acquired in 2004 using a geophone with a natural frequency of 40 Hz and a 40 Hz low-cut recording filter. A number of P and PS reflection events are indicated by the green and orange arrows, respectively.

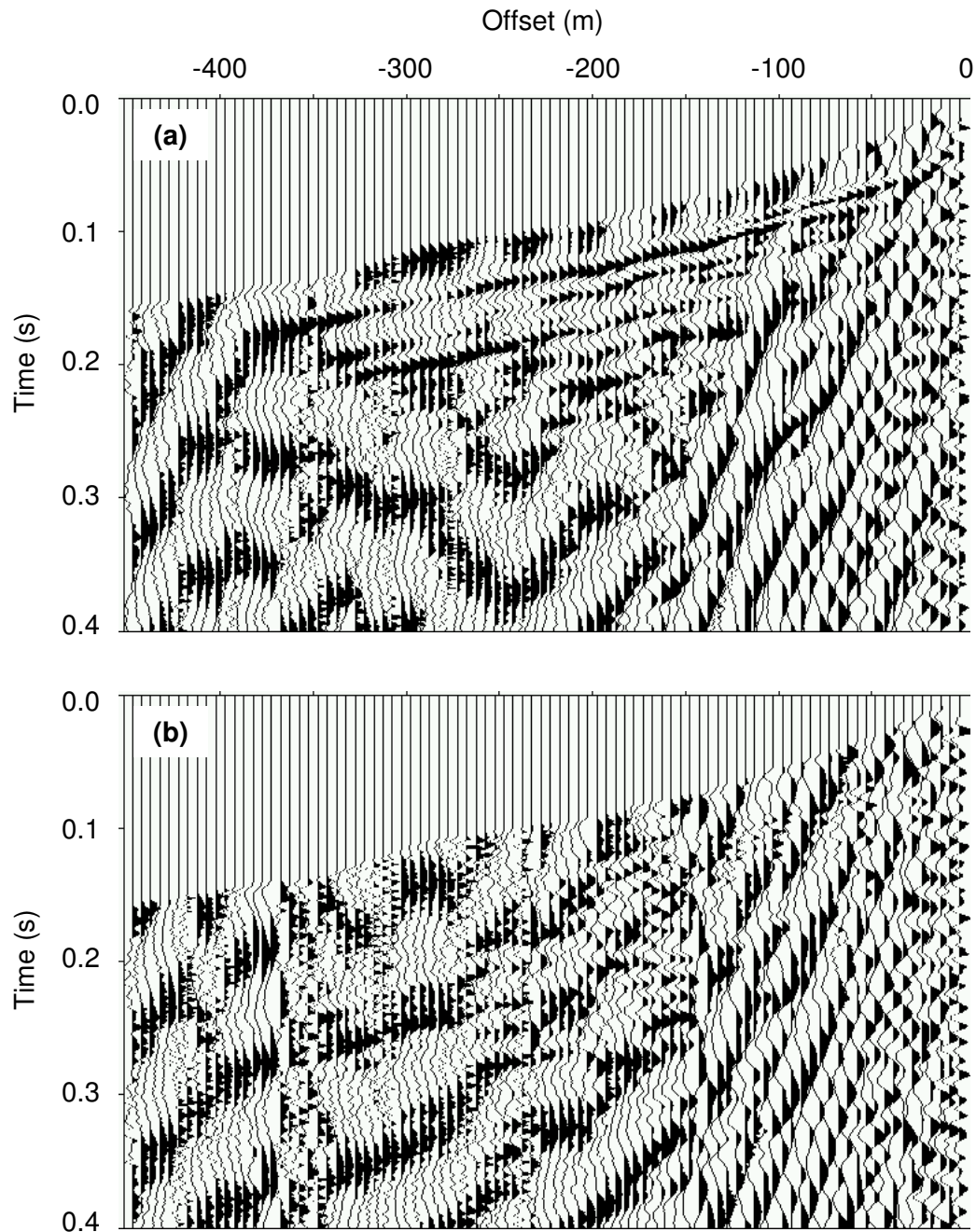


Figure 2.7 Representative (a) vertical-component and (b) inline-component shot records from Line B. These data were acquired in 2006 using a geophone with a natural frequency of 10 Hz and no low-cut recording filter. These shot records are from the same location as those shown in Figure 2.6.

Most significantly, compared to Figure 2.6, the records in Figure 2.7 are totally swamped by low frequency energy – to the extent that desired reflection energy can barely be seen. This is consistent with what we observe in the corresponding representative frequency spectra for these data (Figure 2.8).

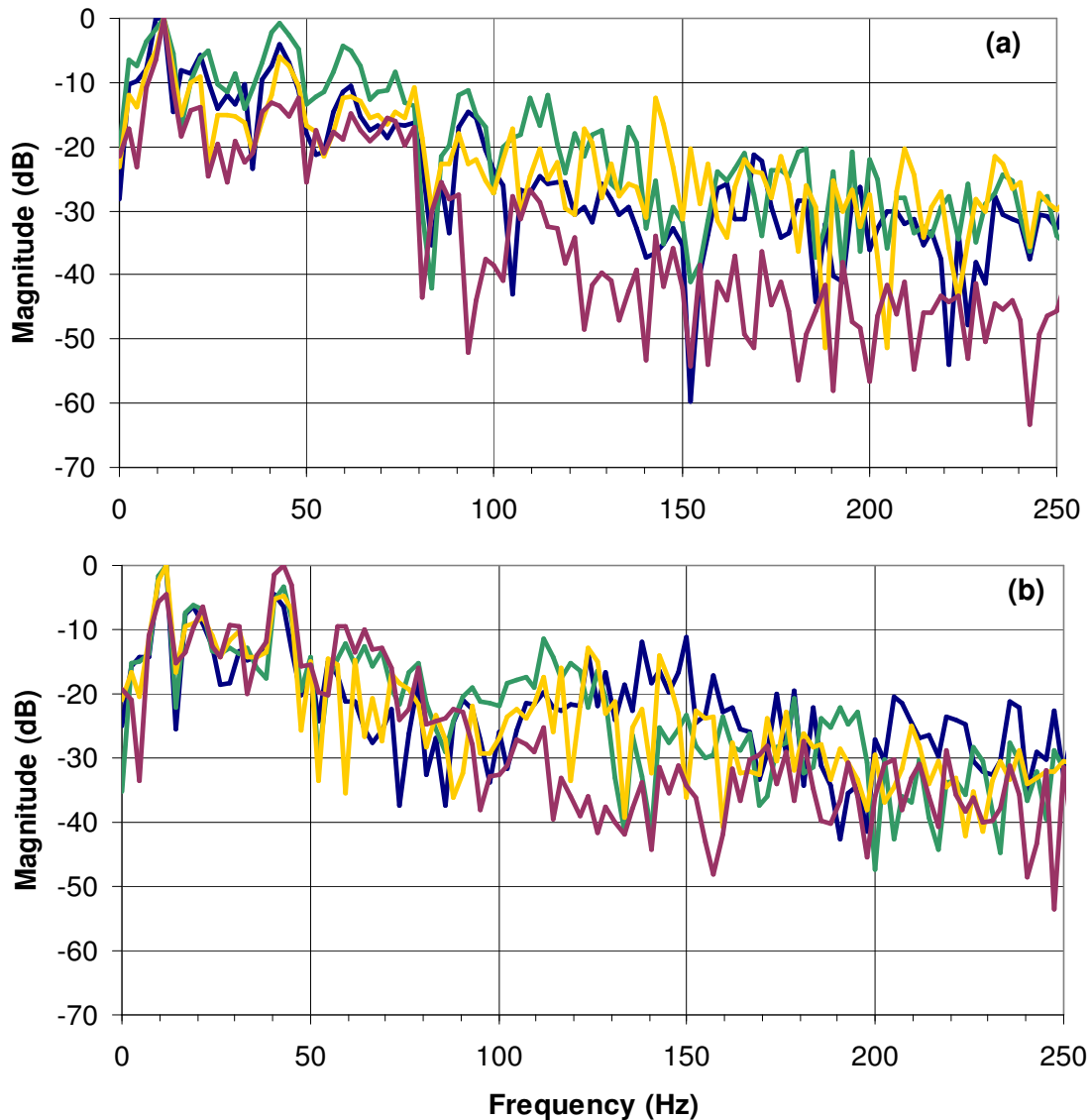


Figure 2.8 Representative trace spectra from the (a) vertical-component and (b) inline-component records given in Figure 2.7. The dominant energy below approximately 20 Hz is associated with the very strong low-frequency noise contaminating the corresponding seismic records. It is apparent from these spectra that this low-frequency energy has much greater power than the remaining data. Hence, higher-frequency signal such as reflection events, are not easily seen in the raw records.

It is possible to determine an optimum low-cut filter to remove a significant portion of the low-frequency noise (the majority of which exists in the 5 – 20 Hz bandwidth), and reveal the desired P and PS reflection events. The low-cut filtered seismic records for Line B are shown in Figure 2.9 – desired reflection events now dominate the records. Frequency analysis of these filtered records enables us to approximate the P and PS signal bandwidths (Figure 2.10). The P signal has dominant energy in the 20 – 80 Hz range, while the PS signal has dominant energy in the 20 – 50 Hz range. For comparison, Figure 2.11 shows the approximate P and PS signal bandwidths for the data acquired using 40Hz geophones. It is clear from a comparison of Figure 2.10(b) with Figure 2.11(b) that the 10 Hz geophones have enabled us to capture a significant amount of PS energy below 40 Hz. This additional low-frequency PS information helps reduce ‘ringiness’ of the PS reflection energy. This is evident in the seismic shot records – the PS reflection events in the inline record acquired with the 40 Hz geophones (Figure 2.6(b)) display a much ‘ringier’, less natural character compared to those in the inline record acquired using the 10 Hz geophones (Figure 2.9(b)).

Note that, for this particular dataset, the 10 Hz geophones have also enabled recovery of significant P-wave energy below 40 Hz (compare Figure 2.10(a) with Figure 2.11(a)). This additional low-frequency P energy was not observed for the Trial #3 experiment because of the different source type – a surface mini-SOSIE source will generate P-wave energy with lower frequencies than a buried dynamite source. Note however, that it is not expected that this additional low-frequency P energy on Line B will make a notable difference in the P-wave stack since we expect the P energy bandwidth to already be sufficiently broad to avoid spurious side lobes on the P reflection events.

2.4 Discussion

The results presented above have demonstrated that strong PS energy can be recovered below 40 Hz if low-frequency energy is allowed to be captured by the recording system. Further, if no low-cut recording filter is incorporated into the acquisition system then a post-acquisition low-cut filter of approximately 20 Hz (i.e. -3 dB at 20 Hz) is necessary to remove low-frequency noise and reveal the desired P and PS reflection signal. Consequently, it is appropriate to use a 16 Hz low-cut recording filter with the 10 Hz geophone for acquisition of low-frequency PS energy.

Note that, to date there has been no investigation into whether using geophones with a lower natural frequency begins to negatively impact on very high P-wave frequencies. While this is not considered an issue for mini-SOSIE surveys (where the upper limit of P-wave frequencies will be reliably measured using a 10 Hz geophone), there is potential for the high P-wave frequencies of dynamite data to extend beyond the typical frequency range that will be reliably recorded using a traditional 10 Hz geophone. On the other hand, new geophones can work around this problem and/or high-frequency seismic energy may suffer from significant attenuation anyway due to local geological conditions. Thus, each survey should be considered on a case-by-case basis. Our general recommendation is that a 3C coal-seismic survey should use geophones with a lower natural frequency (e.g. 10 Hz or 14 Hz), and a corresponding low-cut recording filter (e.g. 16 Hz).

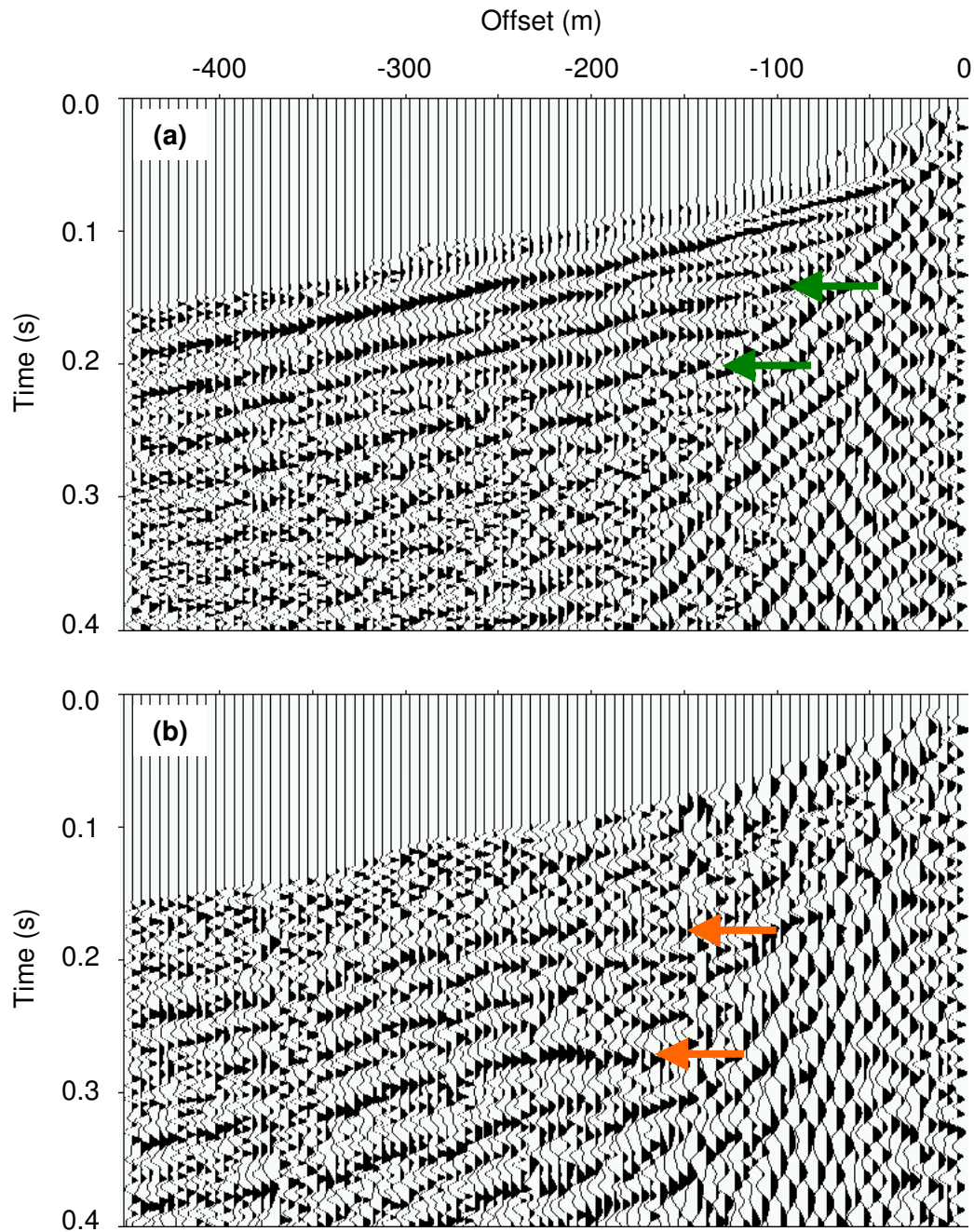


Figure 2.9 (a) Vertical-component and (b) inline-component shot records from Figure 2.7 (Line B) after removal of low-frequency noise via a 20 Hz low-cut filter. Desired P and PS reflection events can now be seen (indicated by the green and orange arrows, respectively).

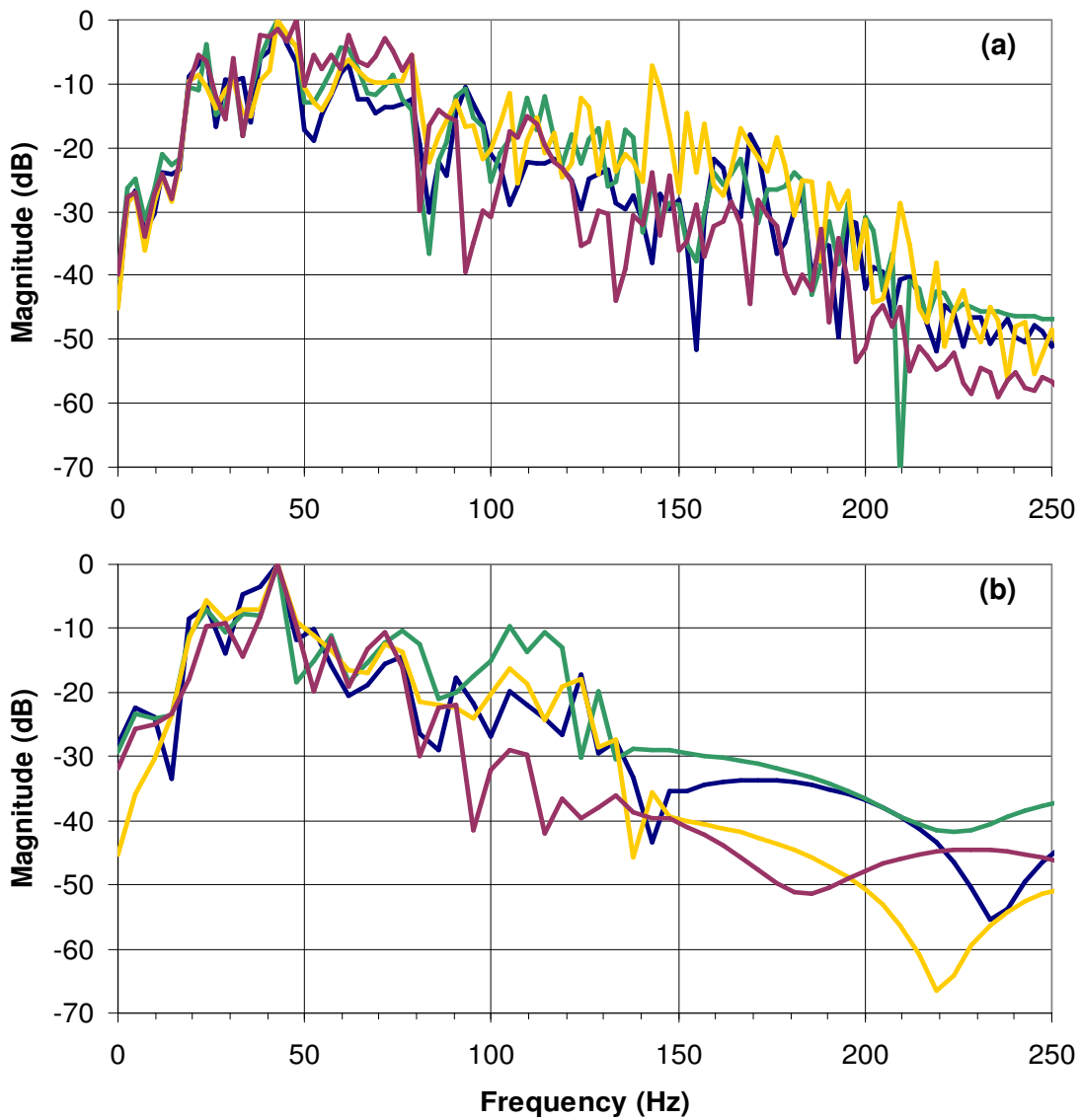


Figure 2.10 Representative (a) P-wave and (b) PS-wave signal spectra for Line B determined by conducting frequency analysis over small data windows in which the desired P and PS reflection energy is dominant. Acquisition using the 10 Hz geophones has enabled significant P and PS reflection energy to be recovered below 40 Hz. (Compare with the P and PS signal spectra in Figure 2.11.)

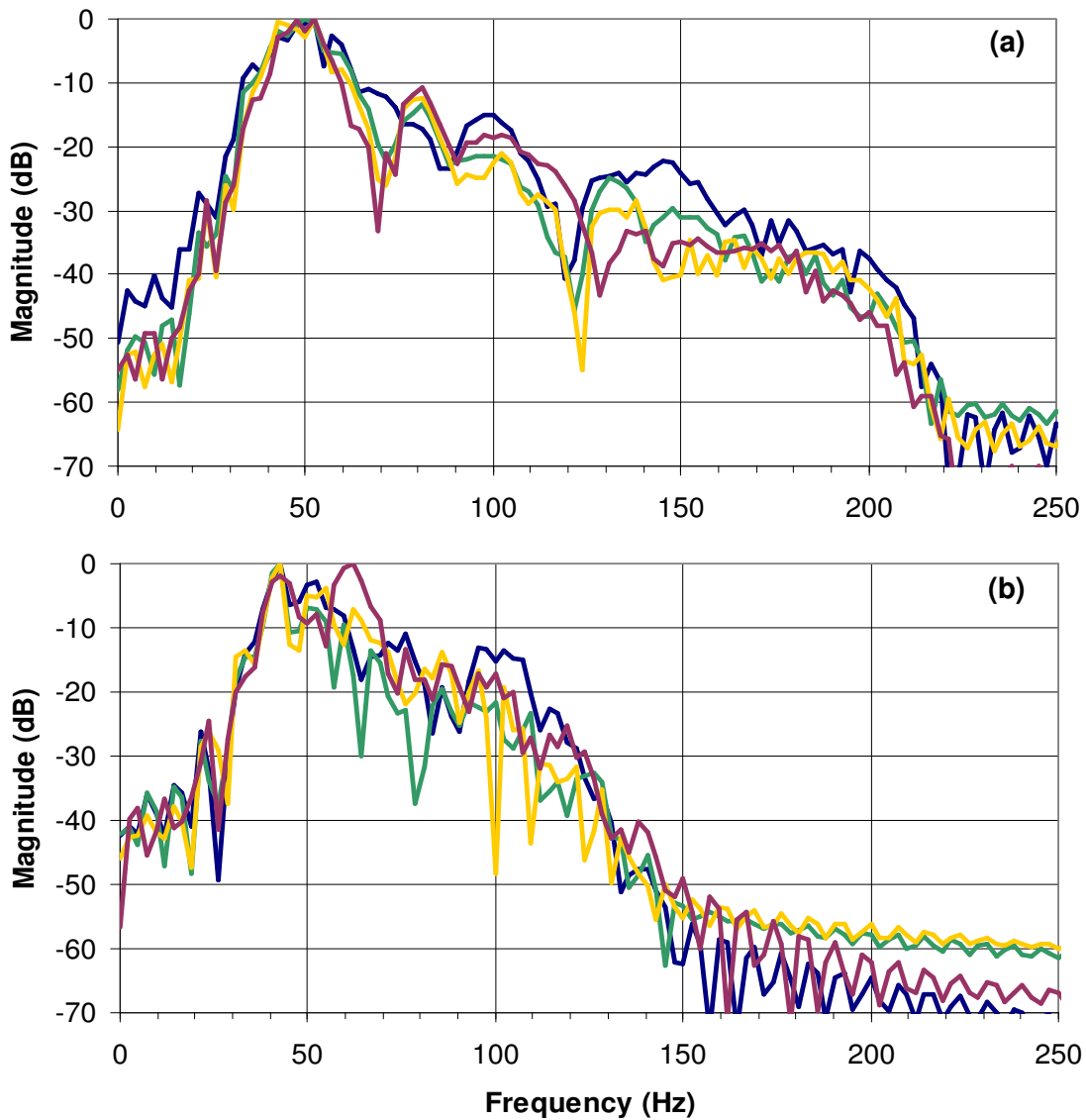


Figure 2.11 Representative (a) P-wave and (b) PS-wave signal spectra for Line A determined by conducting frequency analysis over small data windows in which the desired P and PS reflection energy is dominant. Acquisition using the 40 Hz geophones with a 40 Hz low-cut filter means that both P and PS signal drops away rapidly below 40 Hz. (Compare with the P and PS signal spectra in Figure 2.10.)

CHAPTER THREE PS-WAVE BEHAVIOUR

3.1 Introduction

Since our first converted-wave seismic trials in the Bowen Basin (ACARP Project C10020), we have observed anomalous behaviour – manifested as differences in wave behaviour (e.g. amplitude, traveltimes) as a function of direction of travel – in our PS data. While our converted-wave data processing is designed to simply work around some of the more obvious peculiarities, little effort has been devoted to understanding the cause of this behaviour or the impact, if any, it has on the PS seismic image. As part of Project C13029 we have investigated this anomalous behaviour in greater detail. This chapter describes the different types of anomalies we observe in our PS data, explores possible causes of such behaviour, and suggests how we can take advantage of our new understanding now, and in the future, to enhance converted-wave imaging and/or improve geological characterisation of the sub-surface using PS data.

3.2 The Propagation of PS Waves in the Sub-Surface

Recall that compressional (P) and shear (S) seismic waves propagate differently through the sub-surface. This is illustrated by the schematic in Figure 2.1. P waves are longitudinal waves that have particle motion in the direction of travel. In contrast, S waves are transverse waves that have particle motion perpendicular to the direction of travel.

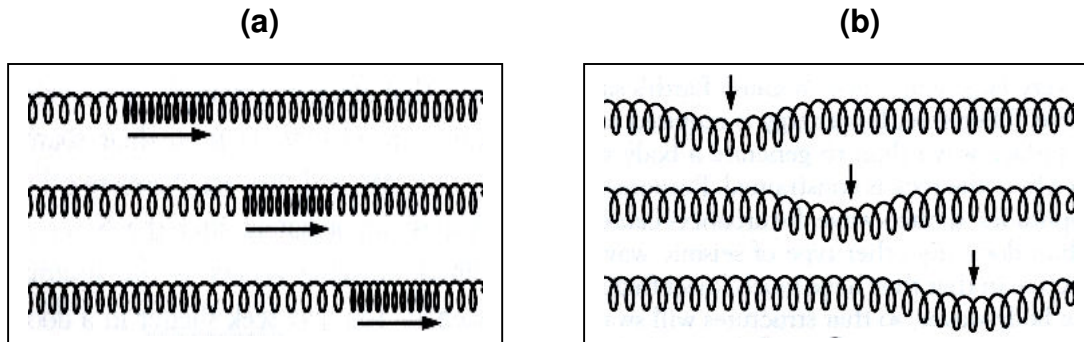


Figure 3.1 Ground vibrations associated with (a) P-waves and (b) S-waves. In this schematic, the seismic waves are travelling from left to right. The particle motion of the P wave is in the direction of travel. The particle motion of the S wave is perpendicular to the direction of travel.

The different modes of propagation of P and S waves mean they travel at different speeds through the earth, and respond differently to various geological situations. For example, S waves typically travel at about half the speed of P waves, with the precise P-wave to S-wave velocity ratio (V_p/V_s) dependent on lithology (Table 3.1). In addition, P waves are influenced by pore space and/or fluid and gas saturation, while S waves are not. This is because S waves will only travel in solid materials. Consequently, in comparison to P waves, S waves are far more sensitive to the actual lithologies through which they travel.

Table 3.1 Typical V_p/V_s values (after Domenico (1984) and Stewart (2003)).

Rock Type	V_p/V_s
Coal	2.5-2.7
Shale	1.9-3.0
Limestone	1.8-2.0
Dolomite	1.7-1.8
Sandstone	1.6-1.7

Since PS waves travel down as P waves and up as S waves, and the two wave types respond differently to any geology they encounter, in a heterogeneous earth (e.g. lateral velocity variations, reflector dip, and anisotropy), when source and receiver positions are interchanged, the resultant PS reflection events will exhibit different amplitude, phase and/or arrival times. In practice, we observe asymmetric amplitude and moveout in pre-stack common-conversion point (CCP) gathers, and/or different two-way traveltimes (TWT) structure or reflection amplitudes in the positive- and negative-offset PS sections. These characteristic responses of PS waves are explored further below.

3.3 Diodic Moveout

Normal moveout (NMO) is the variation of the arrival time of reflection energy with source-receiver offset. In the case of laterally uniform velocity and structure, positive- and negative-offset traces in a common-conversion point (CCP) gather will exhibit symmetry in the moveout of a PS reflection event. In practice, symmetric normal-moveout is approximately maintained even when modest and smooth lateral inhomogeneities are present. However, because of the two types of waves (P and S) that travel along a converted-wave raypath, in laterally heterogeneous media a PS reflection event recorded on the positive-offset traces of a CCP gather can have a different moveout to the same event recorded on the negative-offset traces.

Figure 3.2 illustrates one scenario that can result in the asymmetric moveout of a PS reflection event. In the simple schematic, both PS waves are imaging the same sub-surface point. However, the reflection event on the positive-offset trace will have a delayed arrival time compared to the negative-offset trace, because the S-wave raypath for the energy recorded on the positive-offset trace is longer. (Note that, the P-wave raypaths are also different lengths for the two raypaths shown, but because P-wave velocities are much faster than S-wave velocities, this has relatively little effect on the travel times of the P energy.) Asymmetric moveout can also arise from irregular zones of lithology or from sub-surface anisotropy (where the propagation velocity of the S wave becomes dependent on the direction it travels through the rock). Asymmetry in the arrival times of PS reflection energy on the positive- and negative-offset traces of a CCP gather is referred to as diodic moveout (a term recalling the electronic diode which operates differently in forward and reverse) (Thomsen, 1999). Note that, diodic moveout does not occur for P waves (or for any other pure-mode event) since the positive- and negative-offset raypaths to the one sub-surface reflection point would be the same.

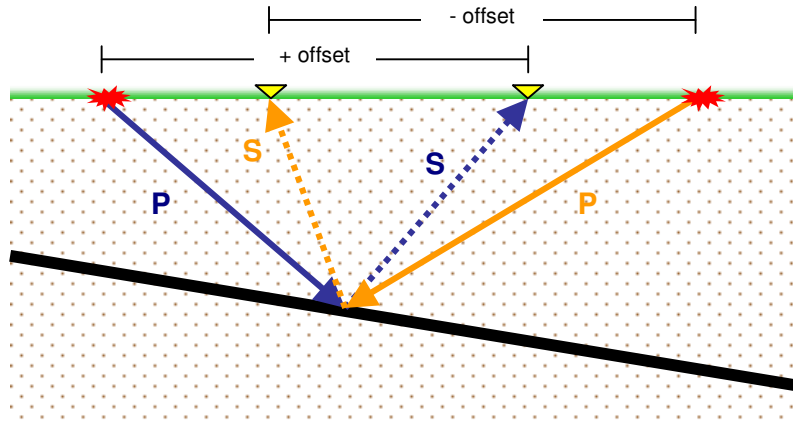


Figure 3.2 Schematic to illustrate the diodic effects of a dipping geological layer on PS reflection events. Here, PS waves recorded on positive (+) offset traces (represented by blue arrows) will have S-wave raypaths longer than the corresponding PS waves recorded on negative (-) offset traces (represented by the orange arrows). Thus, down-dip traces will exhibit slower traveltimes than up-dip traces, resulting in asymmetric or diodic moveout in CCP gathers.

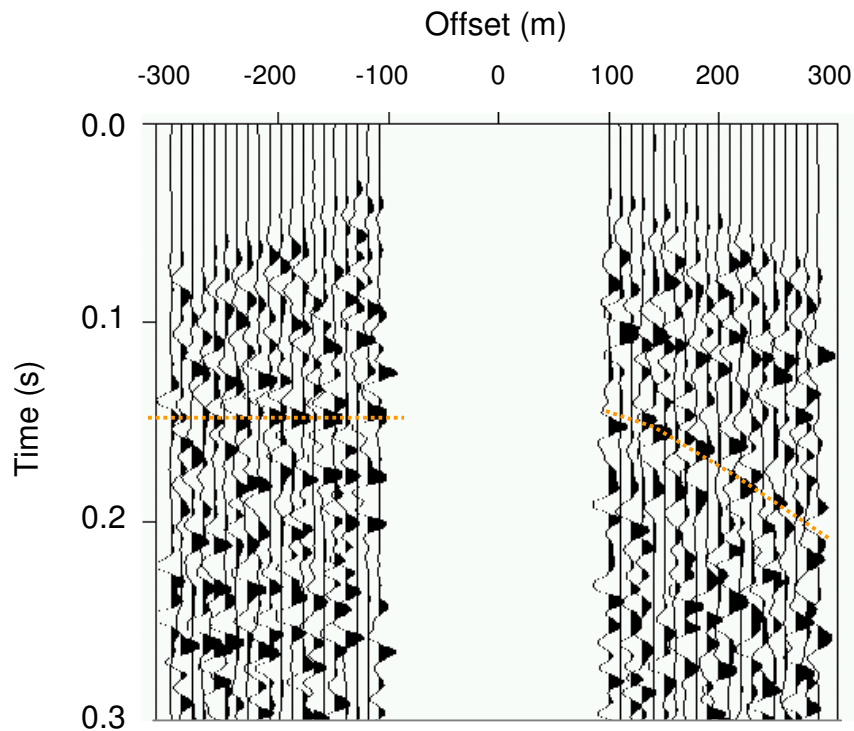


Figure 3.3 A real NMO-corrected CCP gather acquired over a dipping coal seam. The PS reflection events (indicated by the dashed orange lines) exhibit diodic moveout. The single V_p/V_s function used here to correct for NMO is only effective for negative-offset traces. A second V_p/V_s function is required to properly flatten the PS reflection event on the positive-offset traces.

Figure 3.3 illustrates diodic moveout on a real CCP gather. Here, the CCP gather has been NMO-corrected using one V_p/V_s function that is suitable for the negative-offset traces. Obviously, a different V_p/V_s function is required to flatten the PS reflection events on the positive-offset traces. Diodic moveout has been consistently observed in all of our 3C seismic datasets. It means that it is essential to treat positive- and negative-offset traces separately during velocity analysis for PS NMO correction.

3.4 Diodic Illumination

In the case of extreme lateral inhomogeneities in the sub-surface, it is possible for a PS reflection event to look significantly different on the positive- and negative-offset stacked PS sections (in terms of amplitude and/or TWT structure). This behaviour can be described as diodic illumination. A classic example from the oil industry considers a large gas cloud in the sub-surface (e.g. Li *et al*, 2000). If a downgoing P wave has to travel through the gas cloud to reach a particular sub-surface reflection point, the upgoing S wave will be very weak, if not absent (since P waves are severely attenuated by gas). On the other hand, if a downgoing P wave travelling in the opposite direction to reach the same sub-surface reflection point doesn't have to go through the gas cloud, the resultant upgoing S wave will be very strong. The corresponding positive- and negative-offset PS sections would show a strong reflection event for one set of offsets, while the other would show a weak or non-existent PS reflection event. As for diodic moveout, we don't get this effect for pure-mode reflection events (e.g. P waves), because the same wave type travels along both portions of the raypath when the source and receiver locations are interchanged.

While we don't expect to get such high concentrations of gas in the coal environment to cause the type of effect described above, we believe we can get strong local variations in S-wave velocities that can at least change the traveltimes between positive- and negative-offset PS sections. This type of diodic illumination is clearly illustrated with data from Trial #3. Figure 3.4 shows the positive- and negative-offset PS sections for a small portion of the line. From station 260 the traveltimes of the target reflection events on the positive-offset stack (Figure 3.4(a)) are consistently earlier than the corresponding reflection events on the negative-offset stack (Figure 3.4(b)). It is believed that a very clean sandstone channel sitting above the two coal seams marked in Figure 3.4 (identified in nearby borehole data) is 'pulling up' the PS reflection events on the right-hand edge of the survey line (i.e. when the upgoing S wave passes through the sandstone channel, it speeds up and significantly reduces the overall traveltime of the PS reflection). In the case of the negative-offset traces, the upgoing S energy does not pass through the sandstone channel. Figure 3.5 gives a schematic of the type of geological scenario that could result in the traveltime responses observed in Figure 3.4.

Note that, diodic illumination makes it impossible to sum positive- and negative-offset traces during CCP stacking. One simple procedure to work around this diodic nature of PS waves is to process each one-sided CCP gather independently and join the resultant positive- and negative-offset sections at places of convenience to produce a single final PS section (Thomsen, 1999). This is the approach we have used to date.

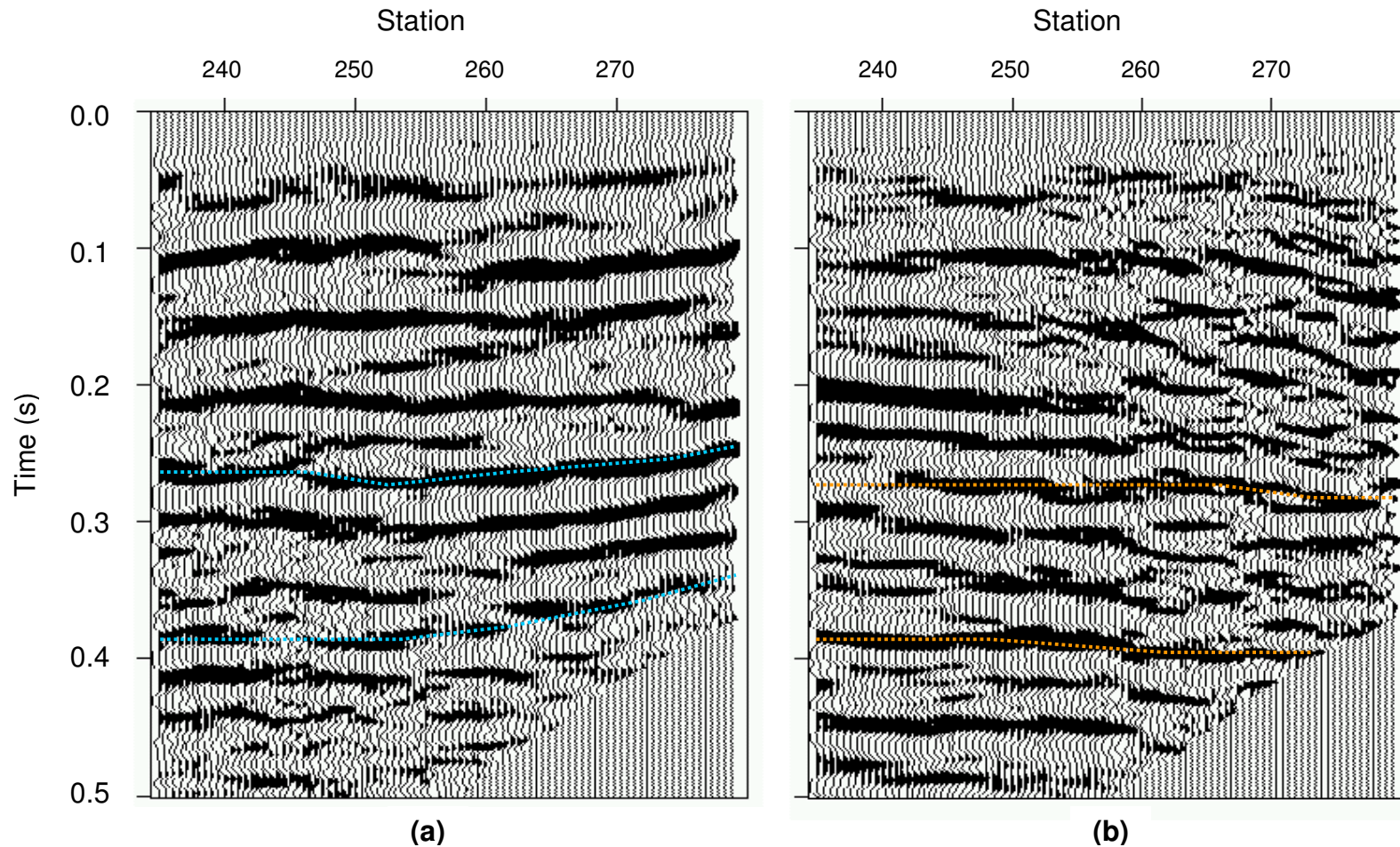


Figure 3.4 Portion of (a) positive-offset PS section and (b) negative-offset PS section from Trial Dataset #3 demonstrating diodic illumination. Target coal-seam reflection events are indicated. The arrival times of the positive-offset PS reflection events become earlier than the corresponding reflection events on the negative-offset stack from approximately station 260. Figure 3.5 illustrates a possible geological scenario that could result in this seismic response. Note that the line ends at station 280. It is expected that the negative-offset traces would start to be influenced by the same geological anomaly as the positive-offset traces just beyond the end of the line.

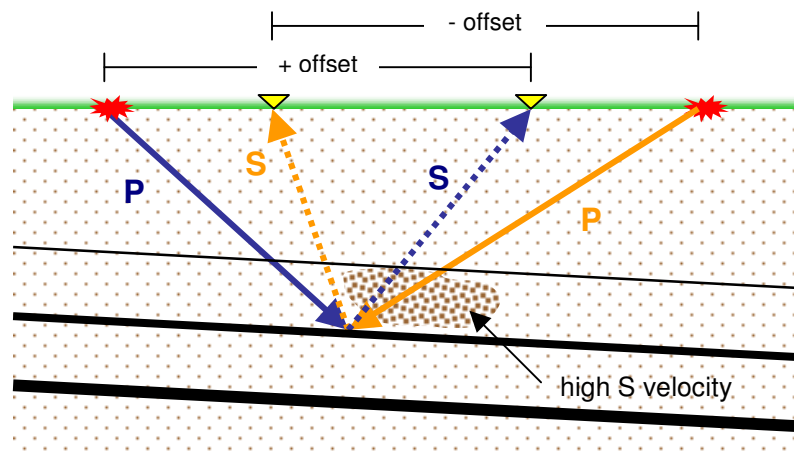


Figure 3.5 Schematic illustrating one geological scenario that could result in the positive- and negative-offset PS stacks given in Figure 3.4. Here, the upgoing S wave of the positive-offset raypath (blue) is travelling through a body of high V_s (e.g. clean sandstone), resulting in faster traveltimes. In contrast, the negative-offset PS reflection raypath (orange) is not influenced by the high- V_s material.

3.5 Improving PS-Wave Processing

Our current practice of treating the positive- and negative-offset traces independently during PS NMO, CCP binning and stacking is a significant step towards successfully accommodating the diodic nature of PS waves. However, full compensation for the PS-wave behaviour requires pre-stack depth migration, which in turn needs an accurate macro-velocity model. This is likely to be too computationally expensive and impractical for PS imaging in the coal environment. A simple alternative however, is to perform dynamic CCP binning that accommodates anisotropy, and post-stack PS migration. To date, Velseis has not implemented either of these processing methodologies. It is common knowledge that without migration, conversion-point dispersal and the positioning of features in the PS section are not accommodated properly. What we have only just recently come to appreciate is the sensitivity of S waves to inhomogeneities (including anisotropy) in the earth. Our investigation into PS-wave behaviour, together with recent processing results from Trial #2 (Chapter 6) and Trial #3 (Chapter 7), provides growing evidence that, in order to improve our PS sections, we may need to use a CCP-binning procedure that will accommodate anisotropy. We expect to implement both PS migration and anisotropic CCP binning in the near future.

3.6 Improving PS-Wave Interpretation

The most significant outcome of this investigation into PS-wave behaviour has been the realisation that, rather than treating mismatched positive- and negative-offset PS sections as a problem, we may be able to take advantage of their peculiarities to yield more information about the sub-surface. Consider, for example, the data shown in Figure 3.4. In this case, the positive- and negative-offset PS sections suggest two different geological interpretations. Understanding the concept of diodic illumination helps us to realise that the differences in the two PS sections could possibly reflect real geology rather than processing artefacts. Integrated interpretation of

both PS sections, instead of just the single final PS section comprising portions of positive- and negative-offset CCP traces, can reveal significant geological detail. This suggests that, in situations where significant lateral heterogeneities are expected, interpretation of PS data may be enhanced if we consider both the un-migrated positive- and negative-offset PS sections.

One final thing to note is that, while we are working with final PS sections that are created from portions of un-migrated positive-offset and negative-offset CCP traces, care must be taken when interpreting the location of structural features. As noted in the previous section, it is well understood that without migration the positioning of features in the PS section is not accommodated properly. This is illustrated using synthetic PS data in Figure 3.6. The true earth model is shown in Figure 3.6(a). The true fault locations are marked on the positive- and negative-offset seismic sections (Figures 3.6(b) and 3.6(c), respectively). Clearly both stacks image the two faults away from their true location (in this example, there is anywhere from 5 m to 60 m lateral error). Further, the two seismic sections show the faults at different locations from each other. The positive-offset stack tends to shift features towards the lower station numbers, and the negative-offset stack tends to shift features towards the higher station numbers – as highlighted by the image of the fault on the left side of the synthetic data. Note that, the same holds true for the fault on the right. However, the effect of the dip of the horizon superimposes an additional shift of the structure down-dip (migration tends to move dipping reflectors in the up-dip direction). Consequently, fault locations determined from our current PS-wave sections will be in error (and inconsistent with P-wave interpretation results). Based on knowledge of local dip, and whether or not positive- or negative-offset traces have been used to image the fault, it should be possible to approximate the direction of error in each interpreted fault location. However, the magnitude of the error in fault locations derived from un-migrated PS data will be data dependent (with larger errors for areas of steeper dip, and smaller errors for relatively horizontal reflection events). Note that, the relative shifts in the location of the structures imaged in our PS sections should not be an issue once PS migration is implemented.

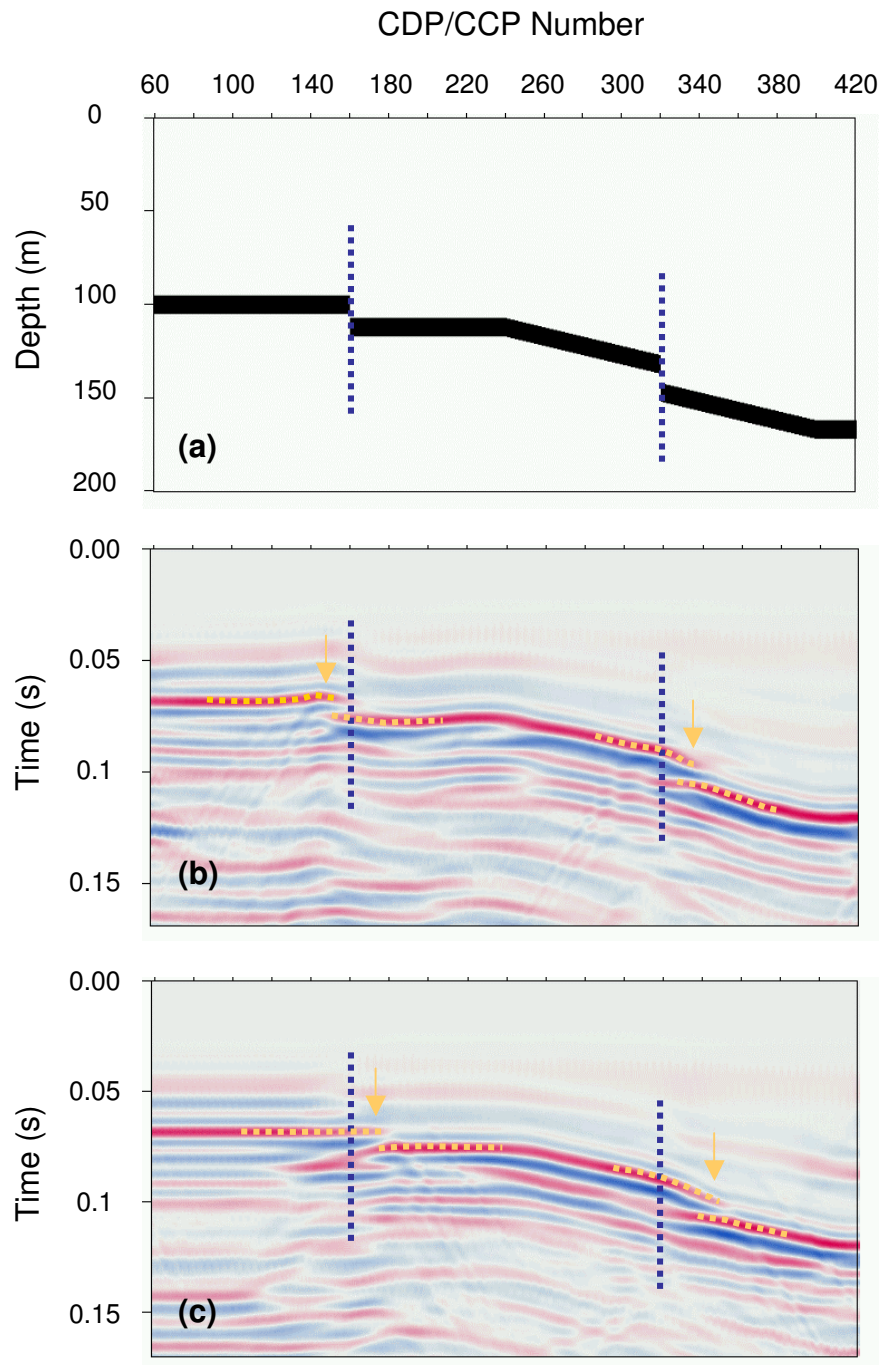


Figure 3.6 (a) Simple synthetic earth model comprising one 10m-thick coal seam. The coal seam is cut by two structures – one with a throw of 12 m (where the seam is horizontal), and one with a throw of 15 m (where the seam is dipping at an angle of 5.7° to the horizontal). (b) Final positive-offset PS stack and (c) final negative-offset PS stack corresponding to the earth model in (a). True fault locations are marked by the dashed blue lines. Interpreted fault locations are marked by the yellow arrows.

CHAPTER FOUR

ADVANCES IN CONVERTED-WAVE PROCESSING METHODOLOGY

4.1 Introduction

The processing of converted-wave coal-seismic data is a relatively immature technology. Experimentation to adapt and fine-tune PS processing methodology developed within the petroleum sector is ongoing to ensure optimum handling of our shallow, high-resolution 3C data. This chapter summarises the key advances we have made in converted-wave processing methodology since the completion of ACARP Project C10020, and reviews our ongoing investigations into vector processing. Note that, not all of the converted-wave data presented in this report have been processed using all of the algorithms described here, since changes to our PS processing sequence have evolved over the duration of this research project. Note also, our investigations into PS-wave behaviour (Chapter 3) and recent PS processing results strongly suggest there is potential for further improvement in our PS processing flow. We recognise that our current 'best practice' approach to processing converted-wave data is very likely to change, and a number of recommendations for future work are included here.

4.2 S-wave Receiver Statics

Statics are the time delays introduced in the seismic data due to the varying thickness of the low-velocity weathering layer. Ideally, processing removes these effects so arrival times of reflection events are what would have been observed if seismic acquisition had been undertaken on a flat plane with no weathering or low-velocity material present.

A PS wave will pass through the weathering layer twice – once on the way down as a P wave, and once on the way up as an S wave. Static corrections to compensate for delays in the downgoing P wave are computed conventionally using the vertical component of the seismic data (e.g. Yilmaz, 1987). Static corrections for the upward travelling S wave do not generally exhibit a simple mathematical relationship with the P static corrections. This is due to the difference in effective thickness of the weathering layer that is 'seen' by P and S waves, and the fact that S-wave velocities can be up to ten times slower than for P waves in the surface layer. Consequently, alternative calculations must be undertaken to determine the necessary S-wave receiver static correction. If suitable S-wave receiver static corrections are not computed, the quality of the resultant PS section will be degraded.

Our early attempts to compute S-wave receiver static corrections utilised a manual common-receiver gather (CRG) stack method based largely on the S static method of Cary and Eaton (1993). However, their assumption that very little structure should affect the PS reflection event used to define the static corrections was generally too limiting for our data. Typically, our coal-seismic data image dipping and faulted geological layers. Consequently, the required normal-moveout (NMO) correction of receiver gathers was extremely ambiguous, and the resultant CRG stack was highly variable (resulting in S-wave receiver static corrections with low repeatability). The strong dependence on V_p/V_s of the PS reflection character in the CRG stack meant that even multiple

iterations of receiver static computations often didn't improve the static correction (and could actually degrade the static solution!).

In an attempt to improve the quality of our PS sections, a new S-wave receiver statics method has been developed. Two key design features were (i) to remove the need for NMO correction of common receiver gathers, and (ii) to remove the requirement that no structure or dip affect the PS reflection events. Details of the new S-wave receiver statics method are given in Appendix A. Essentially, the TWT of a selected PS reflection event is picked on every common-offset receiver section following P-wave source static corrections. Variations between the TWT picks from all of the common-offset sections can then be attributed to PS normal-moveout, CCP structure and S-wave receiver statics. The S-wave receiver statics component of the TWT variations is solved for in a least-squares sense. As for the processing of conventional P-wave data, the short-wavelength S receiver static corrections are then applied to the pre-stack data (to shift data to a temporary processing datum), while the long-wavelength receiver static corrections (and elevation static corrections) are applied to the post-stack data (to shift section to the final datum).

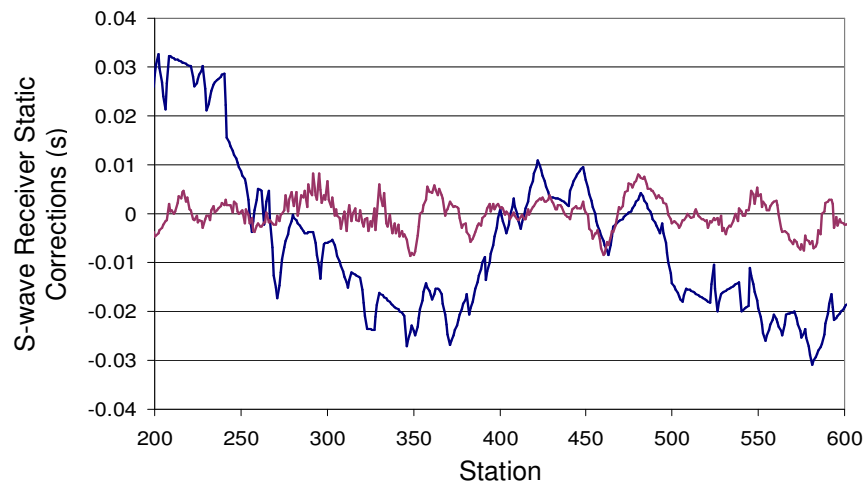


Figure 4.1 Comparison of S-wave receiver static corrections computed using our original statics approach (blue) and our new statics method (maroon) for Line C.

Figure 4.1 compares the new pre-stack S-wave receiver static corrections with those computed using our original approach, for a commercial 2D-3C seismic line (Line C) acquired by Velseis in 2004. High-frequency differences between these two functions highlight problems associated with the old method requiring NMO correction of gathers of traces that don't share the same sub-surface conversion point. The low-frequency differences between these two functions reflect the different ways in which the two static-correction methods accommodate structure and long-wavelength statics. The robustness of the new S-wave receiver statics method is illustrated in Figures 4.2 and 4.3, where comparisons of shot records with no static corrections, original S static corrections and new S static corrections reveal that the new static-correction methodology yields superior shot records.

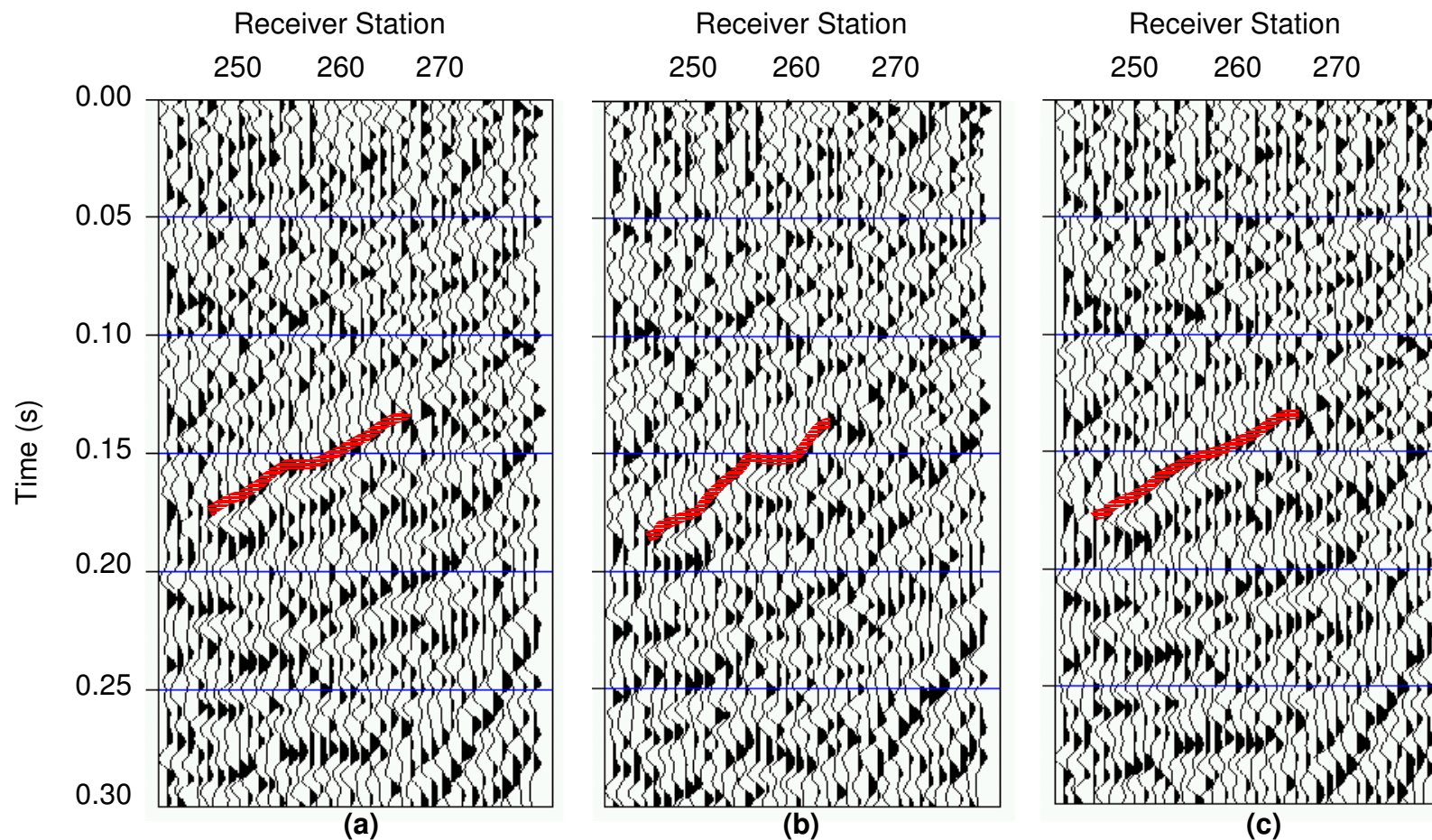


Figure 4.2 Inline component of representative shot record (Shot 302) from Line C: (a) with no S-wave receiver static corrections; (b) with S-wave receiver static corrections derived from our original statics approach; and (c) with S-wave receiver static corrections derived from our new statics method. A dominant coal-seam PS reflection event is highlighted. The new statics method is most successful at removing time delays associated with the weathering layer (i.e. at removing trace-to-trace TWT variations along the event). Note that, these data have had spherical divergence correction, P source static corrections, deconvolution, and spectral whitening applied to them.

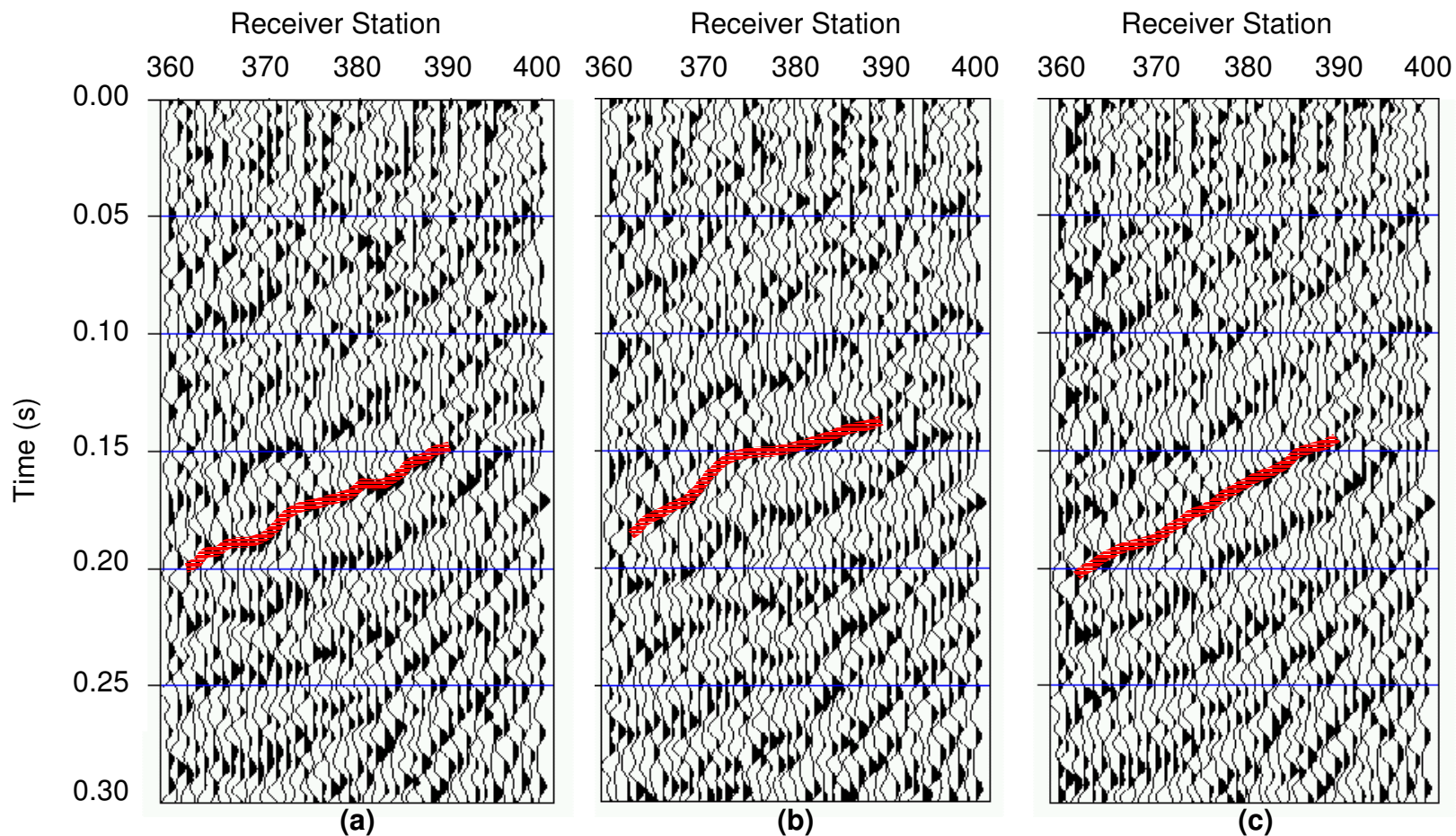


Figure 4.3 Inline component of representative shot record (Shot 418) from Line C: (a) with no S-wave receiver static corrections; (b) with S-wave receiver static corrections derived from our original statics approach; and (c) with S-wave receiver static corrections derived from our new statics method. A dominant coal-seam PS reflection event is highlighted. The new statics method is most successful at removing time delays associated with the weathering layer (i.e. at removing trace-to-trace TWT variations along the event). Note that, these data have had spherical divergence correction, P source static corrections, deconvolution, and spectral whitening applied to them.

4.3 CCP Binning

The raypath of a PS wave through the earth is asymmetric. This is because the upwards travelling S wave travels more steeply than the downgoing P wave. Consequently, the sub-surface reflection point of a PS wave is offset from the midpoint of the source and receiver, towards the receiver. The precise location of the point at which the P wave converts to an S wave is actually a function of V_p/V_s and the depth of the reflector (Figure 4.4).

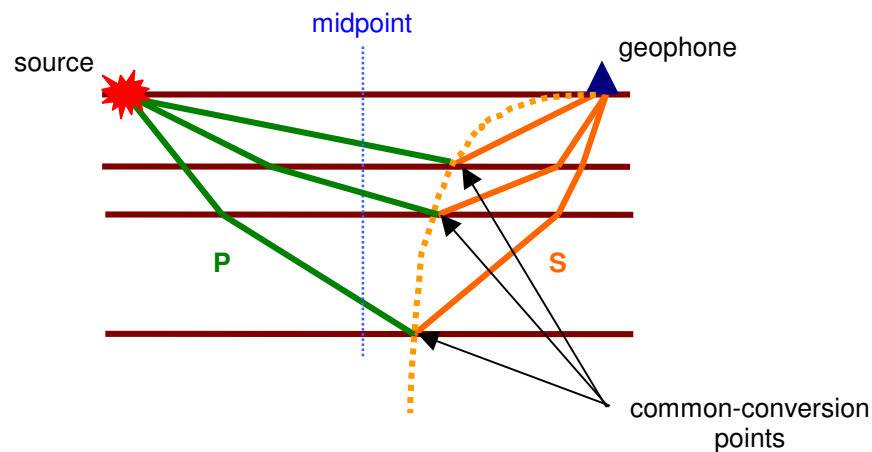


Figure 4.4 The reflection (or conversion) points of a PS wave travelling between a given source and receiver will vary with velocity and reflector depth.

A critical step in converted-wave processing is to collect together traces that share the same P-to-S conversion point – this is referred to as common-conversion point (CCP) binning. Practical experience has demonstrated that ‘dynamic’ CCP binning (Zhang, 1996) yields the best results for shallow, high-resolution converted-wave imaging. This approach to CCP binning allocates each sample down each trace to a CCP bin according to its TWT and the local V_p/V_s value. Thus portions of seismic traces can be assigned to different CCP bin locations.

Our preference for ‘dynamic’ binning has evolved during the course of this research project so that, despite the relatively expensive computational times of the algorithm, the method is now used routinely on all of our 3C coal-seismic datasets. Note however, further software development has been undertaken to improve the accuracy and logistics of the CCP-binning phase of the converted-wave processing flow. Specifically, our V_p/V_s functions used for binning can now be keyed on CCP number rather than station location (this improves accuracy of our V_p/V_s analysis); data samples are now stacked into a CCP bin without relative weighting, and PS NMO is not applied during the CCP-binning process (this enables pre-NMO processing of CCP gathers). A summary of the practical implementation of our current CCP-binning algorithm is given in Appendix B. An example of the benefits of ‘dynamic’ binning over ‘horizon-based’ binning on the converted-wave stack is given in Section 4.6.

Note that, our investigations into PS-wave behaviour (Chapter 3) have highlighted the sensitivity of PS waves to heterogeneities (including anisotropy) in the earth. This, coupled with recent processing results from Trial #2 (Chapter 6) and Trial #3 (Chapter 7), indicates that accommodation of anisotropy in the CCP-binning algorithm may be necessary for further improvement in our PS stacks. Thomsen (2002) describes an iterative CCP-binning procedure that allows a different V_p/V_s function to be used for the PS NMO and CCP-binning components of the PS processing flow. In this way, the significant influence of anisotropy on PS waves can be accommodated. It is recommended that this procedure be implemented and trialed in the near future.

4.4 Post-Stack Noise Attenuation

Typically our inline seismic data records suffer from greater noise contamination than the corresponding vertical-component records. Consequently, our PS sections tend to suffer from a poorer signal-to-noise ratio than our conventional P-wave images. To help boost the signal-to-noise ratio of our PS sections, we have introduced an additional post-stack noise removal algorithm to our converted-wave processing flow. Here we use eigenvector filtering – a method that involves the singular value decomposition (SVD) of the stacked seismic data. SVD decomposes the stacked data into the sum of a series of weighted, orthonormal eigenimages. The contribution of a particular eigenimage in the reconstruction of the input data is proportional to its weighting factor (also called the singular value). It is possible to partially reconstruct the input data using only the most dominant eigenimages. In general, this will enhance any signal that has maximum trace-to-trace coherence, and will reduce random noise. The details of the eigenvector filtering algorithm are given in Appendix C. Figure 4.5 shows the PS section for Line C before and after eigenvector filtering, and the difference between the two sections. It is obvious that significant random noise has been removed from the PS stack by the eigenvector filter.

4.5 Vector Processing

Our converted-wave processing flow makes the assumption that the vertical component of data contains only P-wave energy, and the inline component of data contains only PS-wave energy. Vector processing, inserted into the PS processing flow prior to any other step, has the potential to yield purer P and PS records when this assumption fails (i.e. when there is cross contamination of P energy onto the inline component of data, and S energy onto the vertical component of data). This is likely to occur on far-offset traces (where raypaths are non-vertical), and will be more significant in areas with relatively high-velocity surface layers (e.g. areas with surface basalts).

As part of Project C10020, we illustrated synthetic vector-processing results for a technique referred to as Parametric Inverse Modelling (PIM) (Velseis, 2003; Hendrick, 2001). However, we concluded that, while the vector-processing method could be used to yield purer P and PS pre-stack gathers, no significant differences could be observed between the resultant pure P and PS stacked traces, and the regular vertical- and inline-component stacked traces.

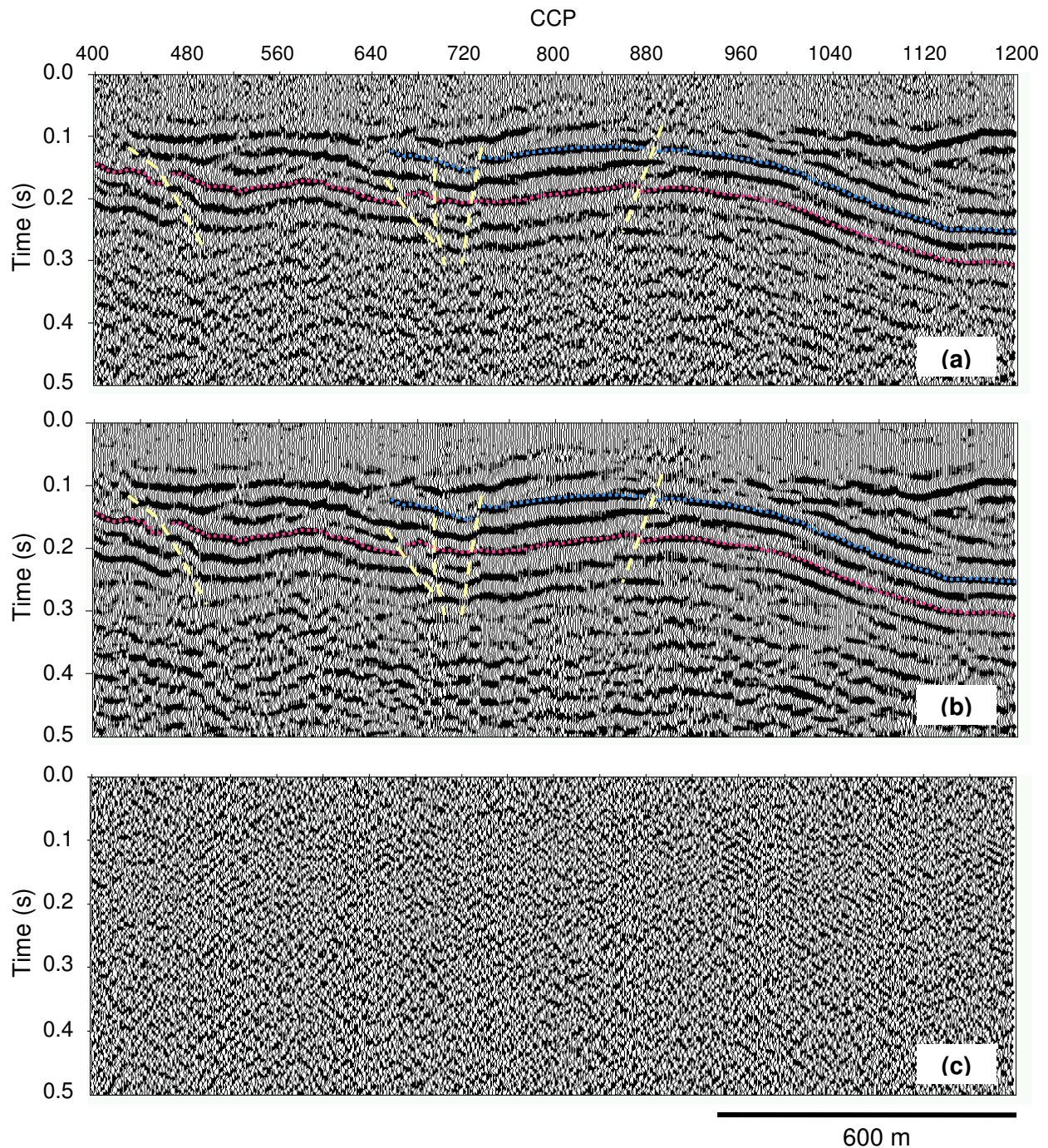


Figure 4.5 PS seismic section for Line C: (a) before and (b) after eigenvector filtering. A running trace window of 120 was used to decompose the data into eigenimages. The first 12 eigenimages were used to reconstruct the 'noise-free' seismic section. The difference between the two sections is given in (c) and demonstrates that significant random noise has been removed by the eigenvector filter.

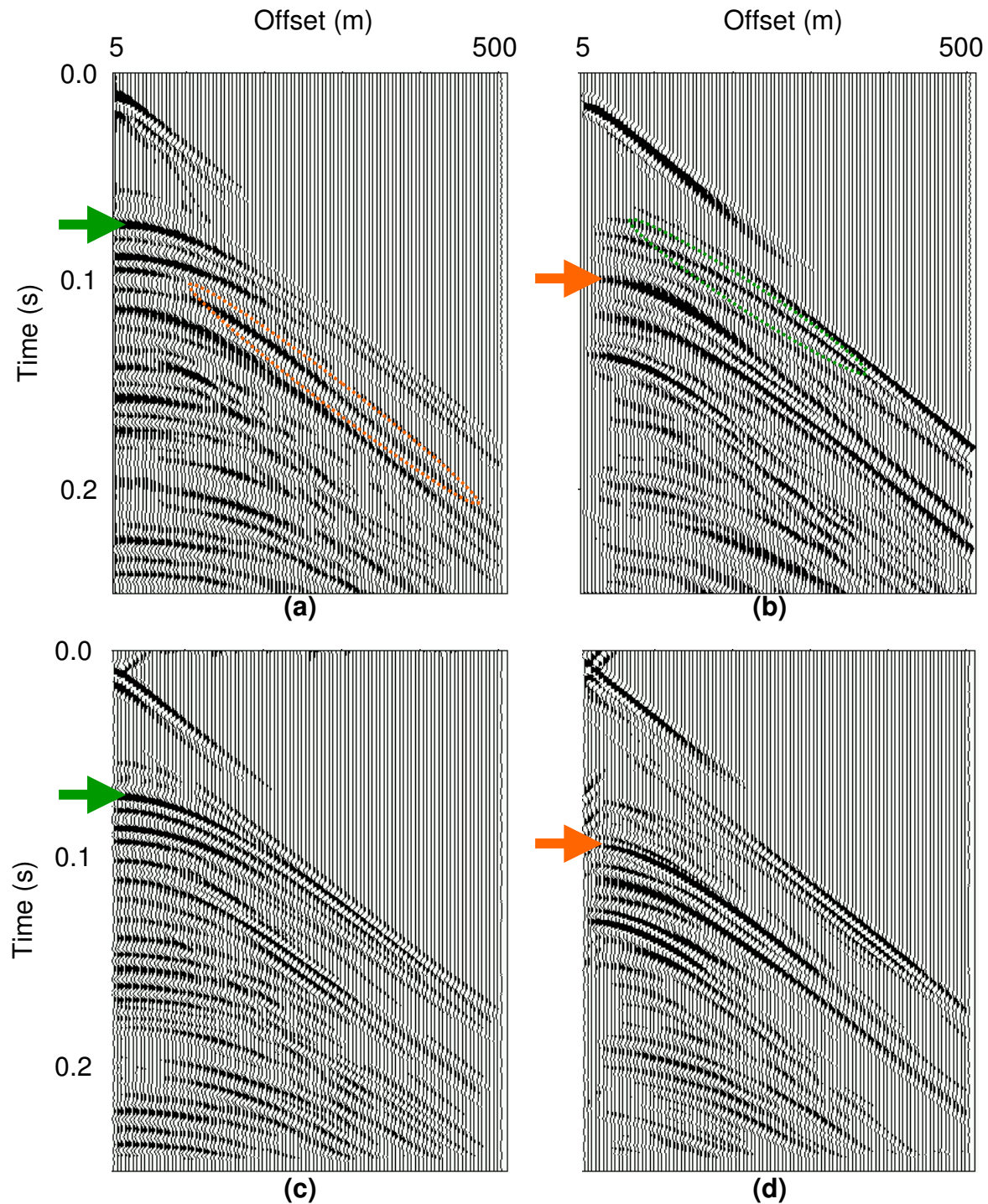


Figure 4.6 (a) Vertical component and (b) inline component of a synthetic shot record generated via elastic wave-equation modelling using a simple coal-scale earth model. The target P reflection event (green arrow) is dominant on the near offset traces of (a). However, there is also significant P energy (green ellipse) on the mid- to far-offset traces of (b). Similarly, the top-coal PS reflection event (orange arrow) dominates (b) on the near- to mid-offset traces. However, there is also cross contamination of PS energy (orange ellipse) on the far-offset traces of (a). (c) Pure P record and (d) pure PS record recovered via elastic wavefield decomposition (EWD). The cross-contaminating energy highlighted in (a) and (b) has been successfully attenuated.

As part of Project C13029, we chose to re-visit vector processing to assist in the processing of one particular dataset for which we had particular trouble obtaining a coherent PS reflection event. Based on our experiences with vector processing, we have tested an alternative vector-processing method referred to as Elastic Wavefield Decomposition (EWD) (Hendrick and Brand, 2006). It operates quite differently to PIM in that it considers an entire shot record at once, can accommodate velocity errors up to 10%, can handle static errors and tends to suppress random noise. Further details on EWD are given in Appendix D. Figure 4.6 demonstrates the ability of EWD to remove cross-contaminating P and PS energy from synthetic inline and vertical records, respectively. A real-data example is shown in Figure 5.1. As for PIM, the EWD vector-processing method does appear to be able to extract purer P and PS pre-stack gathers.

Contrary to our Project C10020 results, however, we do see differences in the stacked PS data following application of EWD (Figure 5.2). Note however, as discussed in Chapter 5, other differences in the production of the PS stacks in Figure 5.2 make it unclear which improvements can be attributed to EWD. Thus, we remain uncertain as to whether or not vector processing should be routinely incorporated into the converted-wave processing flow. Vector-processing is a topic of ongoing research.

4.6 Converted-Wave Processing Flow

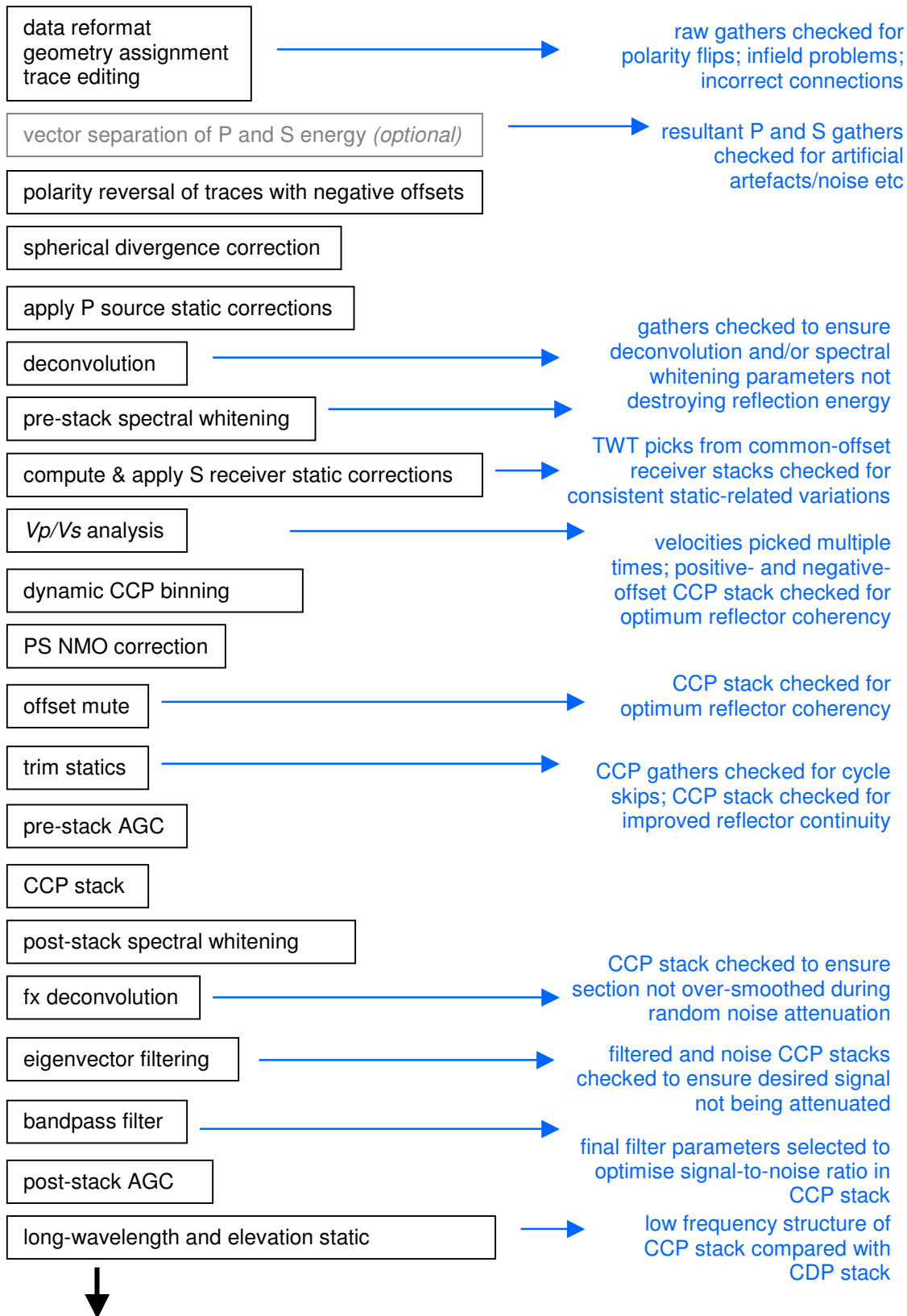
Figure 4.7 illustrates our current 'best practice' approach for processing converted-wave seismic data, and the quality-control procedures we have in place to ensure optimum results are being achieved.

Figure 4.8 compares the PS-wave stack for Line C generated using the best PS processing methodology available in 2004, and our current processing methodology. The significant changes to the S-wave receiver static corrections (Figure 4.1) are largely responsible for the greatly improved reflector coherency in the 2006 section (Figure 4.8(b)). The enhanced 'dynamic' CCP-binning algorithm has improved our final binning and NMO V_p/V_s function, and has helped better focus reflection energy down the full extent of each seismic trace in the 2006 section. In comparison, the horizon-based binning algorithm used in 2004 only attempts to focus reflectors close to the target seam. Eigenvector filtering has removed significant random noise from the 2006 section (as illustrated above in Figure 4.5). The end result is that the 2006 section (Figure 4.8(b)) gives a more robust image of the sub-surface, and subsequent interpretation results can be considered more reliable. We are confident that the processing advances we have made with respect to S statics, CCP binning and noise reduction are improving the outcomes of our PS seismic work.

As noted in Section 3.5, the priorities for further advancements in our PS processing flow are the implementation of PS migration and anisotropic CCP binning. We recommend that the latter be based on the work of Thomsen (2002) (as noted in Section 4.3).

PS Processing Flow

Quality Control



CONVERTED-WAVE STACK

Figure 4.7 Current PS processing flow and quality-control procedures.

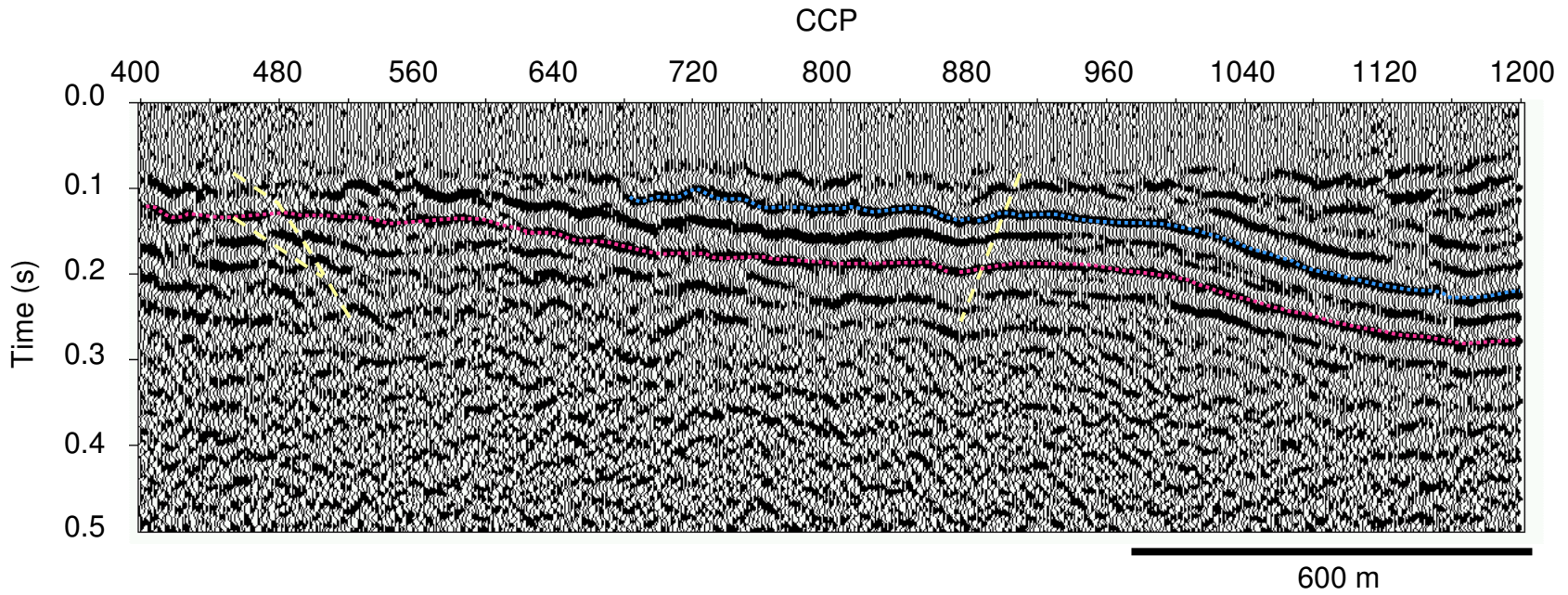


Figure 4.8 (a) PS section for Line C generated using the best PS processing methodology available in 2004. Reflection events associated with the two target coal seams are marked. Dashed yellow lines indicate interpreted structures.

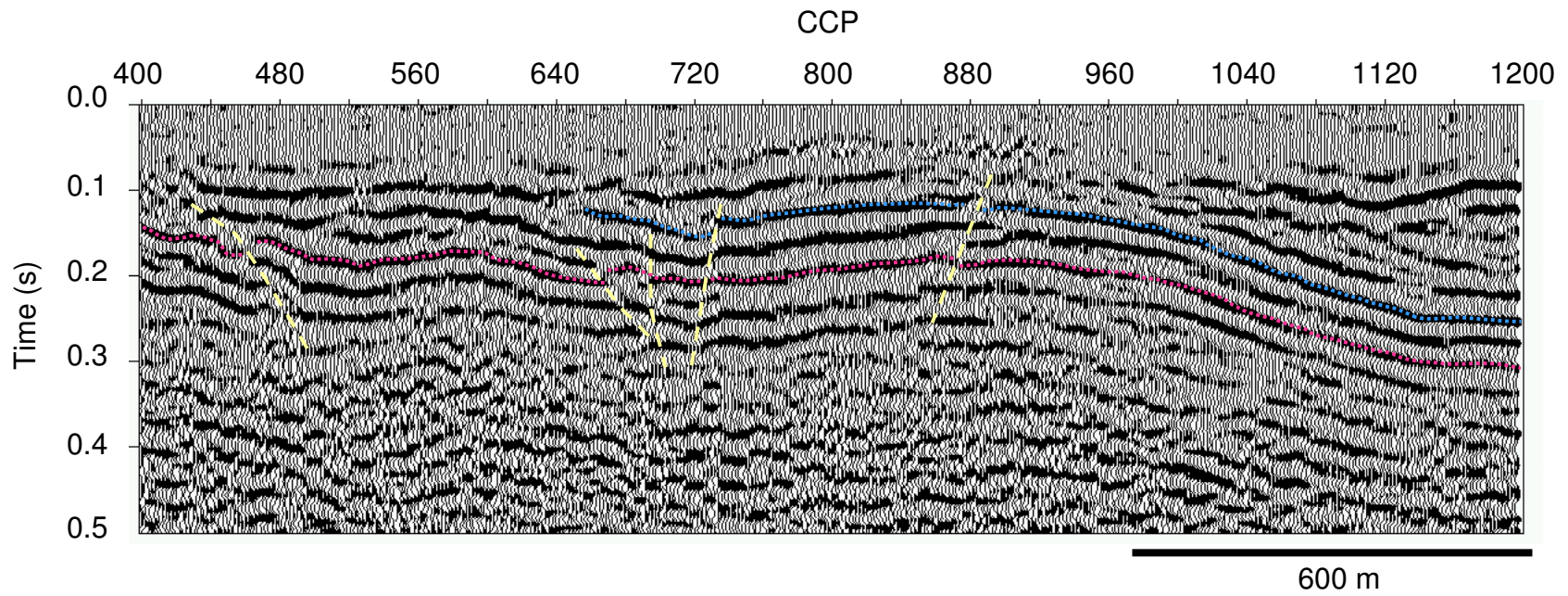


Figure 4.8 (b) PS section for Line C generated using the best PS processing methodology currently available. Reflection events associated with the two target coal seams are marked. Dashed yellow lines indicate interpreted structures.

CHAPTER FIVE

REAL-DATA TRIAL #1

5.1 Introduction

Trial Dataset #1 was acquired as part of ACARP Project C10020 in September, 2001. The data were acquired in an area with a single, thick coal seam at relatively shallow depths. Details of the original survey can be found in Velseis (2003). While the single-seam geology along this line excludes use of these seismic data for our integrated P/PS interpretation investigations (Section 8.2), the simple geology does make the dataset suitable for experimenting with PS processing options. This chapter presents results from a vector-processing trial conducted using this 3C dataset.

5.2 Reprocessing Results

As discussed in Section 4.5, vector processing has the potential to yield purer P and PS records when P and S energy cross contaminates the inline and vertical components, respectively. We are not convinced that significant cross contamination exists for this, or any of our coal 3C datasets. However, vector processing can also be implemented to simply strengthen and enhance P and PS reflection events relative to background noise. Given the difficulties we originally had with obtaining a coherent reflector for the Trial #1 PS stack (see original PS processing flow in Velseis (2003)), it was felt that vector processing of this dataset would be a valid experiment. [Although, note that we now believe at least some of our difficulties were associated with our original S-wave statics corrections.] Based on our experience with various vector-processing methodologies (Hendrick, 2001), Elastic Wavefield Decomposition (EWD) (Appendix D) was selected as a suitable option for this experiment.

Figures 5.1(a) and (b) show a representative raw vertical- and inline-component shot record from Trial Dataset #1. On the vertical component the P-wave reflection from the target coal seam is at 0.1 s at zero offset. The inline-component record reveals the corresponding target PS reflection event at 0.2 – 0.25 s on the centre traces. Figures 5.1(c) and (d) show the P- and PS-wave records extracted via EWD. On the P-wave record, the main P target reflector now dominates the record. Similarly, on the extracted S-wave record, the target PS event has been considerably enhanced relative to other energy.

Application of EWD to all shot records from this dataset has enabled extraction of a ‘pure’ PS section (Figure 5.2(a)). We believe this is the first published real-data example of EWD. Details of the complete PS processing sequence used to derive this PS stack are given in Appendix E. A comparable PS section, derived via the same processing sequence except for EWD, is given in Figure 5.2(b). A comparison of the two PS sections in Figure 5.2 demonstrates that application of EWD has helped focus the PS reflector, and results in slightly better reflector coherency and fault definition. However, despite this apparent improvement in the PS section following EWD, it is still not clear whether vector processing is an essential element of our PS-wave processing flow. We are now aware of the shortcomings in our original approach to S-wave statics (the original S-wave

statics method was used to generate the results shown here). The differences observed in the PS sections in Figure 5.2 may be more to do with the non-repeatability of the S static computation, than the success of EWD. The question as to whether or not vector processing should be routinely incorporated into the converted-wave processing flow needs to be re-examined following our recent advances in PS processing methodology (Chapter 4).

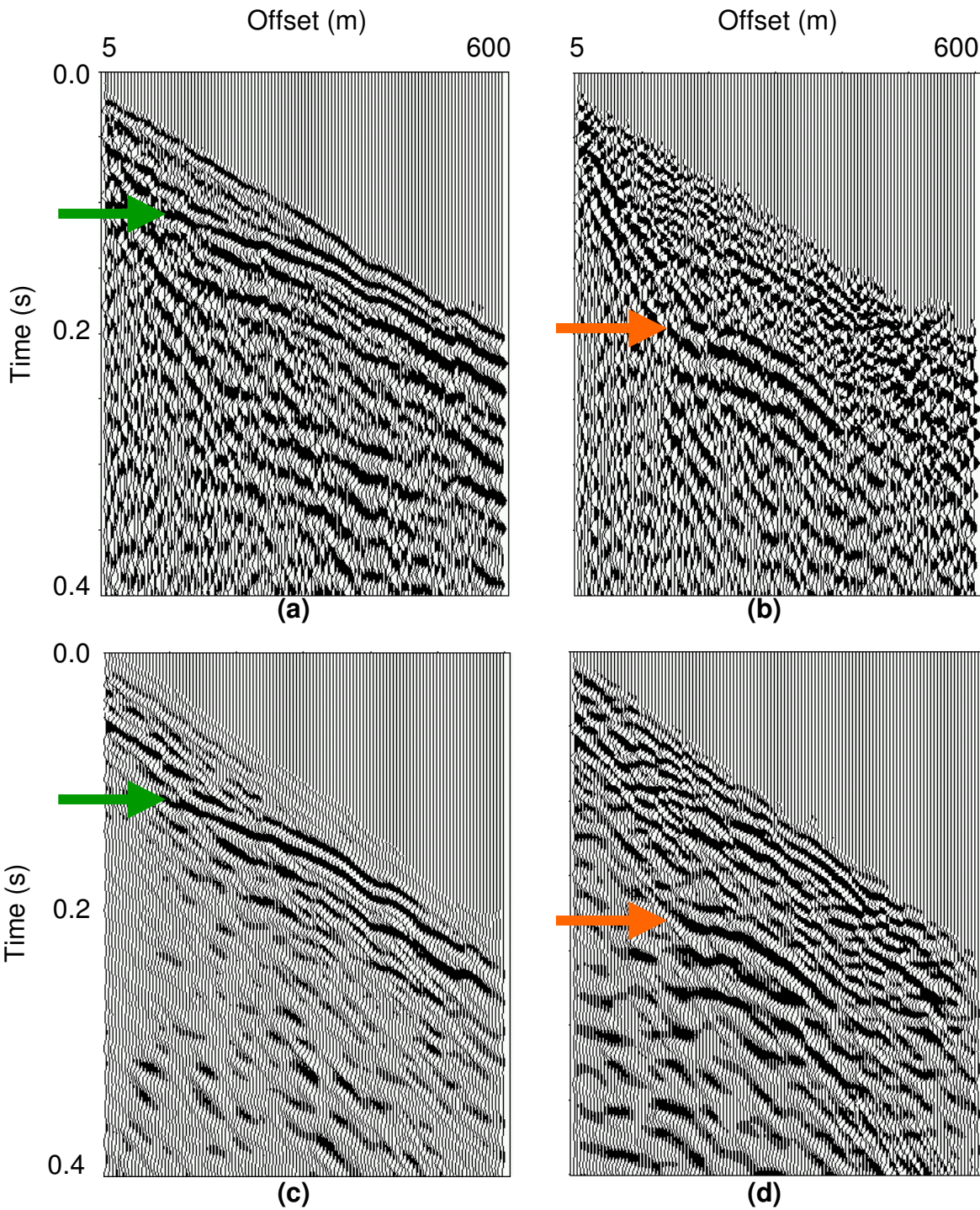


Figure 5.1 (a) Vertical and (b) inline components of a representative shot record from Trial Dataset #1. The target P and PS reflection events are indicated by the green and orange arrows, respectively. Application of EWD to this record produces the 'pure' P-wave record in (c), and the 'pure' S-wave record in (d). A constant near-surface velocity model of $V_p = 1400$ m/s and $V_s = 700$ m/s has been used to produce these EWD results.

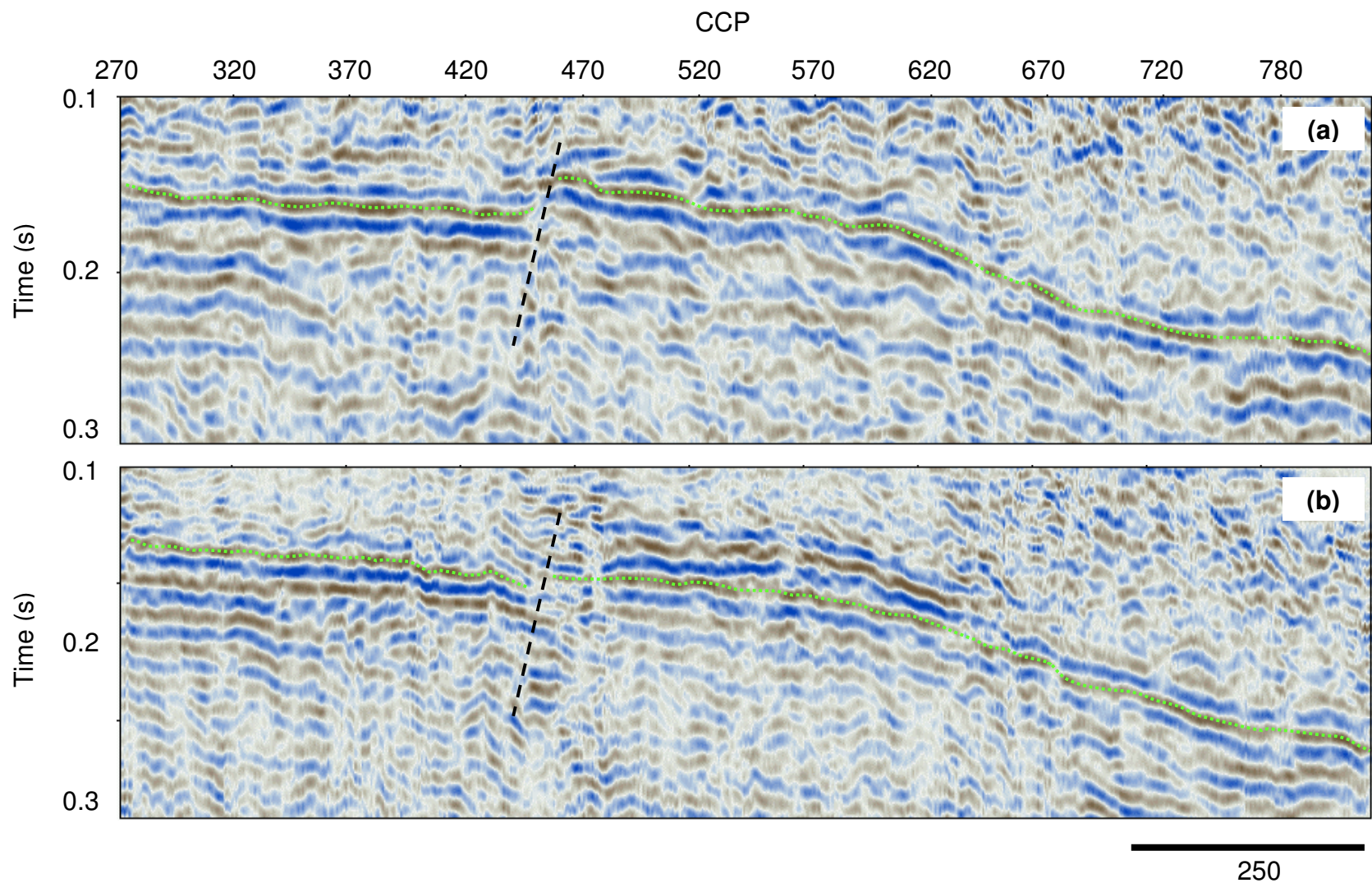


Figure 5.2 (a) Converted-wave stack produced following application of EWD to all shot records from Trial Dataset #1; and (b) conventional PS stack produced from raw inline records. The target coal reflector is indicated by the dotted green line. The interpreted fault is approximately marked by the dashed black line.

CHAPTER SIX

REAL-DATA TRIAL #2

6.1 Introduction

Trial Dataset #2 was acquired as part of ACARP Project C10020 in December, 2002. The dataset is from a location in the Bowen Basin characterised by multiple, thin coal seams. This makes it particularly relevant to our current focus on integrated P/PS seismic interpretation for determining lithological information away from boreholes. Consequently, the PS data have been re-processed using our new S-wave statics method, CCP-binning algorithm and noise-reduction filter described in Chapter 4. Details of the original survey can be found in Velseis (2003). This chapter summarises the processing and conventional P and PS interpretation results from Trial Dataset #2. The outcomes from the integrated P/PS interpretation of these data are given in Chapter 9.

6.2 Reprocessing Results

Figure 6.1 shows the final (un-migrated) P section and re-processed PS section for Trial Dataset #2. As is conventional practice, the time axes of these sections have been adjusted to provide a comparable depth perspective. The original Trial #2 PS section is given in Figure 6.2 (taken from Velseis, 2003). The two PS stacks are significantly different – this is attributed to improvements we have made in the PS processing flow (compare the current processing flow detailed in Appendix F with the original processing flow in Velseis (2003)). Specifically, pre-stack deconvolution has helped remove reverberations in the seismic data and emphasised the actual coal-seam reflection events. In addition, the new S-wave receiver statics method (Section 4.2) has yielded more robust static corrections (Figure 6.3) that do not erroneously influence the overall two-way time (TWT) structure of the PS section. The modified ‘dynamic’ CCP-binning and additional post-stack noise attenuation algorithms (Sections 4.3 and 4.4) have also helped produce a better PS section.

A notable feature of the new Trial #2 PS stack (Figure 6.1(b)) is that the interpreted PS reflection events do not consistently dip down to the right (as expected from the P-wave interpretation). Rather, the TWT horizons suffer from ‘pull-up’ from approximately CCP 620. (The precise lateral location of this ‘pull-up’ depends on whether you are examining the positive-offset or negative-offset CCP traces. That is, these data exhibit diodic illumination as described in Section 3.4.) Since this TWT ‘pull-up’ coincides with a strong reflection event appearing immediately above the shallowest interpreted horizon in Figure 6.1(b), and borehole data suggest that this additional reflection event is associated with a thick (>30m), very clean sandstone unit that extends only part way across the survey line, the change in dip of the PS reflection events is currently interpreted as signaling the presence of the sandstone unit. When upward-travelling S waves pass through this sandstone unit they speed up and reduce the overall traveltime of the corresponding PS reflection events. The same TWT variation is not observed in the P-wave reflection events. This is believed to be because the velocity of the P waves does not vary as significantly between the clean sandstone and surrounding country rock.

Note that, it is believed the original PS section (Figure 6.2) does not show the ‘pull up’ associated with the shallow sandstone unit because the original S static method actually identified the ‘pull-up’ as a static error (Figure 6.3 – see large jump in static corrections near station 330). Consequently, the true PS TWT structure was removed from the original Trial #2 PS section during application of the S-wave receiver static corrections.

It is clear from Figure 6.1 that, overall, the PS section suffers from reduced resolution compared to the P section. This is confirmed by the representative stacked-trace spectra in Figure 6.4. The dominant frequency of the stacked PS data is approximately 40 Hz. The dominant frequency of the stacked P data is approximately 130 Hz. Since the geophones used to acquire these data are designed to suppress energy with frequencies less than 40 Hz, the PS reflection events have a very narrow bandwidth. As demonstrated in Section 2.2, this results in a broad and ‘ringy’ PS seismic pulse. This is consistent with what we observe in Figure 6.1(b).

Despite the lower frequency content of the Trial #2 PS stack, two faults have been interpreted. The Rayleigh resolution limits for the P and PS sections in Figure 6.1 are 4.5 m and 8.5 m, respectively (Appendix H). Thus we don’t expect to see faults with throws much less than these limits on the P and PS seismic sections. However, computation of these resolution limits makes assumptions about the local P and S seismic velocities. We do not have a great deal of experience with estimating S velocities. It may be that S velocities drop considerably about faults that exist within large zones of significant fracturing. This would create zones of higher-than-average PS resolution and could explain the ability of PS data to ‘see’ faults that aren’t interpreted in the corresponding P section, despite having a larger general Rayleigh resolution limit. Drilling or underground mapping information is required to validate the interpreted faults and test this hypothesis.

It is interesting to note that, albeit the PS section suffers from gross TWT-structure errors due to improper static corrections, the dominant frequency of the original PS section (Figure 6.2) is also approximately 40 Hz (Velseis, 2003). This seems to suggest that, contrary to our current understanding, accurate S-wave receiver statics may not be the most critical factor controlling the resolution of our PS sections. Recent investigations into PS-wave behaviour have highlighted the sensitivity of S waves to inhomogeneities (including anisotropy) in the sub-surface (Chapter 3). In the coal environment sedimentary layering would create strong anisotropic behaviour in the sub-surface. We are currently not accommodating anisotropy in our PS processing flow. Thus, the significant loss of high-frequency information in the PS stack may be a result of sub-optimal CCP-binning and NMO algorithms that ignore the effect of anisotropy. This will be a topic for future investigation.

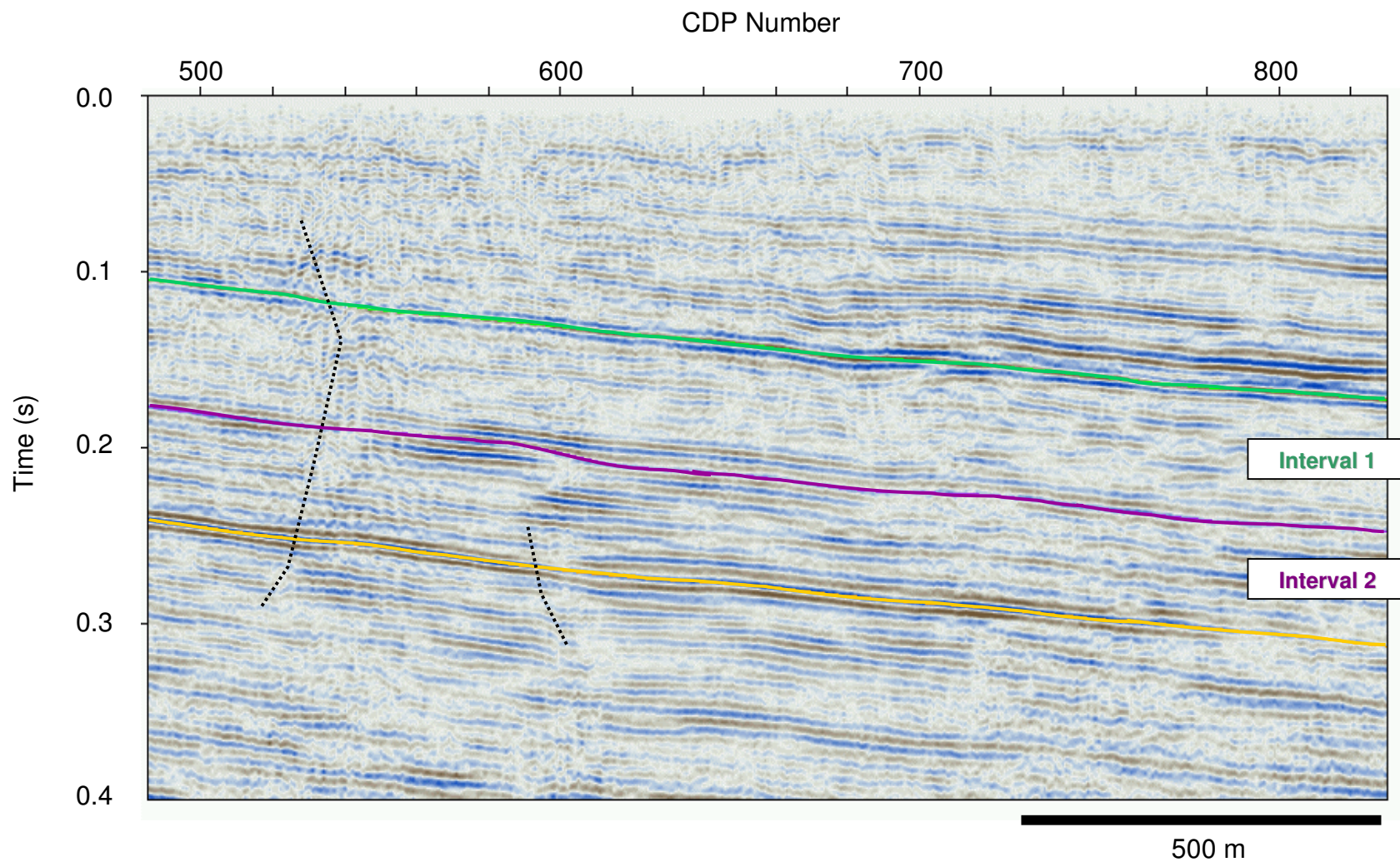


Figure 6.1 (a) P-wave seismic image for Trial #2 derived from the vertical component of the multi-component data. Interpreted seismic horizons for three identified coal seams are marked on the section. Note that, these seismic horizons have been smoothed using a 30-point smoothing window for subsequent integrated P/PS interpretation (Section 9.2). Two intervals for V_p/V_s analysis are defined (Section 9.3). Interpreted faults are approximately marked.

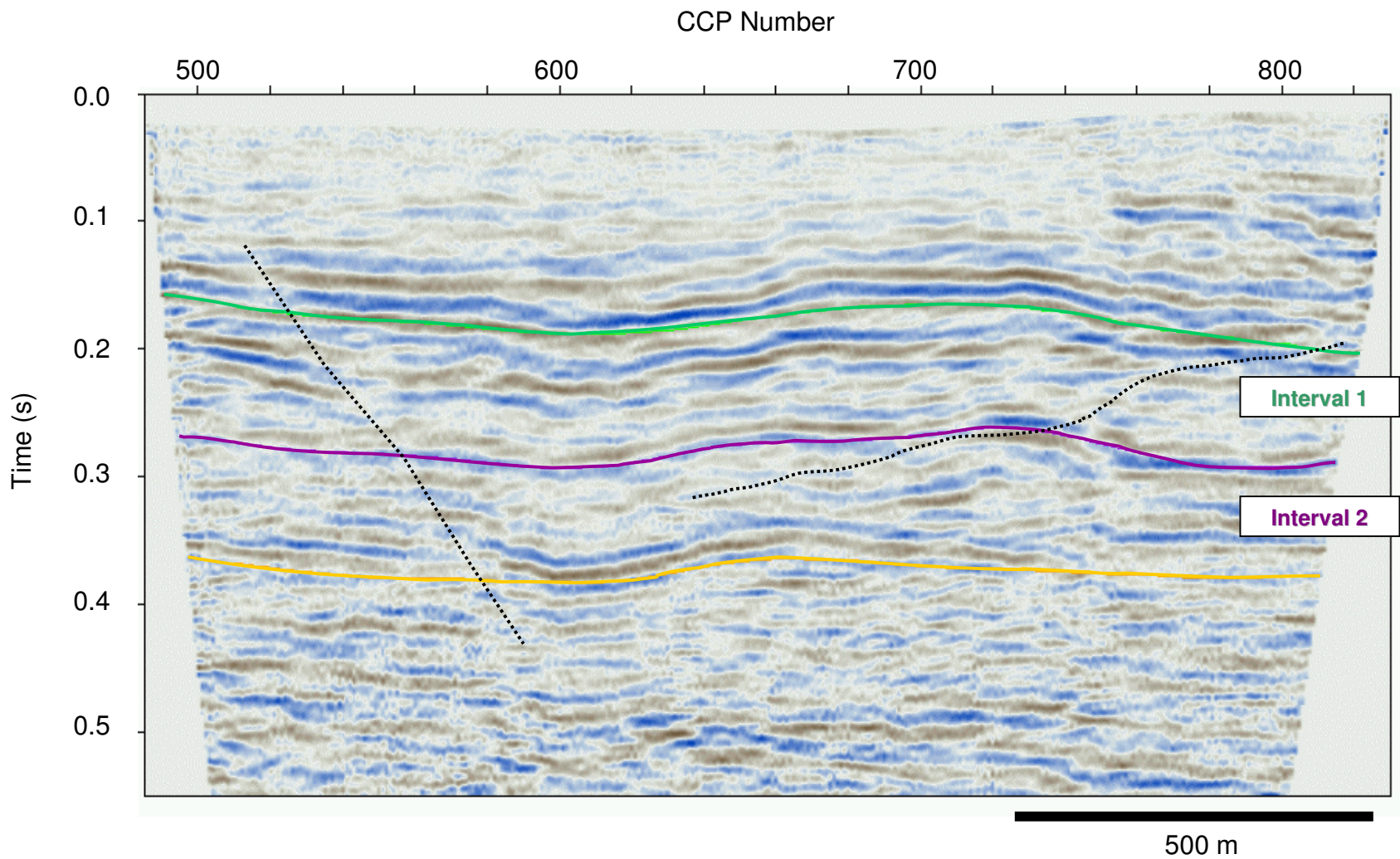


Figure 6.1 (b) Reprocessed PS-wave seismic image for Trial #2 derived from the inline component of the multi-component data. Interpreted seismic horizons for three identified coal seams are marked on the section. Note that, these seismic horizons have been smoothed using a 50-point smoothing window for subsequent integrated P/PS interpretation (Section 9.2). Two intervals for V_p/V_s analysis are defined (Section 9.3). Interpreted faults are approximately marked.

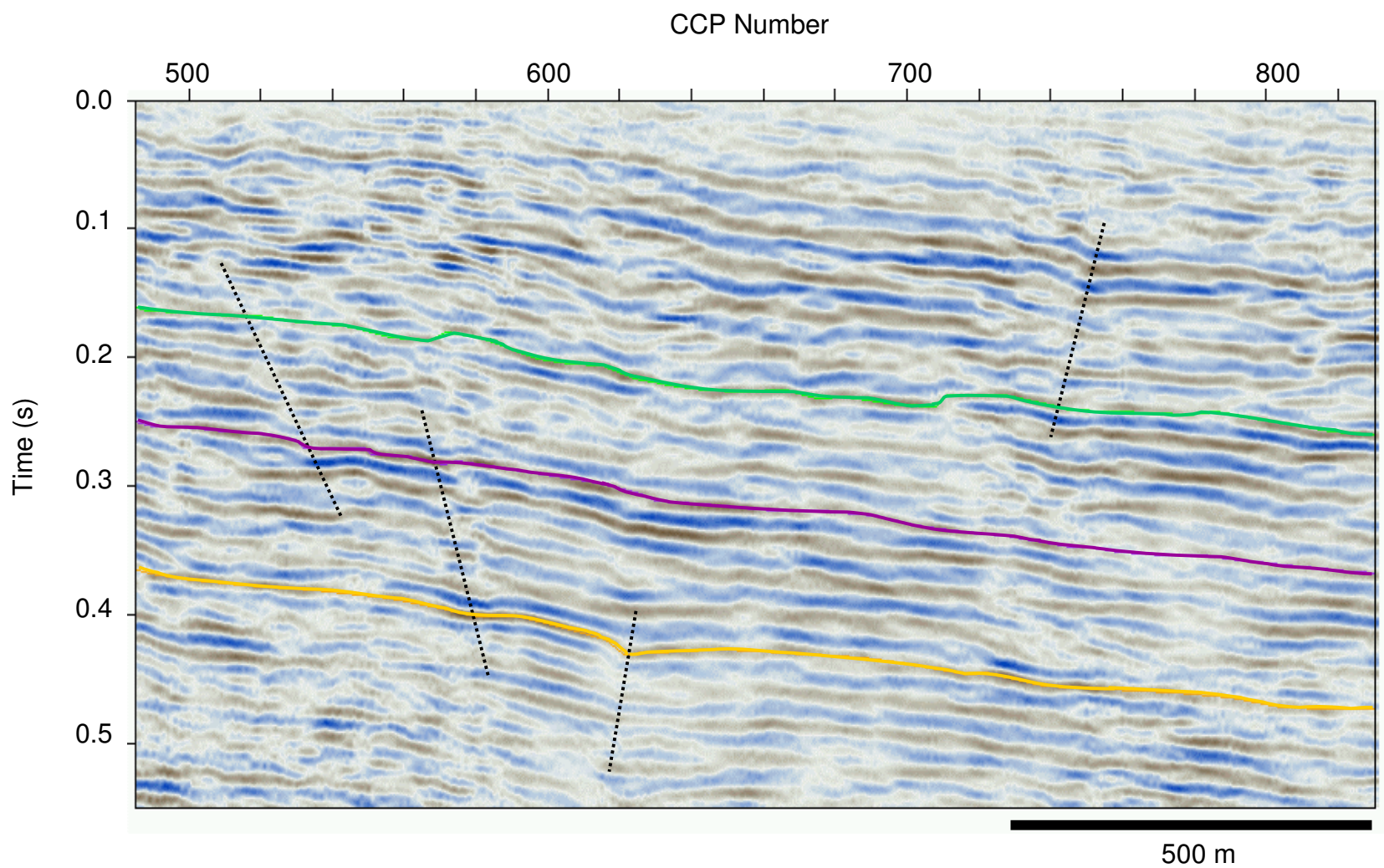


Figure 6.2 Original PS-wave seismic image for Trial #2 derived from the inline component of the multi-component data (Velseis, 2003). Interpreted seismic horizons for three identified coal seams are marked on the section. Interpreted faults are approximately marked.

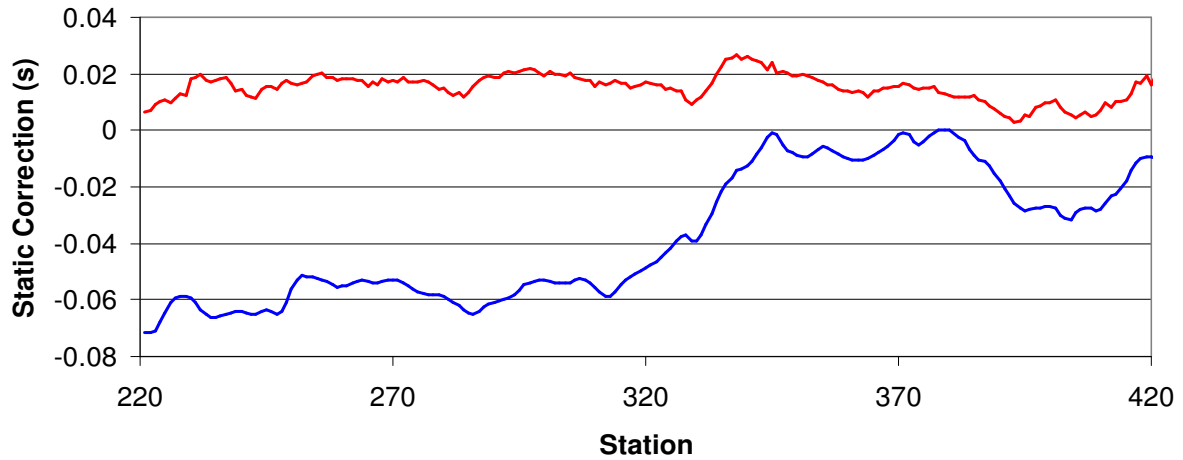


Figure 6.3 Comparison of original S-wave receiver static corrections (blue) derived from old statics method and new S-wave receiver static corrections (red) derived using method described in Section 4.2. The original static corrections have incorrectly incorporated large TWT variations associated with below-weathering lithological variations along the line. The resultant PS section (Figure 6.2) is believed to have gross TWT-structure errors along the right side of the image.

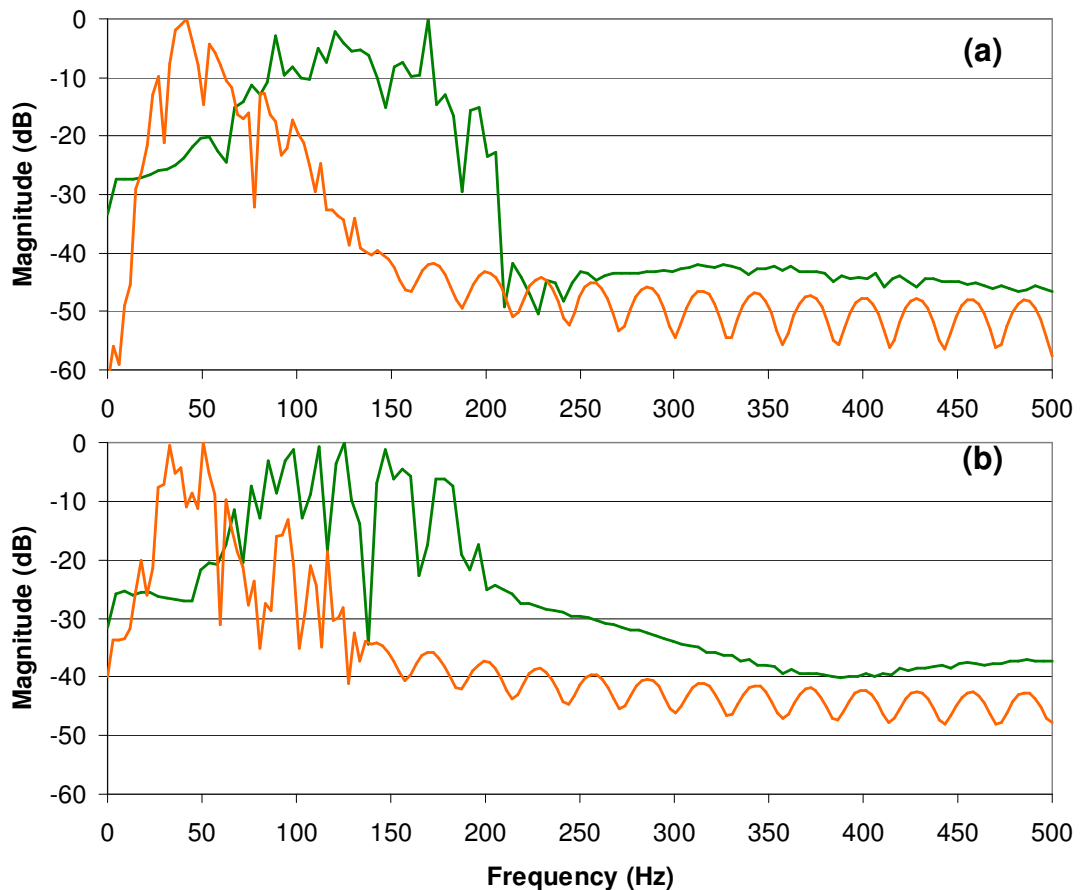


Figure 6.4 Comparison of stacked-trace spectra from the final P and PS sections shown in Figure 6.1 – (a) CDP/CCP 510; and (b) CDP/CCP 700. Frequency spectra for the P-wave data are shown in green. Frequency spectra for the corresponding PS data are shown in orange.

CHAPTER SEVEN

REAL-DATA TRIAL #3

7.1 Introduction

Given the focus of this project to relate integrated P/PS seismic attributes to lithology, an additional multi-component dataset was acquired at a Bowen Basin site specifically useful for illustrating lithological issues. As for Trial #2, the data are from a location characterised by multiple coal seams, and the interburden geology is known to exhibit lateral heterogeneity. This chapter summarises the acquisition, processing and conventional P and PS interpretation of the data from the third trial site. These data are re-visited in Chapter 9 to demonstrate integrated P/PS interpretation for improved geological characterisation of the sub-surface.

7.2 Data Acquisition

Acquisition of Trial Dataset #3 was undertaken by Velseis Pty Ltd on Wednesday 8th June and Thursday 9th June, 2005 (Figure 7.1). The 1.5km trial line was located within a pre-existing 3D seismic grid. The site was selected by mine staff to satisfy the following conditions:

- presence of multiple coal seams (with at least three of thickness 2 m or more, at depths greater than 80 m)
- boreholes (with geophysical logs) available along line
- line to extend across zone where interburden geology is predicted to vary significantly

The seismic recording parameters are given in Table 7.1.

Table 7.1: Field acquisition parameters for Trial #3.

Recording System	Velcom 348
Line Length	1.5 km
Source	Dynamite 400 g Booster / 25 m Electric Dets
Source Depth	12-40 m
First / Last Shotpoint	100.5 / 300.5
Shotpoint Interval	15 m
Geophone	GS30CT-3-series 10Hz / 395 ohm
Receiver Array	3 3C geophones over 1 m
Receiver Interval	7.5 m
Spread	120 channels x3 split spread
Near Trace	3.75 m
Far Trace	446.25 m
Nominal Fold	30
Data Format	SEGY
Sample Interval	1 ms
Record Length	1 s
Recording Filters	Low Cut: -3 dB @ 16 Hz High Cut: -3 dB @ 320 Hz



Figure 7.1 Field acquisition of Trial Dataset #3: planting 3C geophones (left); and a 3C receiver station (above).

Figure 7.2 shows the surface elevation along the trial line. Topographic variation is minimal, apart from a small gully near station 157. The survey line was cleared of grass, leaving a surface cover of bulldust and unconsolidated sandy material. Note that, a strong breeze affected recording from approximately shot 200.5. Light rain fell on receiver stations 260 – 300 during acquisition.

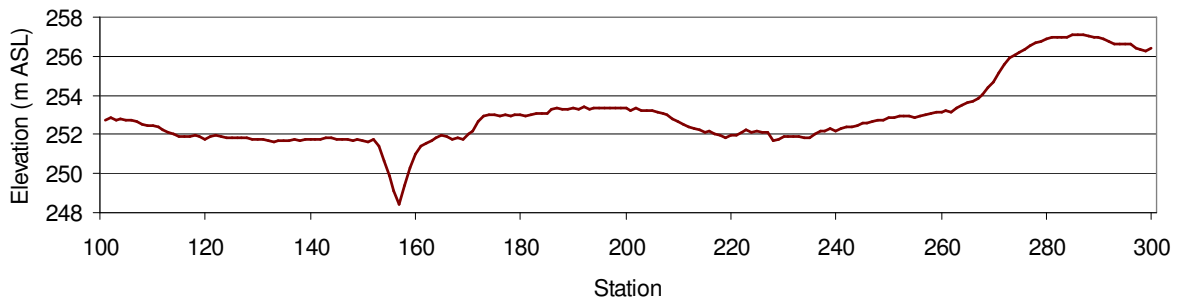


Figure 7.2 Surface elevation along survey line for Trial #3.

Representative vertical and inline shot records from Trial Dataset #3 are shown in Figure 7.3. It is apparent that strong P-to-S conversion is occurring at multiple horizons in the geological sequence, with several dominant converted-wave reflections present in the inline record. Note that both the P and PS reflection events on the raw records suffer from trace-to-trace travelt ime ‘jitter’ associated with weathering statics. As expected, the raw PS reflection events suffer from poorer coherency than the corresponding P-wave reflection events since S-wave weathering statics are typically much more severe than P-wave statics. Note also that, overall, the inline record is noisier than the corresponding vertical record. This is typical of all of our 3C datasets. Consequently, our PS sections tend to suffer from poorer signal-to-noise ratio than our conventional P-wave images

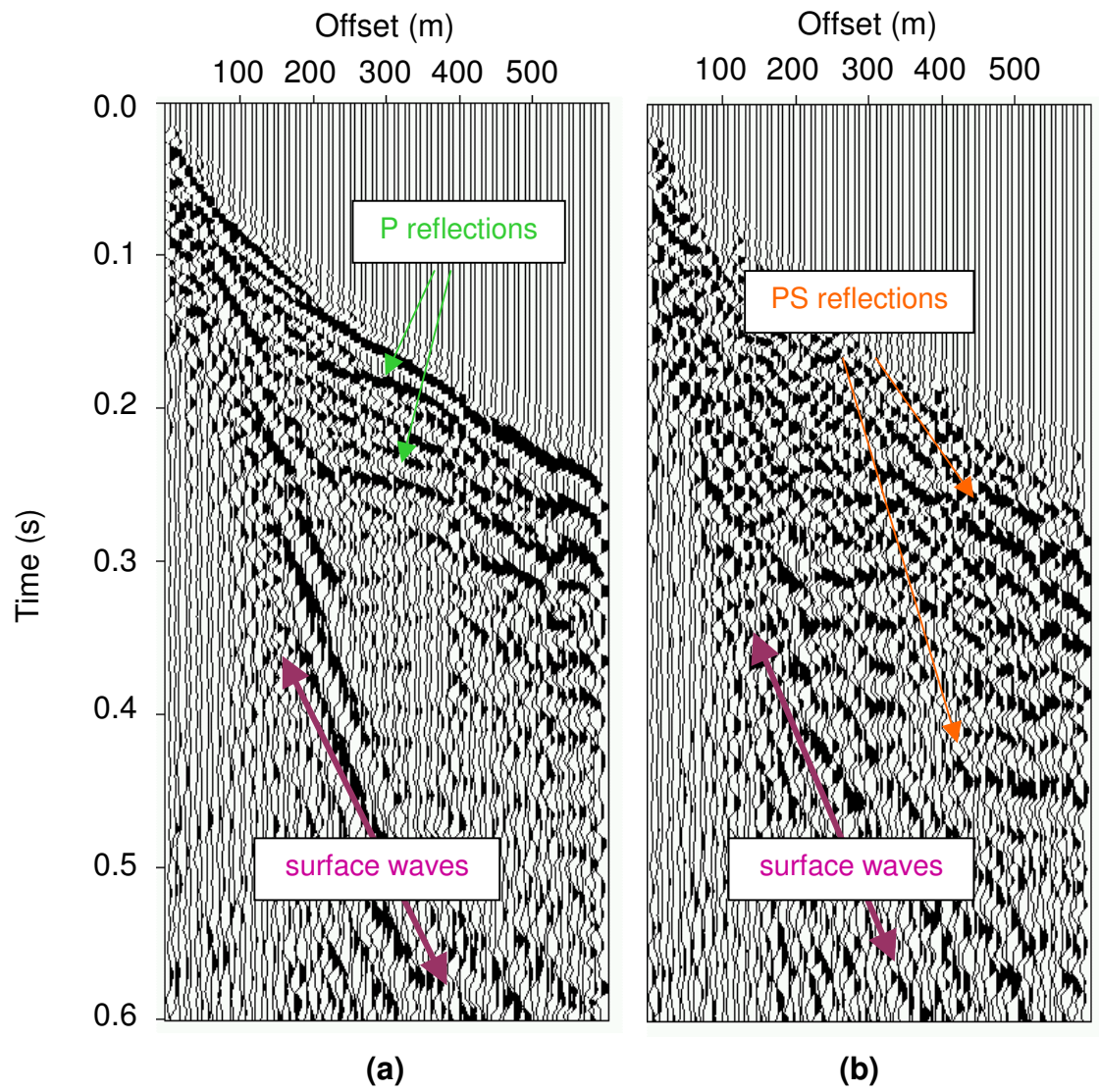


Figure 7.3 (a) Vertical component and (b) inline component of a representative shot record from Trial Dataset #3. P and PS reflection events are indicated.

The raw PS data exhibit a slightly reduced frequency content compared to the raw P data. Figure 7.4 shows frequency spectra for a number of traces from the shot records illustrated in Figure 7.3. The average dominant frequency of the raw P signal is approximately 75 Hz, with the signal bandwidth extending from 30 – 120 Hz. The average dominant frequency of the raw PS signal is approximately 55 Hz, with the signal bandwidth extending from 15 – 100 Hz. As discussed in Section 2.3, acquisition of these data using geophones with a natural frequency of 10 Hz has enabled significant PS energy below 40 Hz to be recorded. Note that, it is likely the overall lower frequency content of the PS data is a result of attenuation of the upward-travelling S energy in a thick near-surface sequence of interbedded high-ash coals, carbonaceous shales and mudstones. This behaviour was also observed for Trial #2 (Velseis, 2003). In the case of Trial #3, the attenuating sequence is up to 60 m thick, and ranges in depth from 0 m (surface) down to 60 m. Note however, that this slight reduction in dominant frequency for the raw PS data does not automatically mean that the resultant PS section will exhibit poorer vertical resolution than the P section. PS energy can have a lower dominant frequency and still yield a section with greater or comparable vertical resolution since the wavelengths of S waves are shorter than for P waves. This is discussed further in Appendix H.

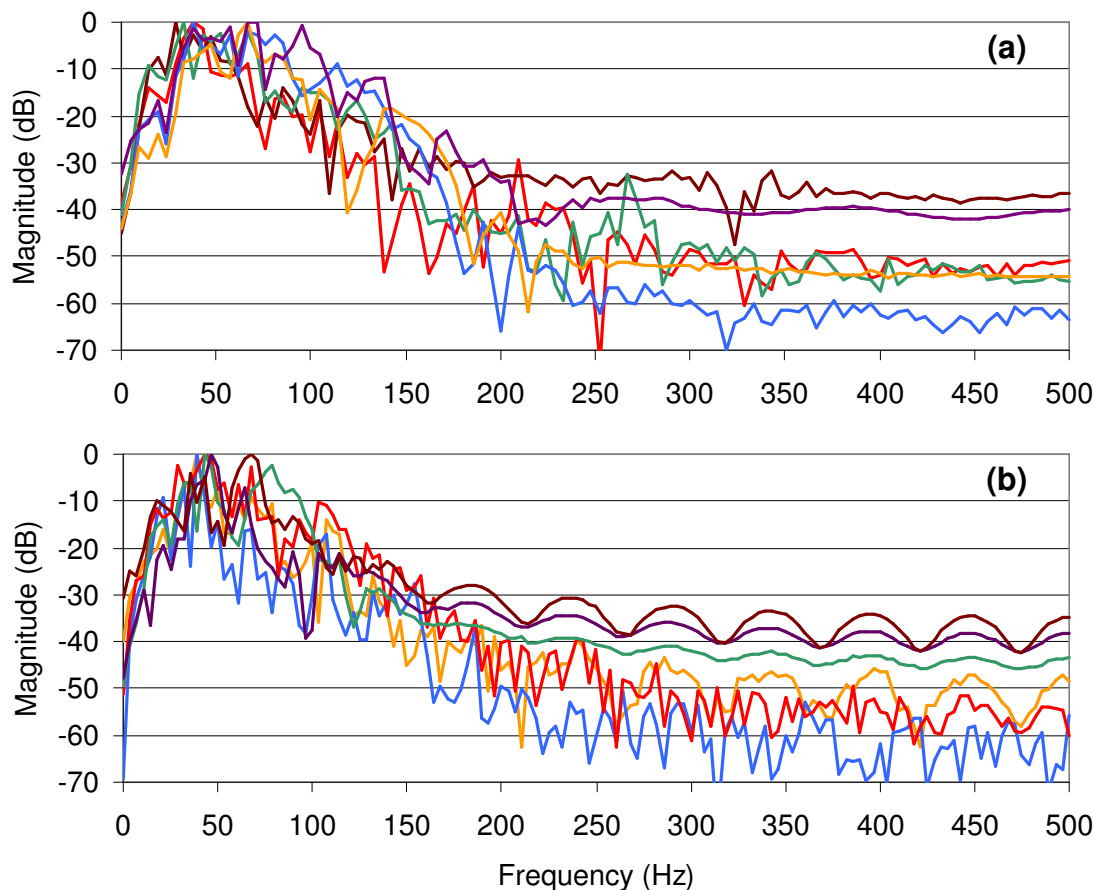


Figure 7.4 Representative trace spectra from the (a) vertical-component and (b) inline-component records given in Figure 7.3. These magnitude spectra have been computed over short time windows centred about the target reflection events.

7.3 Trial Results

Details of both the conventional and converted-wave processing sequences used to produce the final P- and PS-wave images presented here are given in Appendix G. Note that, processing of the PS data from Trial #3 has utilised our latest PS processing flow (Figure 4.7) (i.e. PS processing has included use of the new S-wave statics algorithm, CCP-binning code and eigenvector filter described in Chapter 4).

Figure 7.5 shows the final (un-migrated) P and PS sections for Trial Dataset #3. The vertical scale of the PS image has been adjusted (based on an estimated P-wave to S-wave velocity ratio) to provide a comparable depth perspective to the P-wave image. Despite the raw seismic data indicating that the PS section could have comparable or better resolution than the P section (Section 7.2; Appendix H), it is immediately obvious that the PS section shows significantly reduced resolution compared to the P section, and does not contribute structural information along the survey line. This loss of resolution in the PS section is confirmed by the representative stacked-trace spectra in Figure 7.6. The dominant frequency of the stacked PS data is only about 30% of the dominant frequency of the stacked P data. [The dominant frequency of the pre-stack PS data is approximately 70% of the dominant frequency of the pre-stack P data.]

A similar loss of high-frequency information during PS processing has been observed for Trial #2. As noted in Section 6.2, one possible explanation for this behaviour is our current approach of ignoring anisotropic effects in our CCP-binning and normal moveout (NMO) algorithms. The results from both Trial #2 and Trial #3 suggest that, until the loss of high-frequency information during the PS stacking process is better understood and can be compensated for, acquisition of PS data in areas with deep target reflectors beneath shallow, thick interbedded coal/sedimentary sequences (which will be strongly anisotropic) is not suitable if structural information is the primary motivating factor for collecting the PS data. [Note that, our mini-SOSIE 3C seismic surveys are successfully yielding PS sections that are competitive for structural imaging where target reflectors are less than approximately 150 m deep and do not have overlying thick interbedded sequences.]

Despite the Trial #3 PS section not being able to contribute structural information along the line, the PS data are still capable of providing other information about the sub-surface that cannot be obtained using P-wave data alone. For example, along the right-hand end of the Trial #3 PS section (Figure 7.5(b)), the lower four coal reflection events are being 'pulled-up' relative to the P reflection events. This TWT 'pull-up' is observed on the positive-offset traces (used to produce the final PS stack along this portion of the line) but not the negative offset traces. Recognition of this diodic behaviour (Section 3.4) helps signal that a lithological anomaly exists in the sub-surface. In this case, it is believed that a thick, very clean sandstone unit exists above these four coal seams to cause this effect (this is consistent with nearby borehole data). Additional lithological information recovered via integrated P/PS interpretation of these data is presented in Chapter 9.

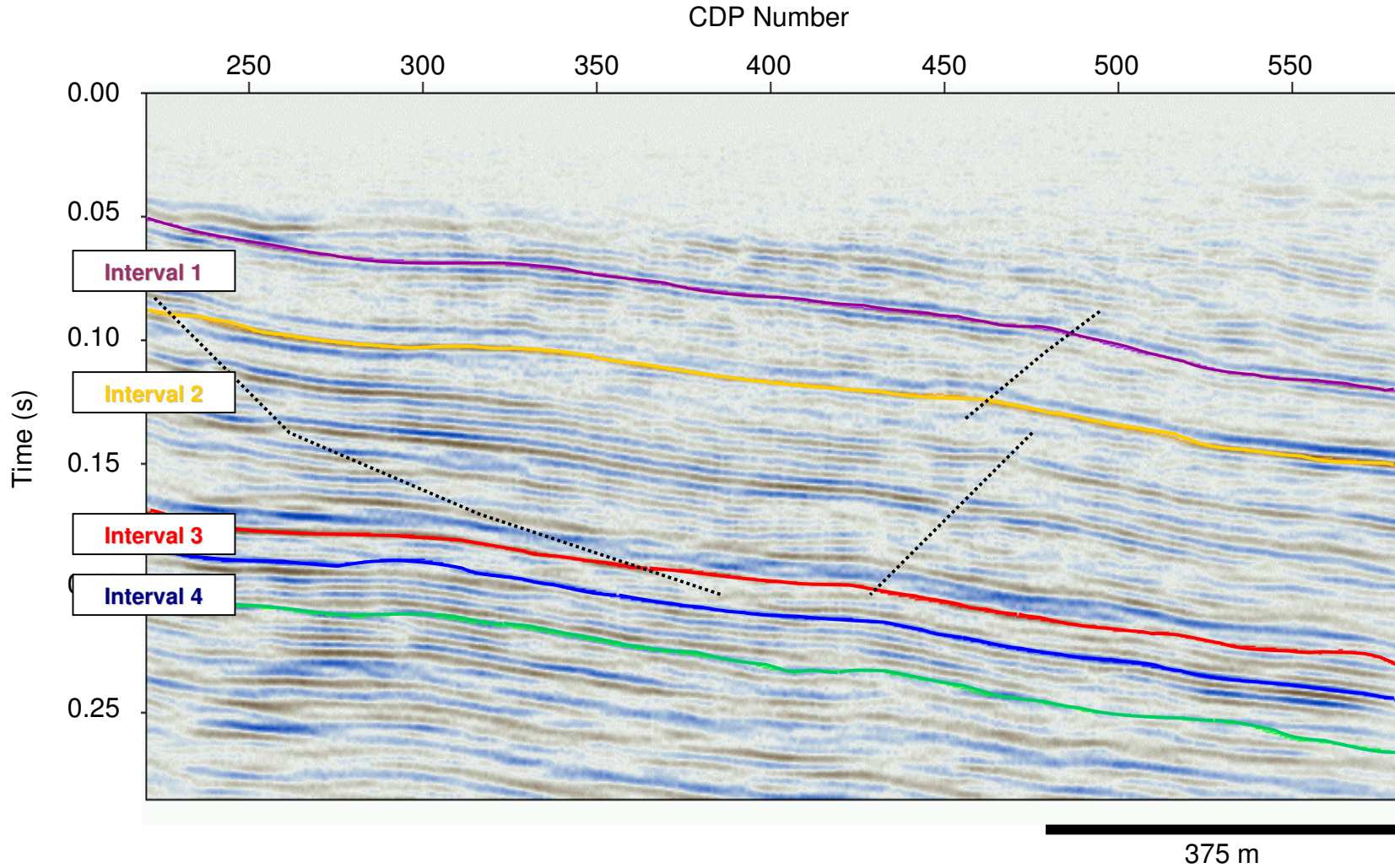


Figure 7.5 (a) P-wave seismic image for Trial #3 derived from the vertical component of the multi-component data. Five seismic horizons interpreted to be coal-seam reflection events are marked on the section. Note that, these seismic horizons have been smoothed using a 30-point smoothing window for subsequent integrated P/PS interpretation (Section 9.2). Four intervals for V_p/V_s analysis are defined (Section 9.4). Interpreted faults are approximately marked.

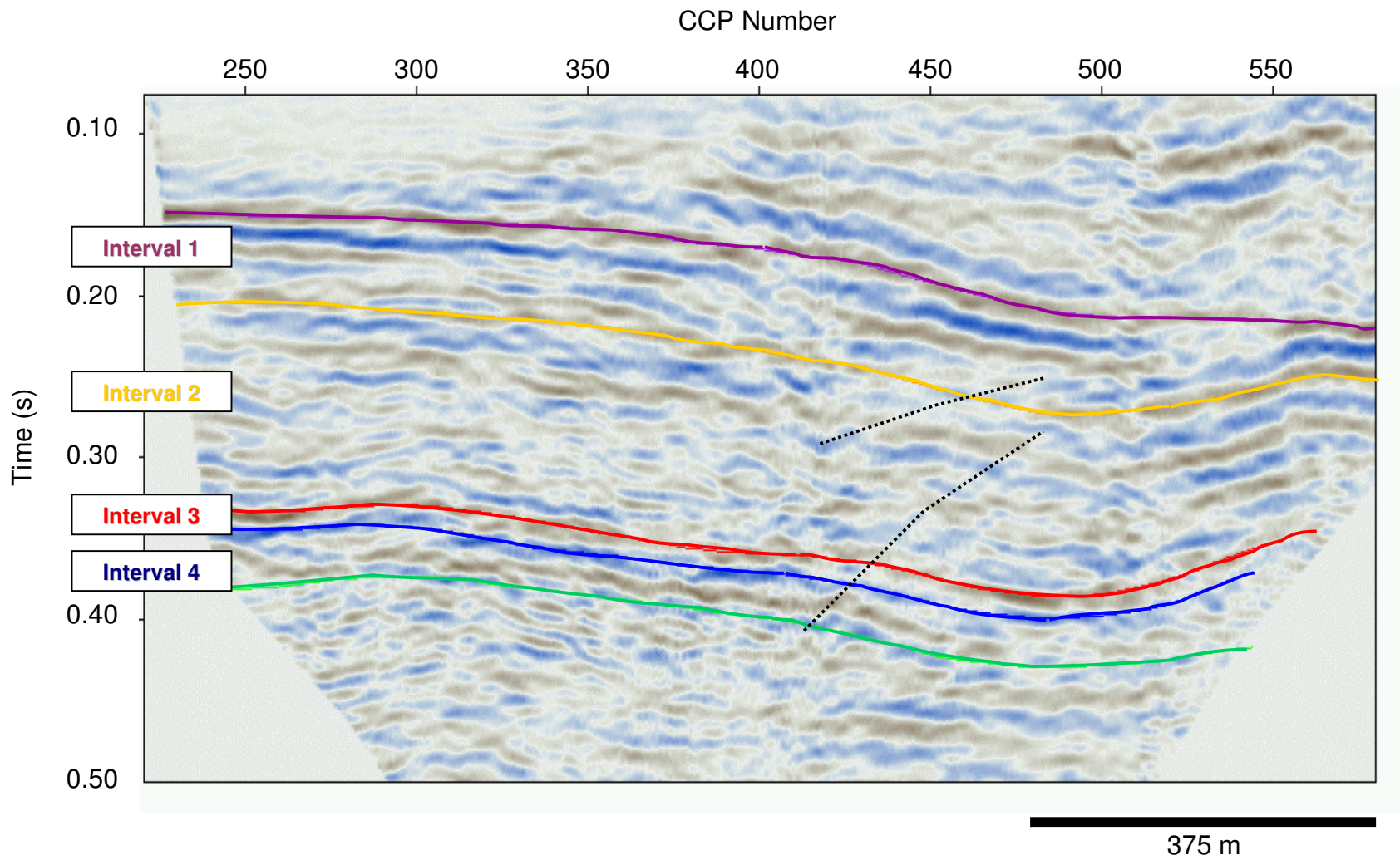


Figure 7.5 (b) PS-wave seismic image for Trial #3 derived from the inline component of the multi-component data. Five seismic horizons interpreted to be coal-seam reflection events are marked on the section. Note that, these seismic horizons have been smoothed using a 50-point smoothing window for subsequent integrated P/PS interpretation (Section 9.2). Four intervals for V_p/V_s analysis are defined (Section 9.4). Interpreted faults are approximately marked.

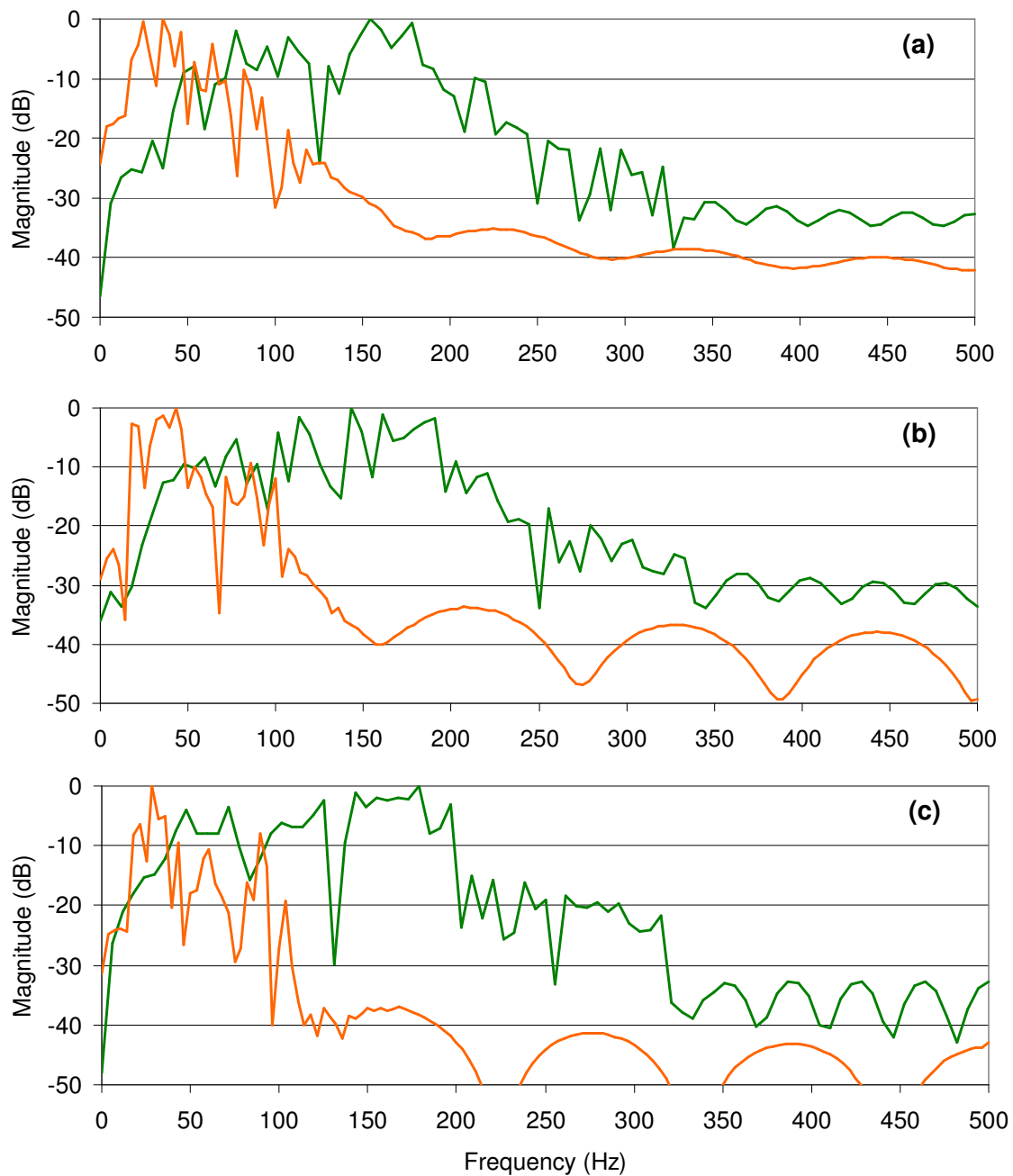


Figure 7.6 Comparison of stacked-trace spectra from the final P and PS sections shown in Figure 7.5 – (a) CDP/CCP 300; (b) CDP/CCP 400; and (c) CDP/CCP 500. Frequency spectra for the P-wave data are shown in green. Frequency spectra for the corresponding PS data are shown in orange.

CHAPTER EIGHT

Vp/Vs INTERPRETATION: THEORY AND SYNTHETIC DATA ANALYSIS

8.1 Introduction

One of the primary objectives of this project has been to investigate the potential for the P-wave to S-wave velocity ratio (V_p/V_s) to yield detailed information about sub-surface geology away from borehole locations. The motivation behind V_p/V_s analysis is that the velocity ratio is an effective indicator of lithology and/or fractures, cracks and pore space (Tatham, 1982). Table 3.1 lists typical V_p/V_s values for a number of different rock types. Poorly consolidated or fractured material will also exhibit high V_p/V_s values. V_p/V_s analysis can yield estimates of Poisson's Ratio. This elastic constant is an indicator of rock strength, and may be useful for predicting behaviour of the roof and/or floor in underground mining situations. This chapter reviews the basic methodology of V_p/V_s interpretation, and presents results from a number of synthetic trials designed to examine the accuracy and resolution of geological information recoverable via V_p/V_s analysis. Real-data V_p/V_s interpretation results for Trials #2 and #3 are presented in Chapter 9.

8.2 Methodology

The V_p/V_s attribute for a specific geological interval can be estimated via:

$$V_p/V_s = \left(2 \frac{\Delta t_{PS}}{\Delta t_P} \right) - 1, \quad (8.1)$$

where Δt_P and Δt_{PS} are the time differences between the seismic reflection events at the top and bottom of the interval of interest on the P and PS sections, respectively.

It is obvious from equation 8.1 that, in order to undertake V_p/V_s interpretation, more than one reflection event must be interpretable on both the P and PS seismic sections. (Thus, data from Trial #1 are not used in our V_p/V_s interpretation experiments.)

Computation of this seismic attribute also assumes that reflection events correlated between the P and PS sections originate at the same geological boundary. Accurate correlation of reflection events on the P and PS seismic sections is the most critical and most difficult step in the V_p/V_s analysis process.

Poisson's Ratio can be derived from the resultant V_p/V_s estimate via (Sheriff, 1991):

$$\sigma = \frac{\left(\frac{V_p}{V_s} \right)^2 - 2}{2 \left(\frac{V_p}{V_s} \right)^2 - 2}. \quad (8.2)$$

As seen from equation 8.2, no new information is introduced by using Poisson's Ratio instead of V_p/V_s . However, mine staff are possibly more familiar with this elastic constant. Hence, Poisson's Ratio is included on all V_p/V_s interpretation results presented in this report.

8.3 Recovering Absolute V_p/V_s Values

From equation 8.1, it is apparent that recovery of the absolute V_p/V_s value for a geological interval requires accurate two-way time (TWT) picks along the top and bottom P and PS seismic reflection events for that interval. It follows that V_p/V_s analysis will only recover correct absolute V_p/V_s values when a geological interval has a thickness greater than the seismic wavelength. When the top and bottom boundaries of a geological interval are less than a wavelength apart, the seismic reflection events from these boundaries begin to interfere with one another. The resultant TWT picks extracted from the seismic section will be affected by this interference, and Δt_P and Δt_{PS} values will not reflect the true thickness of the interval. Corresponding V_p/V_s values will be incorrect.

This impact of interval thickness on absolute V_p/V_s values is illustrated in Figures 8.1 to 8.4. For this simple coal-wedge model, V_p/V_s analysis correctly computes an absolute V_p/V_s value of approximately 2.5 for seam thicknesses ranging from 40 m down to approximately 15 m. The point at which V_p/V_s analysis fails to accurately predict the true coal V_p/V_s is the point at which the reflection events from the top and bottom of the coal seam begin to significantly interfere with one another. This occurs when the coal-seam thickness drops below the seismic wavelength (here, 17 m).

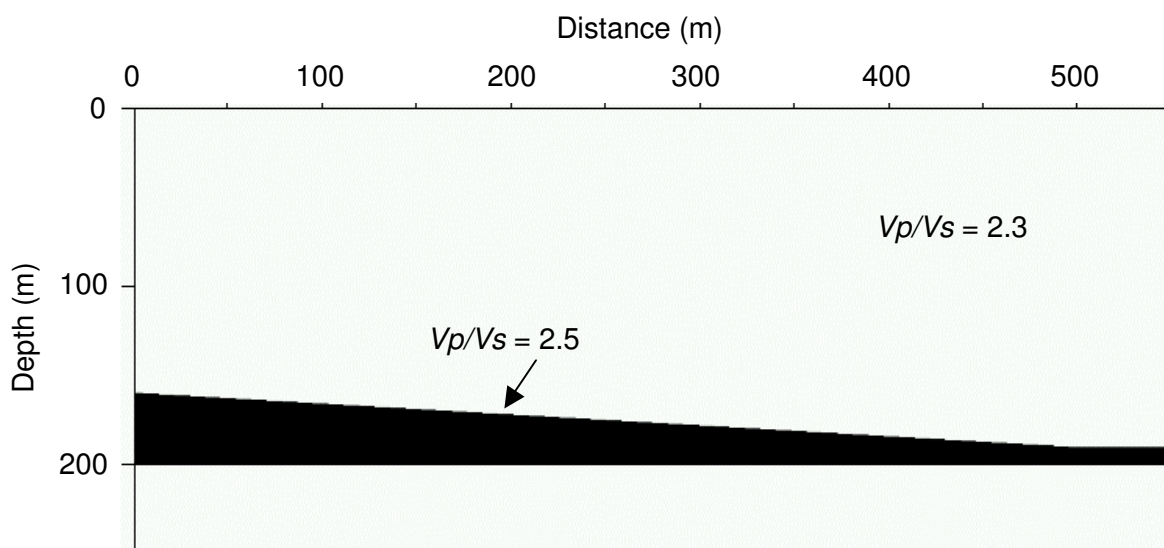


Figure 8.1 Synthetic earth model used to generate the P and PS seismic sections shown in Figure 8.2. The coal wedge starts with a thickness of 40 m and thins to 10 m. The coal V_p/V_s is 2.5 ($V_p = 2200$ m/s; $V_s = 880$ m/s). The coal sits in a shale-rich country rock with a V_p/V_s of 2.3 ($V_p = 3350$ m/s; $V_s = 1450$ m/s).

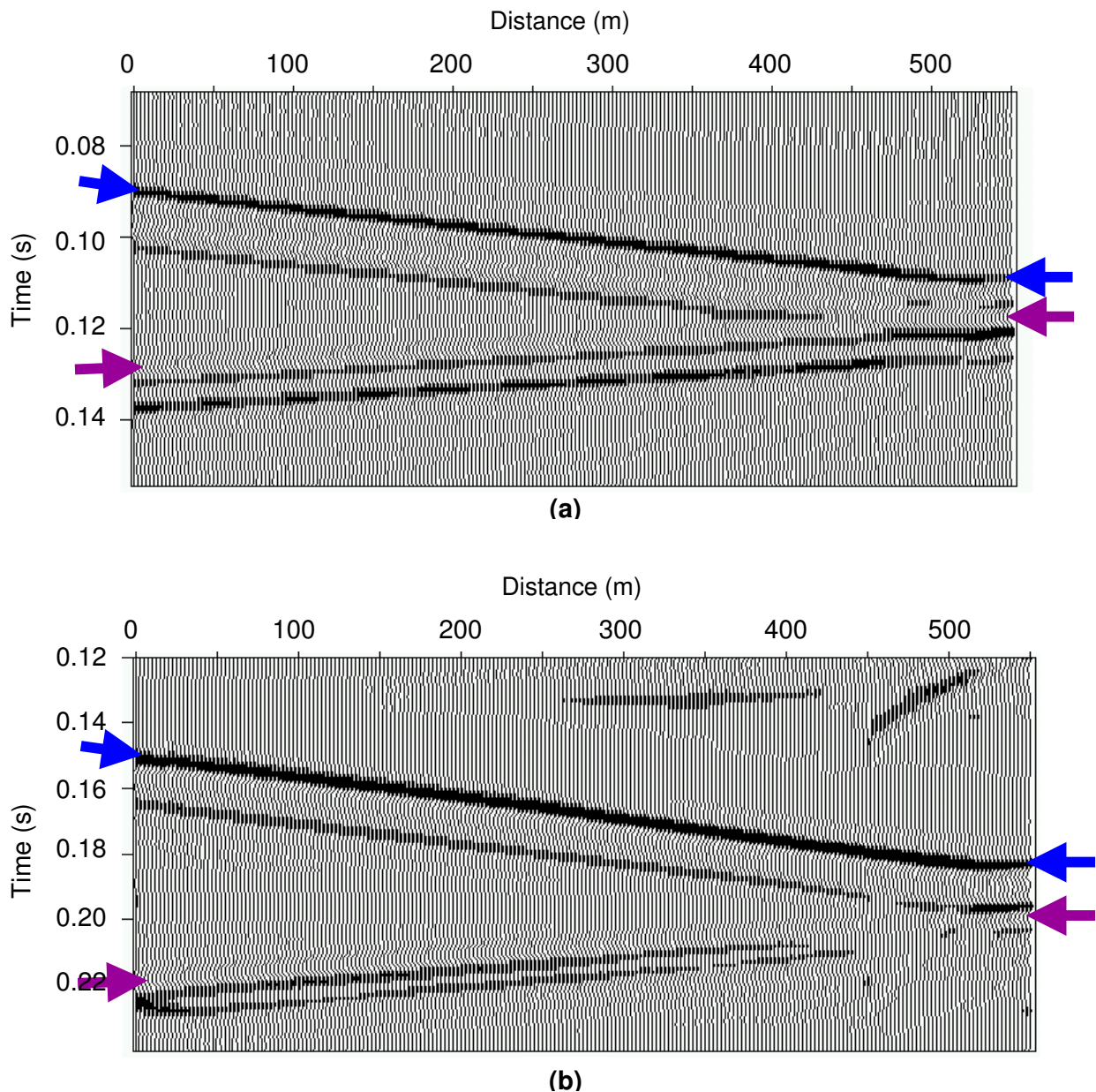


Figure 8.2 (a) P-wave and (b) PS-wave seismic sections corresponding to the earth model shown in Figure 8.1. See Appendix I for details on the synthetic seismic modelling used to generate these data. The reflection events for the upper and lower boundaries of the coal wedge are indicated by the arrows. Note that the time axes of these sections have been adjusted appropriately to provide a comparable depth perspective.

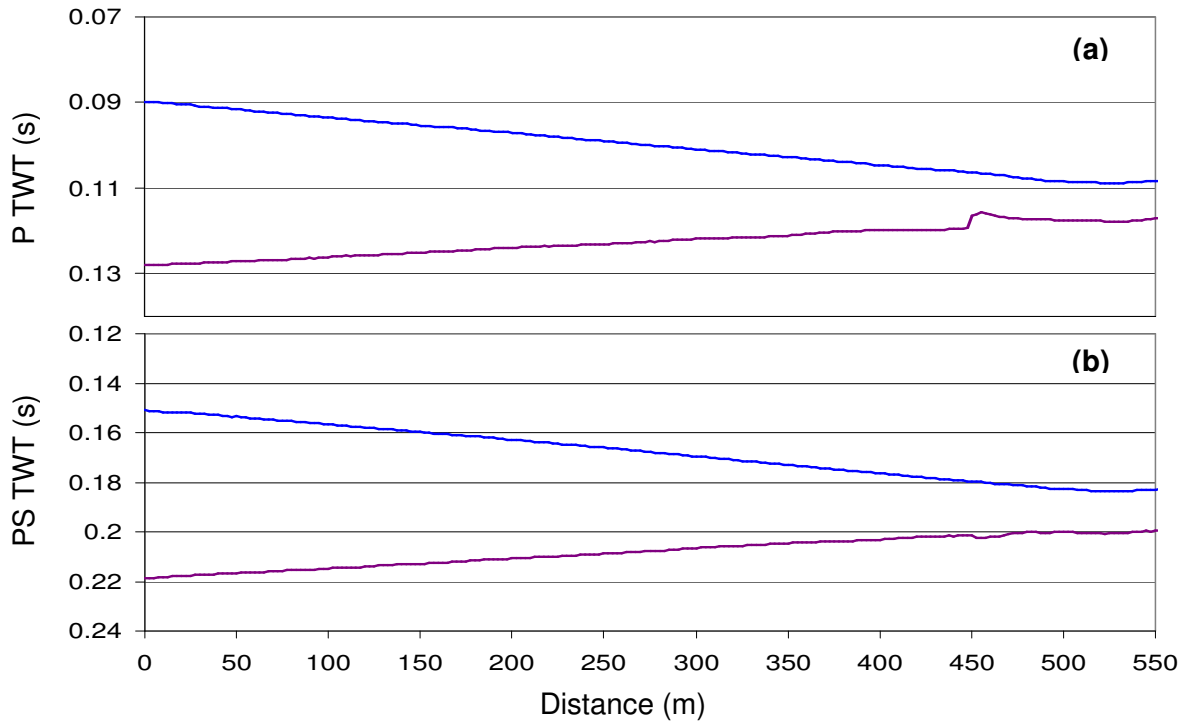


Figure 8.3 Two-way time (TWT) picks along the top and bottom coal-wedge reflection events for (a) the P-wave and (b) the PS-wave sections given in Figure 8.2.

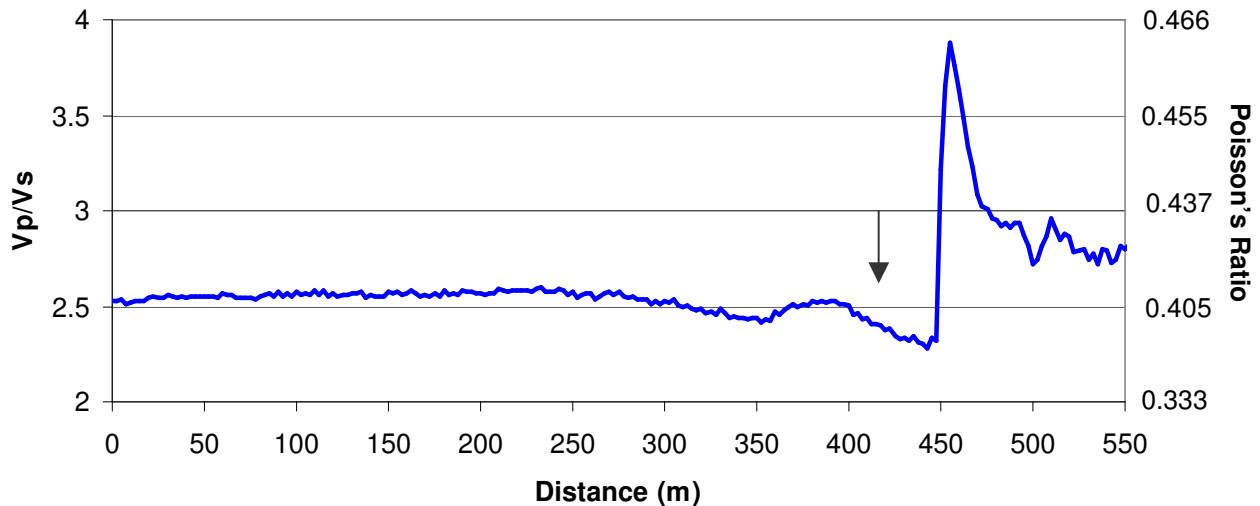


Figure 8.4 V_p/V_s measurements computed for the coal-wedge model using the TWT information displayed in Figure 8.3. For coal thickness ranging from 40 m down to approximately 15 m (marked by arrow), V_p/V_s analysis correctly computes an absolute V_p/V_s of approximately 2.5. When the coal thickness drops below the seismic wavelength, the V_p/V_s estimates become unstable, dropping low before becoming spuriously high. Equivalent Poisson's Ratio values are indicated on the right-hand axis.

In reality, the thicknesses of our coal seams will always be much less than the seismic wavelengths we typically find in a coal environment (wavelengths can vary between approximately 12 – 40 m). Consequently, top- and base-coal reflection events are generally indistinguishable, forming one combined top/base coal seismic-reflection package. As a result, we don't believe Vp/Vs analysis can be meaningfully applied to the coal seams themselves. Instead, Vp/Vs analysis in the coal environment should be aimed at the detection of lithological variations between coal seams (e.g. to indicate roof and/or floor conditions; to locate sand channels etc). Note however, in conducting Vp/Vs analysis on these inter-seam intervals, we typically use the combined top/base coal seismic-reflection packages to define the seismic intervals. Since these top/base coal seismic-reflection packages are affected by seismic wave interference, it transpires that absolute Vp/Vs value can't be recovered even if the interval of interest is thicker than the seismic wavelength. This scenario is illustrated in Figure 8.5. The seismic datasets used to generate the Vp/Vs values in Figure 8.5 have a wavelength of approximately 30 m. Based on the coal-wedge synthetic example discussed above, we would then expect the 40 m interval to yield accurate absolute Vp/Vs values. However, the absolute Vp/Vs values computed for the 40 m-, 15 m- and 9 m-thick geological intervals are all incorrect because the top and bottom reflection events used to define each of the intervals are, themselves, affected by seismic interference.

Figure 8.5 effectively demonstrates that the recovery of absolute Vp/Vs values in the coal environment is extremely unlikely. Equivalently, it is unlikely we can determine absolute values for Poisson's Ratio. However, Figure 8.5 does illustrate that it is still possible to get an accurate indication of relative Vp/Vs behaviour. In Figure 8.5, each Vp/Vs curve clearly reveals a zone of low Vp/Vs that can be interpreted as a zone of sand-rich material. This suggests that Vp/Vs analysis is a useful tool for highlighting zones within a geological interval that are, say, relatively sand- or shale-rich, compared to the surrounding geology. Note however, when using Vp/Vs analysis to detect relative changes in geology, the Vp/Vs values computed for one geological interval cannot be directly compared to those generated for another interval. As illustrated in Figure 8.5, the Vp/Vs values derived for rock types with the same physical velocity-ratio are unlikely to be the same for intervals of different thicknesses. Thus, derived Vp/Vs values are only suitable for qualifying relative lithological changes within individual geological intervals. The detection of relative lateral changes in lithology is discussed further in the following section.

Figure 8.5 (next page) Synthetic earth model (left) and corresponding Vp/Vs analysis results (right) for (a) 40 m-thick interval bounded by two thin coal seams; (b) 15 m-thick interval bounded by two thin coal seams; and (c) 9 m-thick interval bounded by two thin coal seams. Each earth model comprises shale-rich country rock with a Vp/Vs of 2.3 ($Vp = 3350$ m/s; $Vs = 1450$ m/s), an 80 m-wide sandstone unit with a Vp/Vs of 1.65 ($Vp = 3900$ m/s; $Vs = 2363$ m/s), and two thin coal seams with Vp/Vs equal to 2.5 ($Vp = 2200$ m/s; $Vs = 880$ m/s). The wavelength of the corresponding seismic data is approximately 30 m. The absolute Vp/Vs values derived for each model are incorrect. This is due to seismic interference affecting TWT picks used to compute Vp/Vs . Note however, that the relative lithological variation in each of the models is successfully recovered by Vp/Vs analysis.

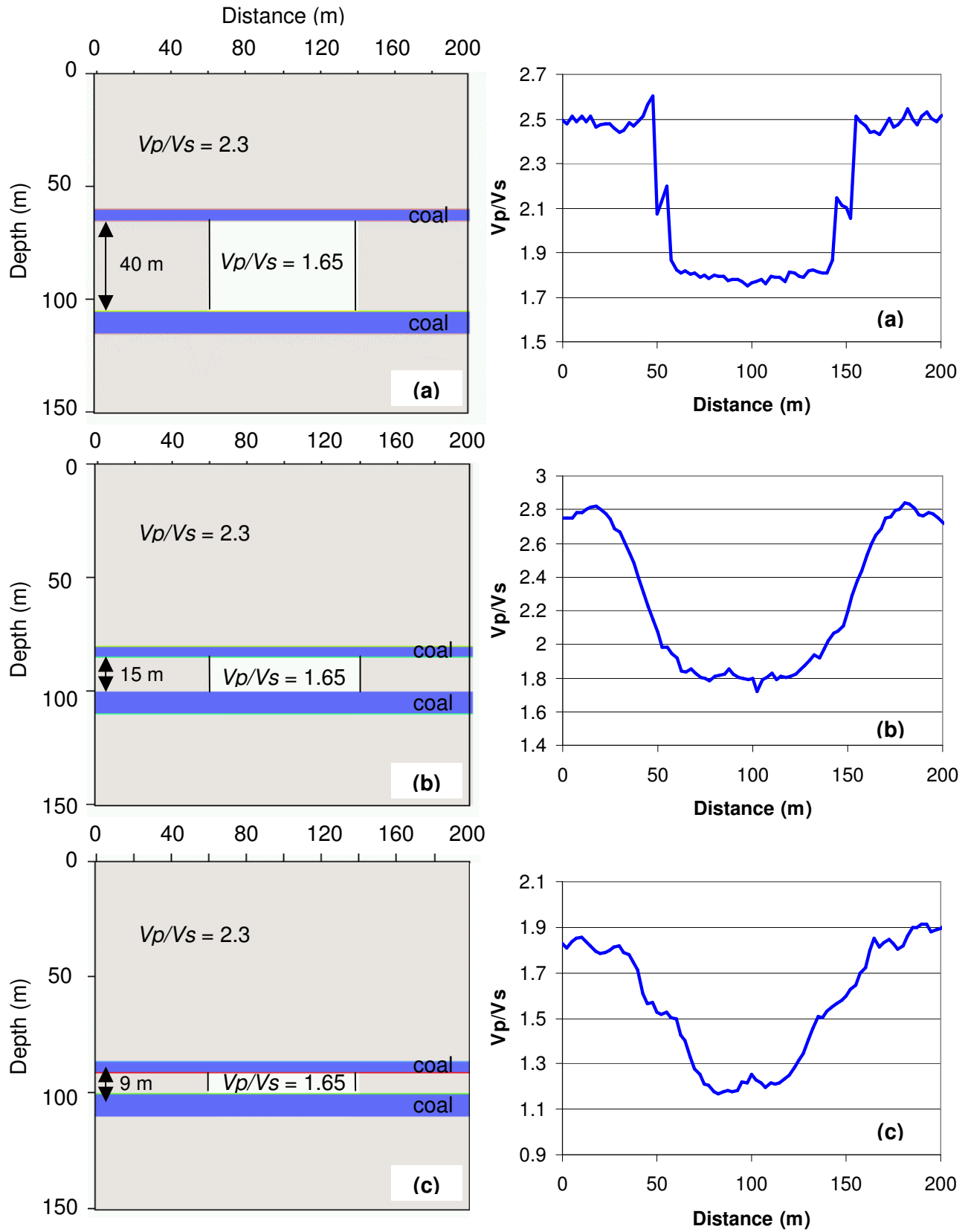


Figure 8.5 (see figure caption on previous page)

8.4 Detection of Lateral Geological Anomalies

While V_p/V_s analysis may not be able to yield absolute velocity-ratio and/or Poisson's Ratio measurements, it still has the potential to contribute more to our knowledge of the sub-surface than conventional P-wave seismic interpretation through its ability to detect lateral lithological variations. In order for V_p/V_s analysis to detect lateral geological anomalies, the anomaly itself must be of a sufficient size and exhibit a sufficient velocity-ratio contrast such that it creates a TWT response in the P and/or PS seismic sections.

Common seismic resolution limits dictate that in order for V_p/V_s analysis to detect a lateral geological anomaly, its width must be greater than the 'Fresnel zone'¹. Figure 8.6 illustrates this concept. Here, four sandstone units of varying width have been included in a synthetic earth model comprising two coal seams and a sandy country rock (Figure 8.6(a)). The corresponding seismic data have an estimated 'Fresnel zone' of 37 m. As expected, V_p/V_s analysis (Figure 8.6(b)) cannot resolve the 10 m- and 20 m-wide sandstone units. However, the V_p/V_s attribute clearly detects the 40 m- and 60 m-wide channels. Note that, the 'Fresnel zone' is dependent on the frequency content of the seismic data, the local seismic velocity, and the depth of the geological boundary. Hence, the required width of an anomaly for detection by V_p/V_s analysis will be site specific and dependent on local geology and data quality.

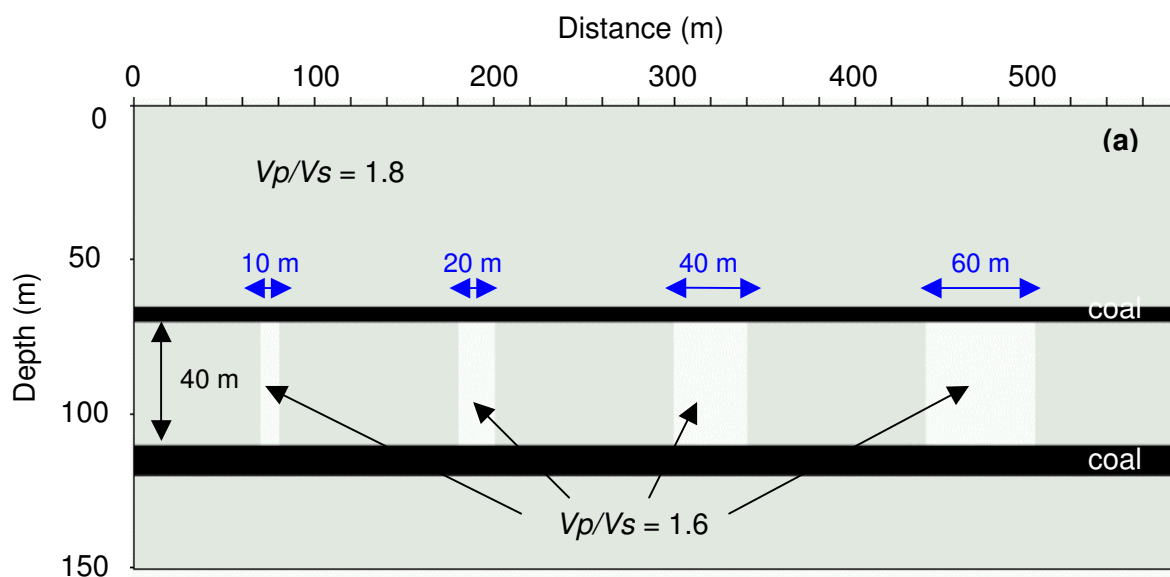


Figure 8.6(a) Synthetic earth model used to demonstrate lateral resolution limits of V_p/V_s analysis. The model comprises sandy country rock with a V_p/V_s of 1.8 ($V_p = 3600$ m/s; $V_s = 2000$ m/s), four sandstone channels with V_p/V_s equal to 1.6 ($V_p = 3900$ m/s; $V_s = 2450$ m/s), and two thin coal seams with V_p/V_s equal to 2.5 ($V_p = 2200$ m/s; $V_s = 880$ m/s).

¹ In reality, seismic energy is reflected from a zone on a geological boundary. Within this zone, any two or more reflecting points are considered indistinguishable from the earth's surface. This circular zone is called the 'Fresnel zone', the radius of which is defined as approximately equal to $\sqrt{(z\lambda)/2}$, where z is the depth of the reflector, $\lambda = v/f_D$ is the dominant wavelength of the data, v is the average seismic velocity, and f_D is the dominant frequency of the seismic signal.

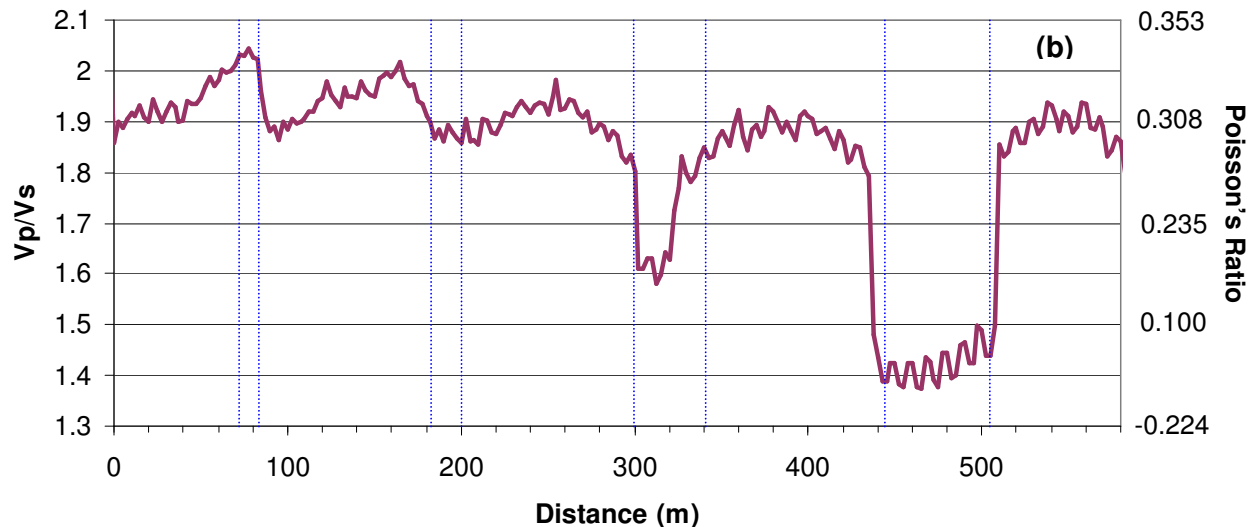


Figure 8.6(b) V_p/V_s measurements derived from synthetic data generated using the earth model in Figure 8.6(a). Equivalent Poisson's Ratio values are indicated on the right-hand axis. The 'Fresnel zone' of the synthetic seismic data is approximately 37 m. As expected, V_p/V_s analysis cannot resolve the 10 m- and 20 m-wide sand-rich channels. However, the 40 m- and 60 m- wide sandstone units are clearly detected. Note that, the dotted blue lines indicate the true physical location of each sandstone channel.

Note that, the width of the V_p/V_s anomaly associated with the 40 m-wide sandstone unit in Figure 8.6(b) is too narrow, and the V_p/V_s values are significantly smaller than those derived for the 60 m channel (albeit, the absolute V_p/V_s values for the 40 m channel are fortuitously correct). The width of the 40 m-wide channel cannot be accurately resolved because its width is very close to the lateral resolution limit of the seismic data. The absolute V_p/V_s values in the 40 m and 60 m channels are different because the latter is only affected by seismic interference in the coal-seam reflection events used to define the top and bottom of the interval. The V_p/V_s values in the 40 m channel are also being impacted by lateral resolution limits. This highlights the ambiguity that will exist in real-data V_p/V_s interpretation.

The velocity-ratio contrast necessary to instigate a response in the V_p/V_s attribute is dependent on the thickness of the anomaly (with thinner anomalies requiring greater velocity contrasts to ensure significant TWT variations in the seismic section/s). Extensive synthetic trials using representative coal geology, 10 m to 40 m-thick intervals, and typical coal-seismic frequencies, suggest that V_p/V_s analysis needs velocity-ratio contrasts greater than approximately 0.2 to reliably detect lateral differences in geology. This immediately suggests that V_p/V_s analysis is not suitable for detecting subtle lithology changes within one rock type. Figure 8.7 is a representative example illustrating the inability of V_p/V_s analysis to consistently predict relative V_p/V_s values for lithological anomalies with velocity-ratio contrasts less than 0.2. Obviously, we expect this sensitivity of V_p/V_s analysis to become worse when the seismic data are contaminated by significant noise and/or suffer from poor resolution (i.e. attenuation of high-frequency information).

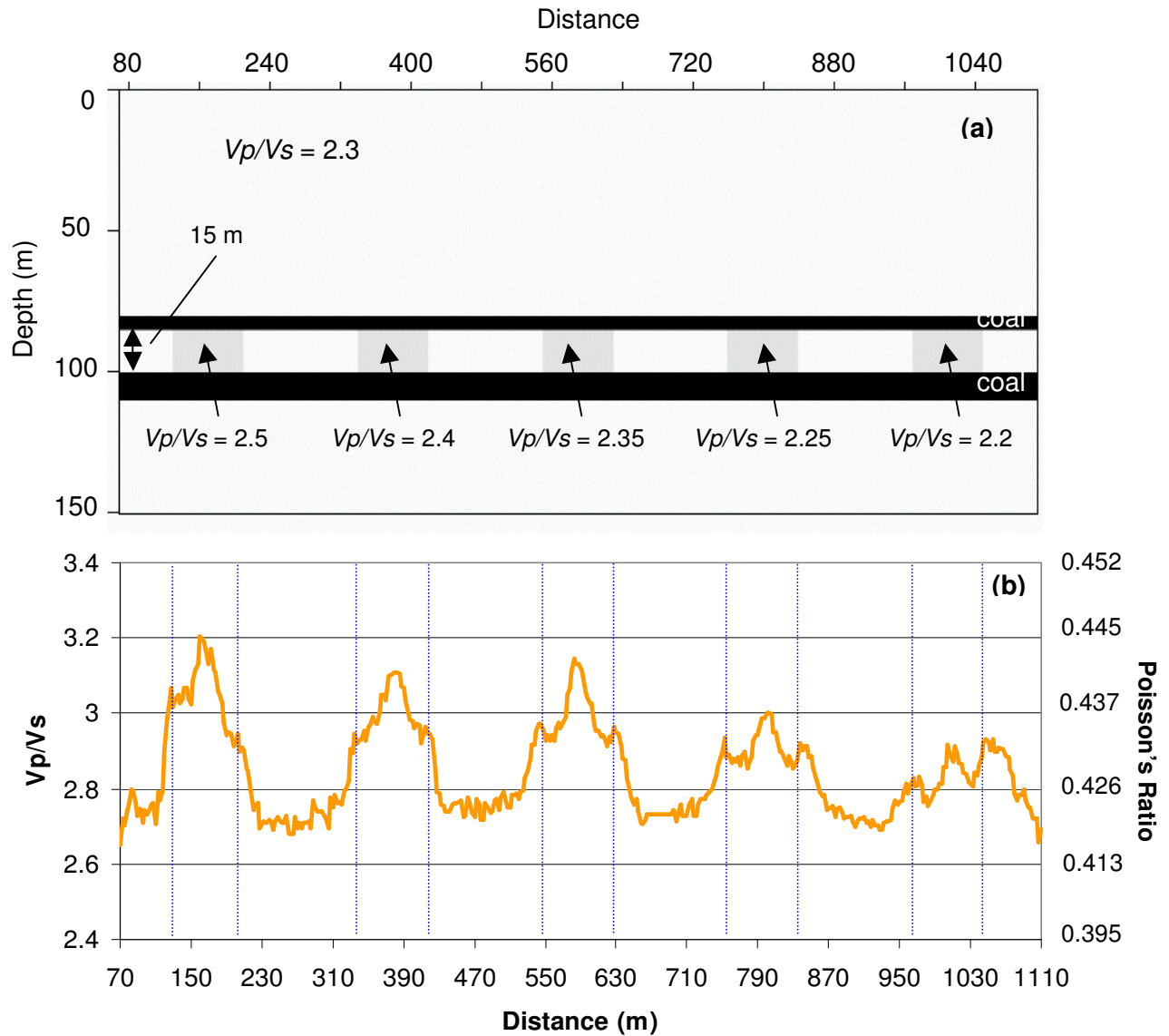


Figure 8.7 (a) Synthetic earth model used to demonstrate sensitivity of V_p/V_s analysis to velocity-ratio contrasts. The model comprises shale-rich country rock with a V_p/V_s of 2.3 ($V_p = 3350$ m/s; $V_s = 1450$ m/s), five 80 m-wide anomalies with various V_p/V_s values, and two thin coal seams with V_p/V_s equal to 2.5 ($V_p = 2200$ m/s; $V_s = 880$ m/s). (b) Corresponding V_p/V_s attribute. The dotted blue lines indicate the true physical location of each channel. The V_p/V_s curve gives the wrong relative information for the two right-hand anomalies, illustrating that V_p/V_s interpretation does not consistently predict lithology when velocity-ratio contrasts are less than 0.2.

There are a number of other factors that will influence the computed V_p/V_s attribute in addition to the physical properties of the geological anomaly we have discussed above. Most notably, errors and ambiguities in the P and PS processing flows (e.g. personal selection of stacking-velocity functions) can be shown to introduce errors of 0.2 – 0.3 in the V_p/V_s attribute. This suggests that errors of this order must be accommodated in the V_p/V_s interpretation process. Significant random and coherent noise (e.g. multiple energy) can also create non-geological TWT variations

in reflection events. In the situation where noise obviously contaminates a reflection event, it should not be used to conduct V_p/V_s analysis (Figure 8.8). Structures will also create TWT anomalies that will negatively impact on V_p/V_s analysis. These three sources of spurious TWT variations in the seismic sections must be taken into consideration when interpreting the V_p/V_s curve. Section 9.2 summarises how practical real-data V_p/V_s interpretation can attempt to work around these issues.

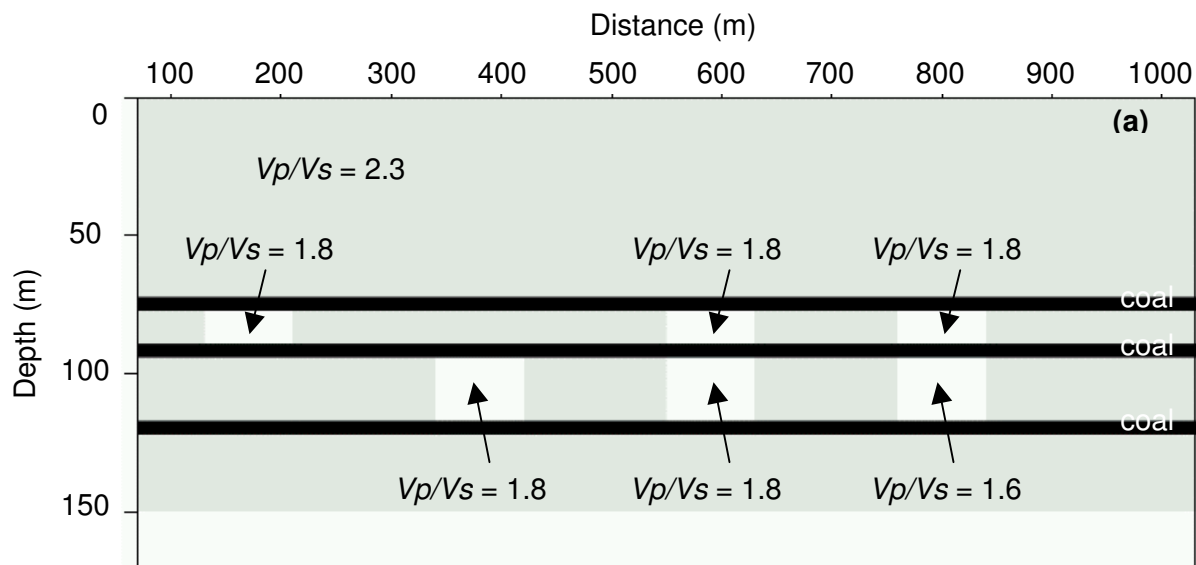


Figure 8.8(a) Synthetic earth model used to demonstrate that reflection events contaminated with multiple energy should not be used for V_p/V_s analysis. The model comprises shale-rich country rock with a V_p/V_s of 2.3 ($V_p = 3350$ m/s; $V_s = 1450$ m/s), a number of sandstone channels (V_p/V_s values marked), and three thin coal seams with V_p/V_s equal to 2.5 ($V_p = 2200$ m/s; $V_s = 880$ m/s). The coal seams are used to define two geological intervals for V_p/V_s analysis – the top interval is 12 m thick, the bottom interval is 23 m thick.

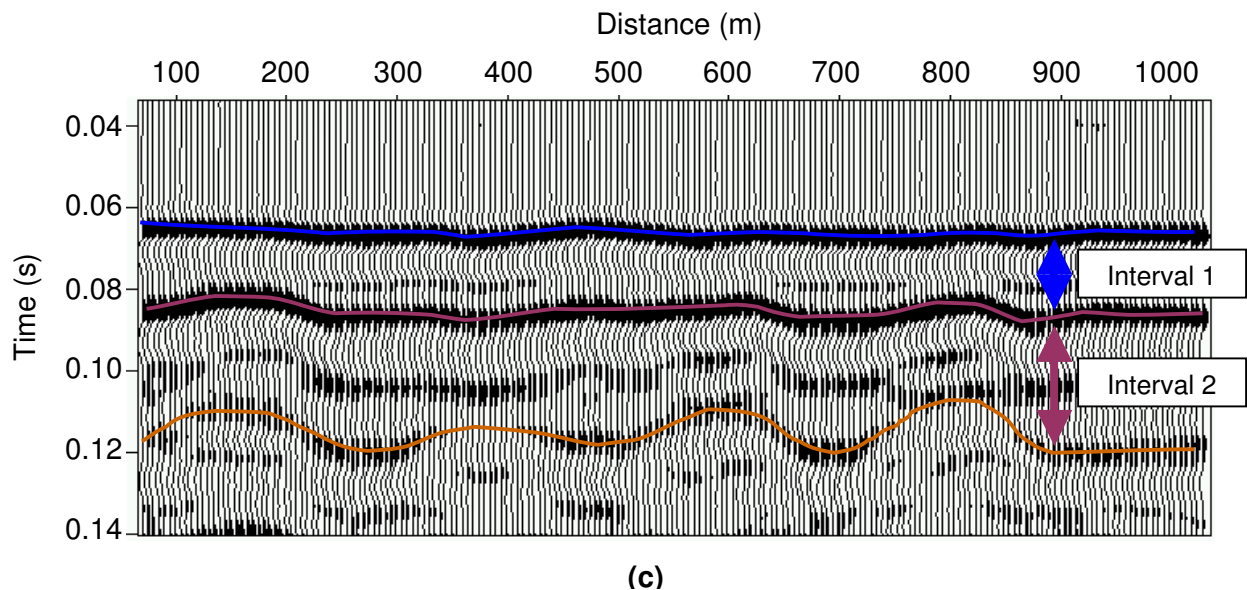
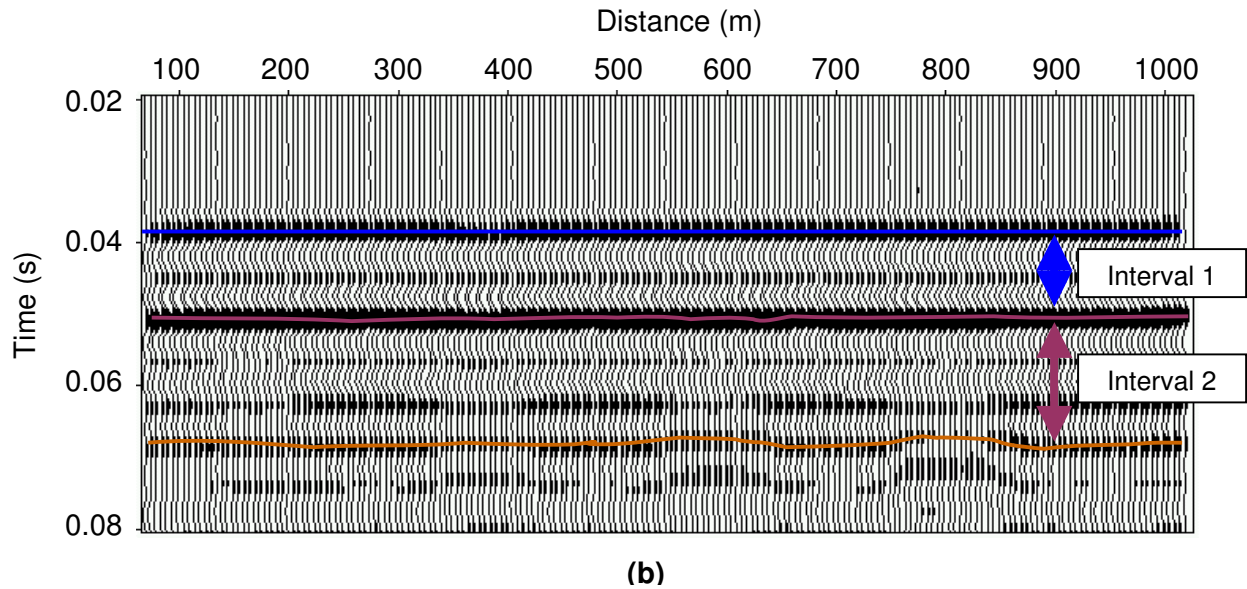


Figure 8.8 (b) P-wave and (c) PS-wave seismic sections corresponding to the earth model shown in Figure 8.8(a). See Appendix I for details on the synthetic seismic modelling used to generate these data. Three reflection events corresponding to the three coal seams are identified. It is apparent that the lower seismic reflection event is being severely attenuated by multiple energy and suffers from a poor signal-to-noise ratio. Note that the time axes of these sections have been adjusted appropriately to provide a comparable depth perspective.

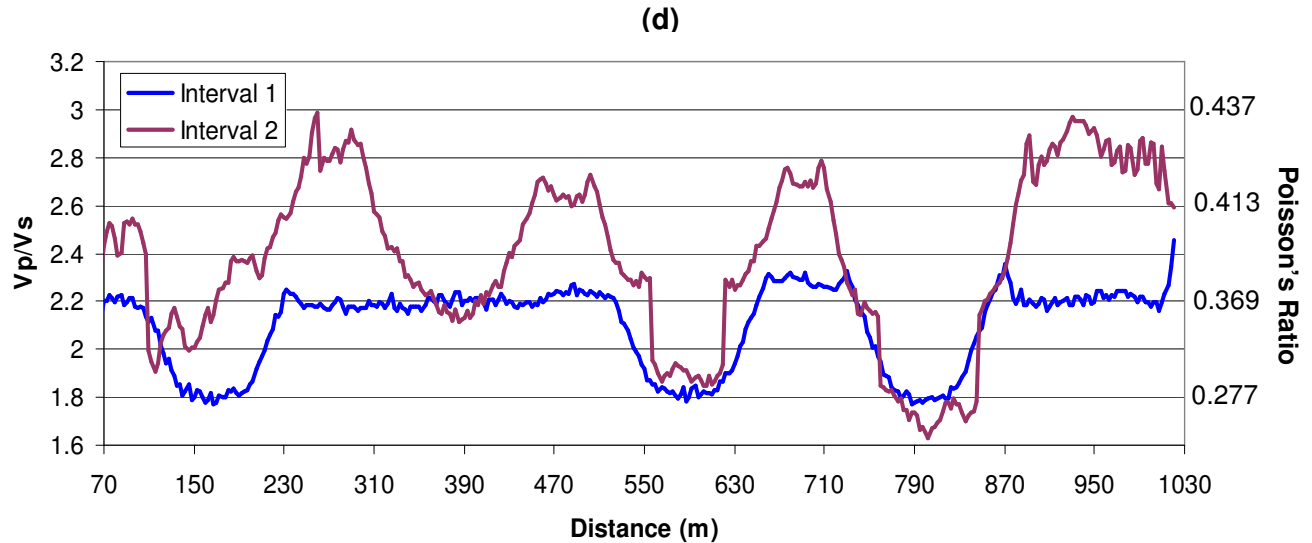


Figure 8.8(d) V_p/V_s measurements derived from the synthetic seismic sections shown in Figures 8.8(b) and 8.8(c). Equivalent Poisson's Ratio values are indicated on the right-hand axis. As we expect in the coal environment, absolute V_p/V_s values are incorrect. However, relative variations in the V_p/V_s attribute for Interval 1 (blue) accurately detects the three sand-rich channels. In contrast, V_p/V_s values for Interval 2 (maroon) are erroneous. For example, there should be no sand-rich channel between approximately 100 – 180 m. This incorrect channel feature is caused by multiple energy from the overlying sandstone channel interfering with the deeper primary reflection event. Only reflection events with a strong signal-to-noise ratio should be used for V_p/V_s analysis.

CHAPTER NINE

V_p/V_s INTERPRETATION: REAL DATA EXAMPLES

9.1 Introduction

Two of our ACARP trial 3C seismic datasets image multiple coal seams, making them suitable for demonstrating *V_p/V_s* analysis. This chapter discusses practical issues for real-data *V_p/V_s* analysis, and presents results from the integrated P/PS interpretation of Trial #2 and Trial #3. The real-data examples given here represent the first attempts to tie results from the *V_p/V_s* interpretation of coal-seismic data to geological information available from borehole logs.

9.2 *V_p/V_s* Interpretation of Real Data

The synthetic data results presented in Chapter 8 demonstrate that real-data *V_p/V_s* analysis is best suited for detecting broad zones (of the order of 30 – 50 m or more) of significant lithological variation (e.g. sandstone vs shale). To help reduce spurious interpretation results associated with processing artefacts, seismic noise and structures, we suggest that real-data *V_p/V_s* analysis incorporate the following practical procedures: (i) only use strong coal-seam reflection events to define geological intervals, (ii) only use smoothed TWT horizons to help remove the effect of random noise and minor structures, (iii) avoid *V_p/V_s* interpretation about large-scale structures, and (iv) do not read significance into small amplitude variations (less than approximately 0.2) in the resultant *V_p/V_s* curves.

The real earth is much more complicated than the simple synthetic earth models used in Chapter 8, and any single interval defined for real-data *V_p/V_s* analysis will generally comprise many different geological layers. Consequently, the *V_p/V_s* curve will effectively measure the average velocity-ratio across an interval. This means that it is not possible to differentiate, say, between intervals comprising a series of upward-fining sand-shale sequences from intervals that comprise a random distribution of sand- and shale-rich sequences. Similarly, if an interval shows an increase in sand content, it is not possible to determine whether this is a general increase in sand across all layers in the interval, or whether a sandstone layer has been added to the geologic column. Figure 9.1 helps to illustrate the implications of this behaviour. A detailed synthetic earth model (based on a line of borehole data from the Bowen Basin) is given in Figure 9.1(a). Four geological intervals are marked (with thicknesses typical of real-data *V_p/V_s* analysis). RMS (root-mean-square) *V_p/V_s* curves for each of these defined geological intervals (computed directly from the synthetic earth model) are shown in Figures 9.1(b) to 9.1(e). The *V_p/V_s* curves reflect all of the lithological changes that exist within each interval. They are effectively the best results we could hope to get with *V_p/V_s* analysis, yet specific information such as whether or not a coal seam has a shale floor, or a massive sandstone unit sitting 5 m above it etc, is lost in the averaging process. This illustrates that real-data *V_p/V_s* analysis does not have the ability to remotely acquire high-resolution geological detail about the roof and floor of a coal seam. However, as we will demonstrate, *V_p/V_s* analysis can highlight broad zones of relatively different lithology. This information, when combined with other key indicators available to a mine geologist, may help isolate areas that require further investigation prior to mining.

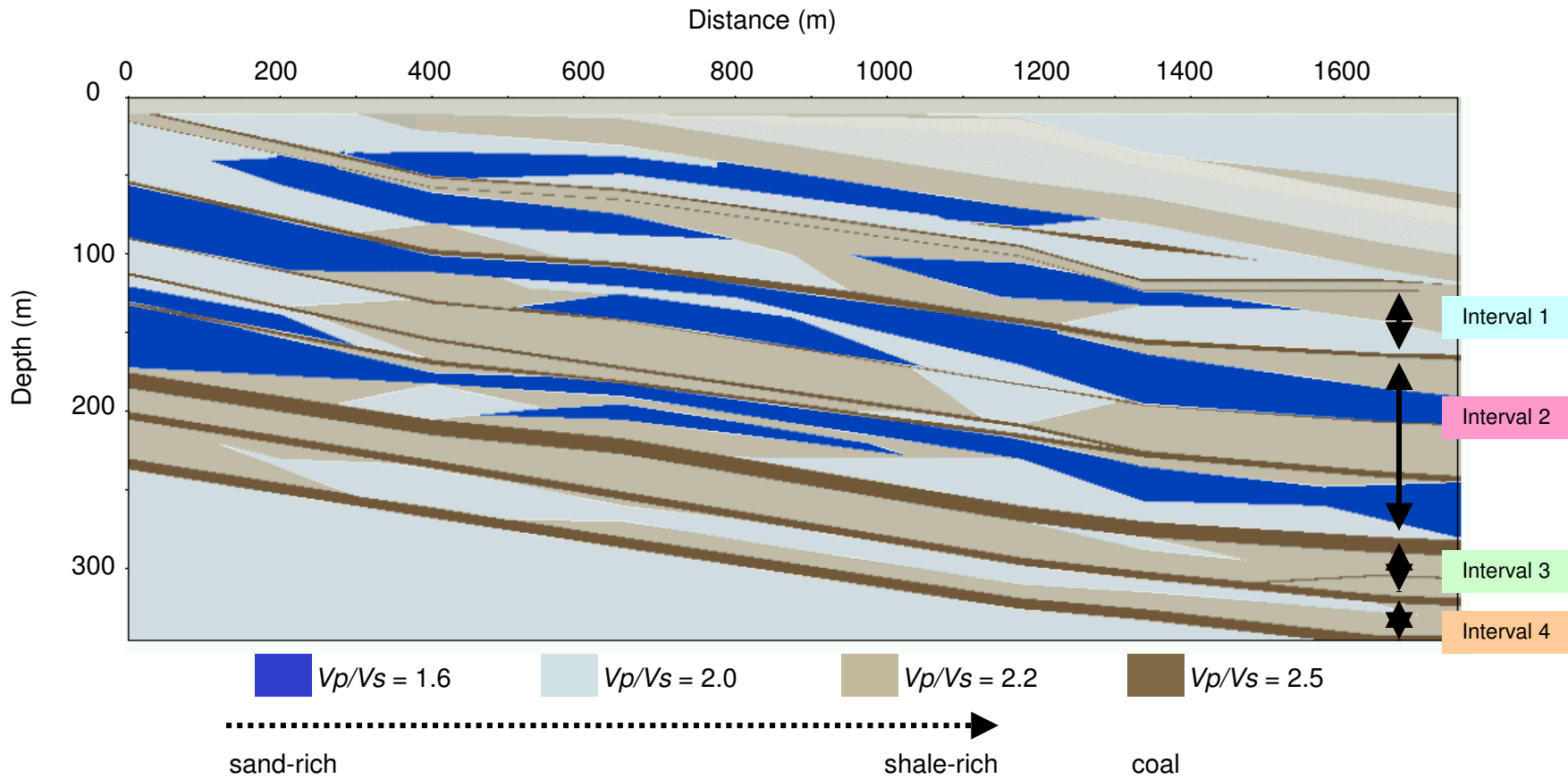


Figure 9.1 (a) Detailed synthetic earth model created using log data from a line of boreholes in the Bowen Basin. Vp/Vs values for each geological unit are shown. Four geological intervals, bound by thin coal seams, are indicated. These geological intervals have been defined based on typical interval thicknesses we work with for real-data Vp/Vs analysis.

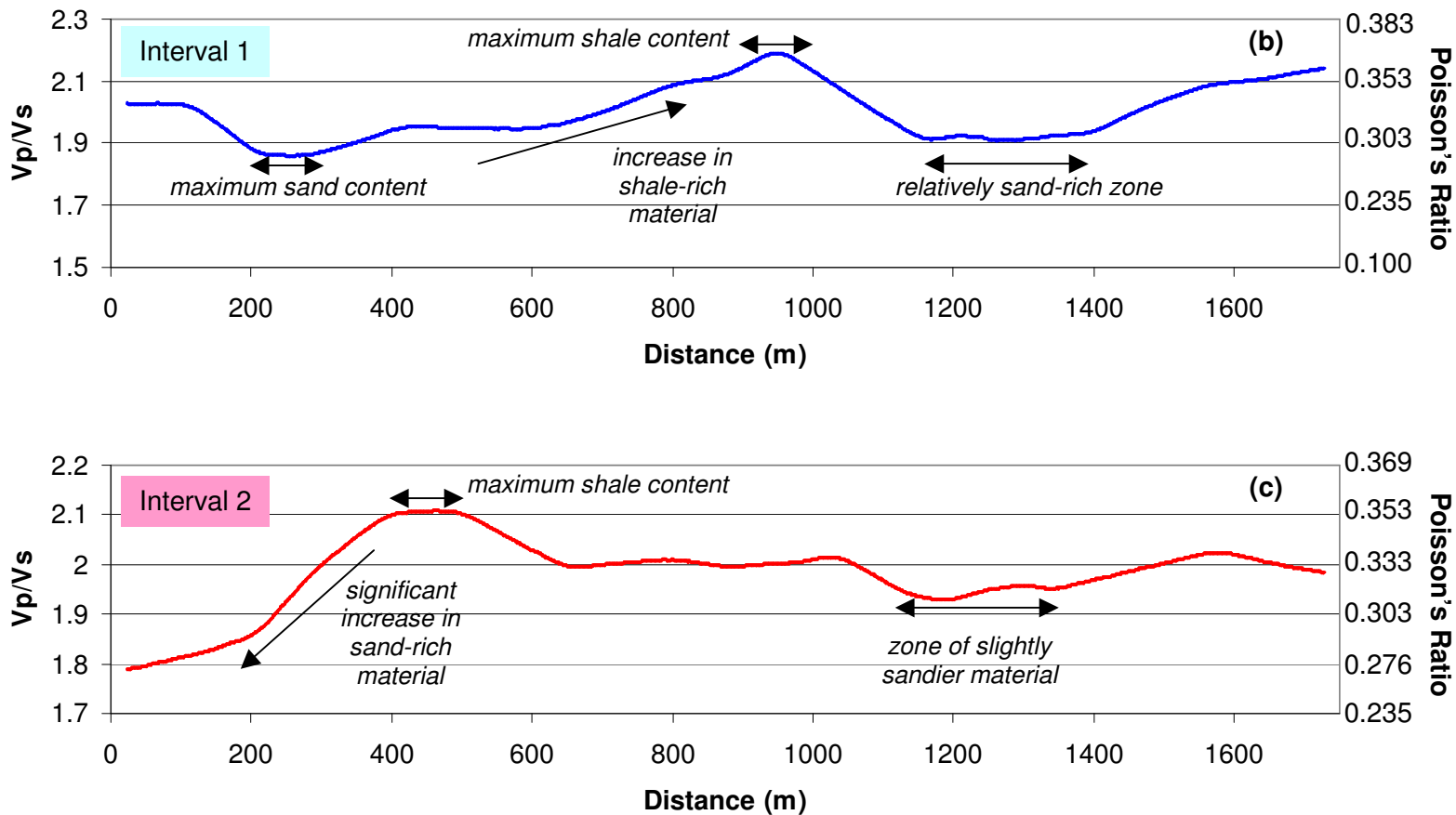


Figure 9.1 RMS V_p/V_s values computed directly from the synthetic earth model shown in Figure 9.1(a) for (b) Interval 1 and (c) Interval 2. Equivalent Poisson's Ratio values are indicated on the right-hand axis. Italicised comments summarise the V_p/V_s information we can extract from the V_p/V_s curves. All of the V_p/V_s variations in the synthetic earth model are reflected in these V_p/V_s curves. However, the averaging of the V_p/V_s information across the entire interval results in loss of detail with regards to where in the interval sand or shale content may increase or decrease. (Note also that, for real-data V_p/V_s analysis we couldn't reliably interpret the very small variations (< 0.2) seen in these synthetic V_p/V_s curves.)

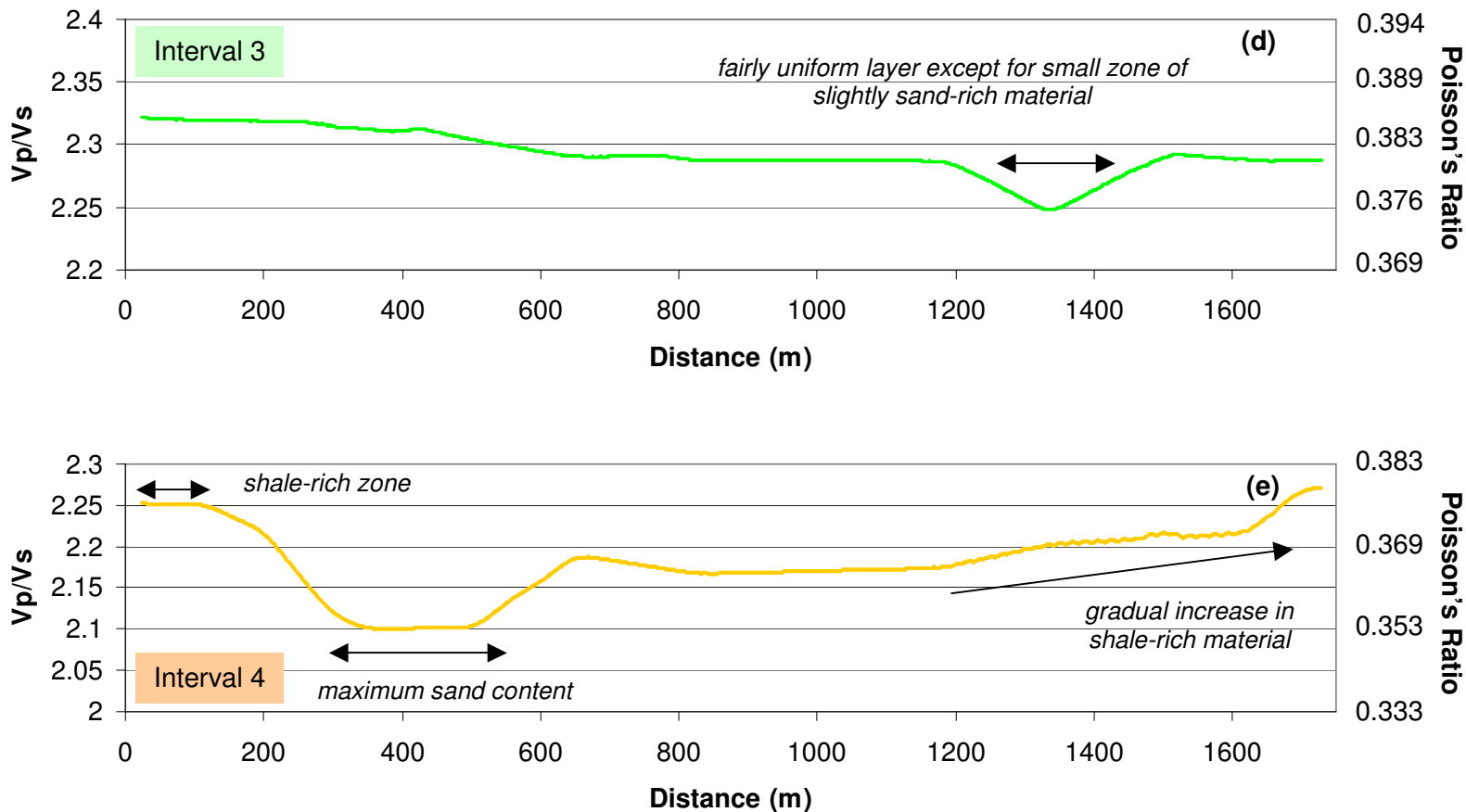


Figure 9.1 RMS V_p/V_s values computed directly from the synthetic earth model shown in Figure 9.1(a) for (d) Interval 3 and (e) Interval 4. Equivalent Poisson's Ratio values are indicated on the right-hand axis. Italicised comments summarise the V_p/V_s information we can extract from the V_p/V_s curves. All of the V_p/V_s variations in the synthetic earth model are reflected in these V_p/V_s curves. However, the averaging of the V_p/V_s information across the entire interval results in loss of detail with regards to where in the interval sand or shale content may increase or decrease. (Note also that, for real-data V_p/V_s analysis we couldn't reliably interpret the very small variations (< 0.2) seen in these synthetic V_p/V_s curves.)

9.3 Results from Trial #2

Figure 6.1 shows the final P and PS sections for Trial Dataset #2. Three seismic horizons associated with coal seams have been interpreted. Consequently, there are two intervals available for V_p/V_s analysis. As noted in Section 9.2, the TWT picks for these horizons have been smoothed to help reduce noise in the V_p/V_s attribute. Note that, the middle seismic horizon is affected by a relatively large structure. This will negatively impact on the V_p/V_s attribute. Figure 9.2 displays the V_p/V_s interpretation results for the two intervals. Smoothed gamma logs from boreholes along the line are displayed with the V_p/V_s attribute to help validate the interpretation results since it is believed that the V_p/V_s attribute should reveal similar lithological information. The results are summarised below.

Interval 1

Figure 9.2(a) shows the V_p/V_s curve for Interval 1. The V_p/V_s attribute predicts that the interval contains less sand material along the first third of the line, compared to the remainder of the line. Note that, a fault intersecting the middle seismic horizon creates an artificial thinning of this seismic interval about CDP/CCPs 700-750 in the PS section. Thus, the relative drop in V_p/V_s values in this zone cannot be interpreted to reflect real lithological changes in the interval. The fault is the likely reason why the computed V_p/V_s values are not in agreement with the borehole data about CDP/CCP 740.

Interval 2

The V_p/V_s curve for the second interval (Figure 9.2(b)) predicts that lithology within this interval for the first two-thirds of the line is relatively sand-rich (with a narrow zone of increased sandy material about CDP/CCP 590 – this anomaly could warrant further investigation). The right end of the line is dominated by a zone of high V_p/V_s values. This is consistent with borehole data along the line. However, most of the high V_p/V_s values lie within the neighbourhood of the fault that intersects the middle seismic horizon. Since the fault creates an artificial thickening of this interval on the PS section, it will result in artificially high V_p/V_s values. Consequently, these higher V_p/V_s values should not be considered reliable in terms of mapping a relative change in lithology.

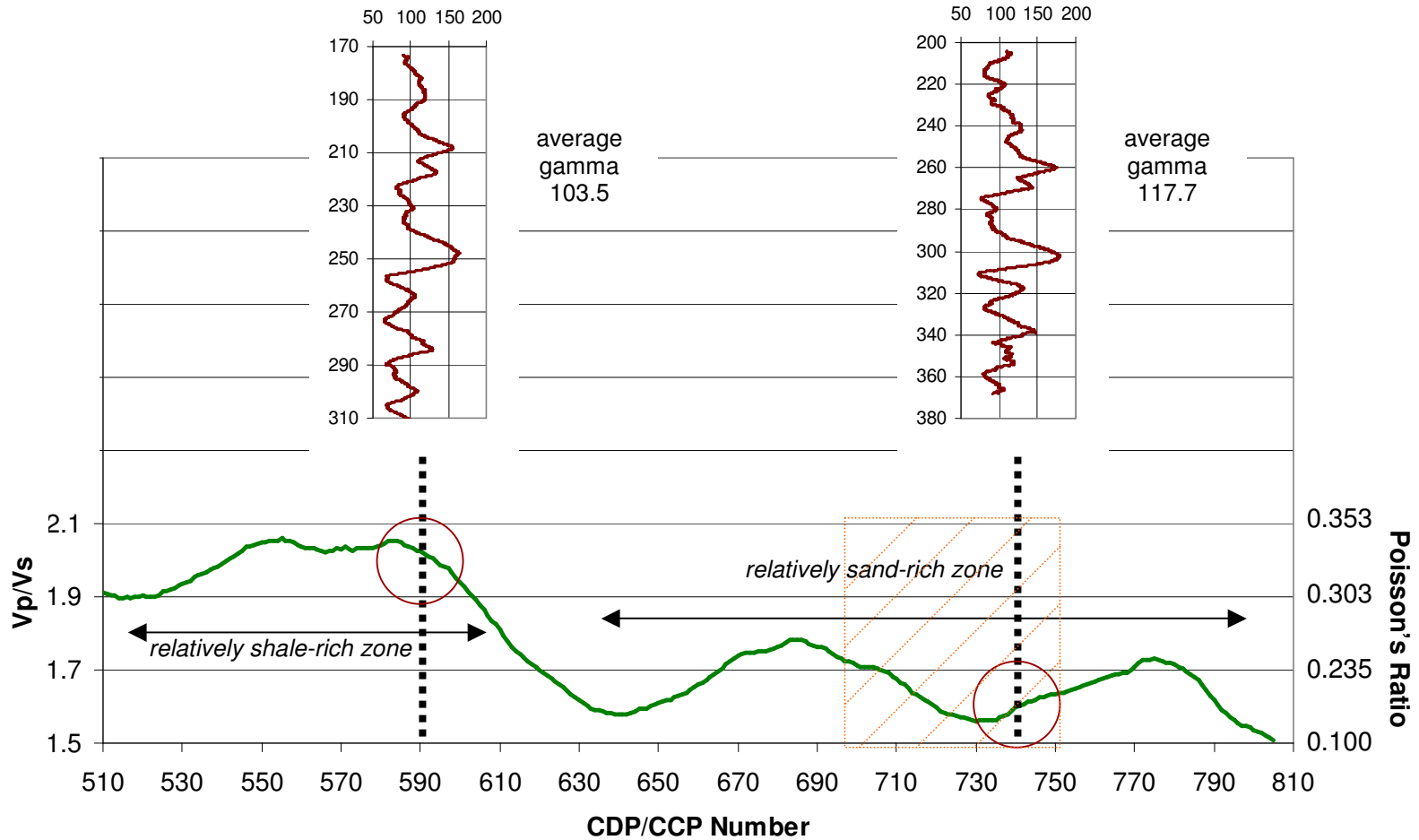


Figure 9.2 (a) V_p/V_s interpretation for Interval 1 from Trial #2. The predicted V_p/V_s values (or equivalent Poisson's Ratio values) are displayed. Italicised comments highlight the interpretation results. Portions of smoothed gamma logs corresponding to this interval are displayed for each borehole along the seismic line (log display: vertical axis – depth (m); horizontal axis – API). Note that, the zone of influence of an interpreted structure is highlighted by the orange dotted lines.

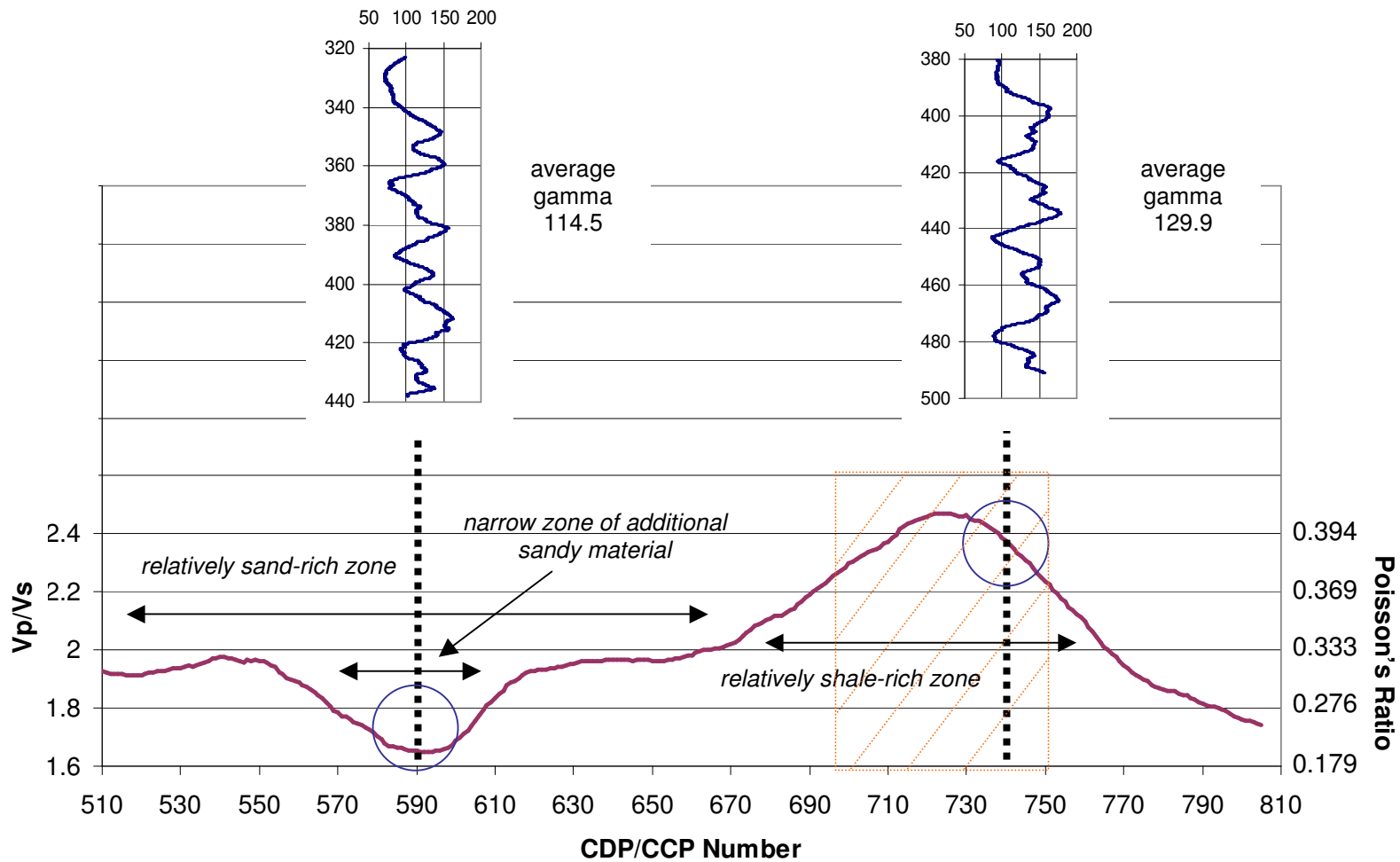


Figure 9.2 (b) V_p/V_s interpretation for Interval 2 from Trial #2. The predicted V_p/V_s values (or equivalent Poisson's Ratio values) are displayed. Italicised comments highlight the interpretation results. Portions of smoothed gamma logs corresponding to this interval are displayed for each borehole along the seismic line (log display: vertical axis – depth (m); horizontal axis – API). Note that, the zone of influence of an interpreted structure is highlighted by the orange dotted lines.

9.4 Results from Trial #3

The final P and PS sections for Trial Dataset #3 are shown in Figure 7.5. Five seismic horizons associated with coal seams have been interpreted. This results in four intervals over which V_p/V_s analysis can be conducted. Again, the TWT picks along the interpreted horizons have been smoothed to help reduce noise in the V_p/V_s attribute. Figure 9.3 displays the V_p/V_s interpretation results for each interval. As for Trial #2, smoothed gamma logs from boreholes along the line are included in Figure 9.3 to help validate the V_p/V_s interpretation. The interpretation results are summarised below. Recall that the V_p/V_s curves from each individual interval cannot be compared to any other since the absolute V_p/V_s values are not meaningful.

Interval 1

The V_p/V_s curve for the shallowest interval (Figure 9.3(a)) predicts a gradual increase in shale content from the beginning of the line to approximately CDP/CCP 460. The shale content of the interval then appears to drop rapidly along the remainder of the line. This lithological trend is not observed in the gamma logs along the line, which instead suggest the average lithology is fairly constant at each borehole location. Note that, the rapid drop in V_p/V_s values at the right end of the line is a result of the TWT interval thinning on the PS section but not the P section – where we believe the deeper PS reflection events are responding to a thick sandstone channel (Section 3.4). The extreme seismic response observed in this dataset strongly supports a significant lithology change. It is not clear why this does not create a large change in the gamma logs. It is possible that the poor correlation of the V_p/V_s attribute with the gamma logs could be a result of an erroneous correlation of reflection events on the P and PS seismic sections.

Interval 2

Figure 9.3(b) illustrates the V_p/V_s curve for the second interval. The V_p/V_s attribute predicts that the lithology in this interval is relatively constant across the first half of the line, and then gradually becomes more sand-rich. This is in agreement with the fact that, for this interval, the right-most borehole contains the largest proportion of sand-rich geology relative to the other boreholes along the line.

Interval 3

In Figure 9.3(c) there are two zones of relatively high V_p/V_s values along the line – at CDP/CCP 300-350 and CDP/CCP 430-460. The relatively high V_p/V_s values on the right coincide with interpreted faulting. The high V_p/V_s values could indicate a zone of intense fracturing about multiple minor faults. (In contrast, a clean fault with less broken ground around it wouldn't necessarily affect the V_p/V_s curve.) As a result, we can't reliably interpret this zone of high V_p/V_s values as a real change in rock type. The zone of high V_p/V_s values on the left end of the line is not associated with any interpreted structure. However, the V_p/V_s values don't match the lithology indicated by the borehole data. In addition, the relative V_p/V_s values at the two boreholes on the right don't accurately reflect the relative variations in the gamma logs. This may

indicate that, for this particular dataset, this interval is too thin for V_p/V_s analysis (i.e. the seismic horizons picked to define this geological interval are not accurately tracking the top and base coal seam used to define the interval).

Interval 4

The V_p/V_s curve for Interval 4 is shown in Figure 9.3(d). The interval is predicted to have a relatively sand-rich lithology along the first two-thirds of the line. There is a very slight increase in shale content predicted towards the right end of the line. Note however, the V_p/V_s values at the borehole locations do not deviate by more than 0.2, and are therefore not considered to be significantly different. Based on the borehole gamma logs however, we expect that the V_p/V_s values at the left-most borehole location should be significantly lower than the V_p/V_s values at the other two borehole locations. The ability of V_p/V_s analysis to predict geology in this interval is questionable.

9.5 Discussion

Synthetic experiments (Chapter 8) have clearly demonstrated that, due to the nature of seismic data (e.g. resolution limits, sensitivity to velocity changes, noise), V_p/V_s analysis cannot hope to be a remote-imaging tool that is capable of recovering continuous, high-resolution geological detail from the sub-surface. However, V_p/V_s analysis has the potential to indicate broad lithological changes. Real data examples from Trial #2 are inconclusive in demonstrating the potential of V_p/V_s analysis since faulting is affecting the attribute at one of the borehole control points. Real data examples from Trial #3 produce mixed results. There appear to be issues with TWT picks, interval thicknesses and minor faulting. However, there are instances where we believe V_p/V_s analysis is demonstrating an ability to indicate broad lithological changes - whether or not these relatively few success are coincidental remains to be seen. Further validated trials will help assess the robustness of this seismic attribute and help streamline practical interpretation procedures.

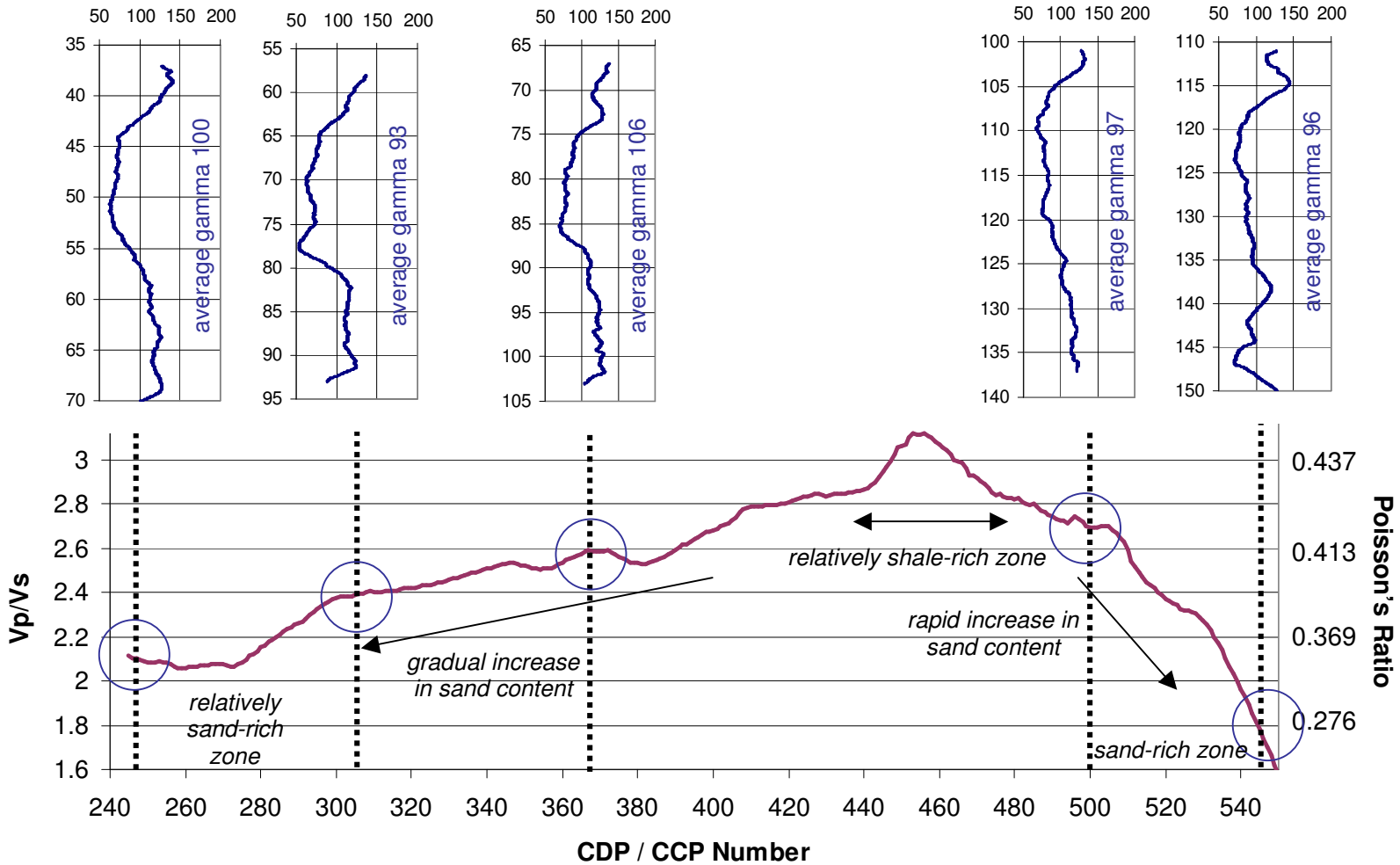


Figure 9.3 (a) V_p/V_s interpretation for Interval 1 from Trial #3. The predicted V_p/V_s values (or equivalent Poisson's Ratio values) are displayed. Italicised comments highlight the interpretation results. Portions of smoothed gamma logs corresponding to this interval are displayed for each borehole along the seismic line (log display: vertical axis – depth (m); horizontal axis – API).

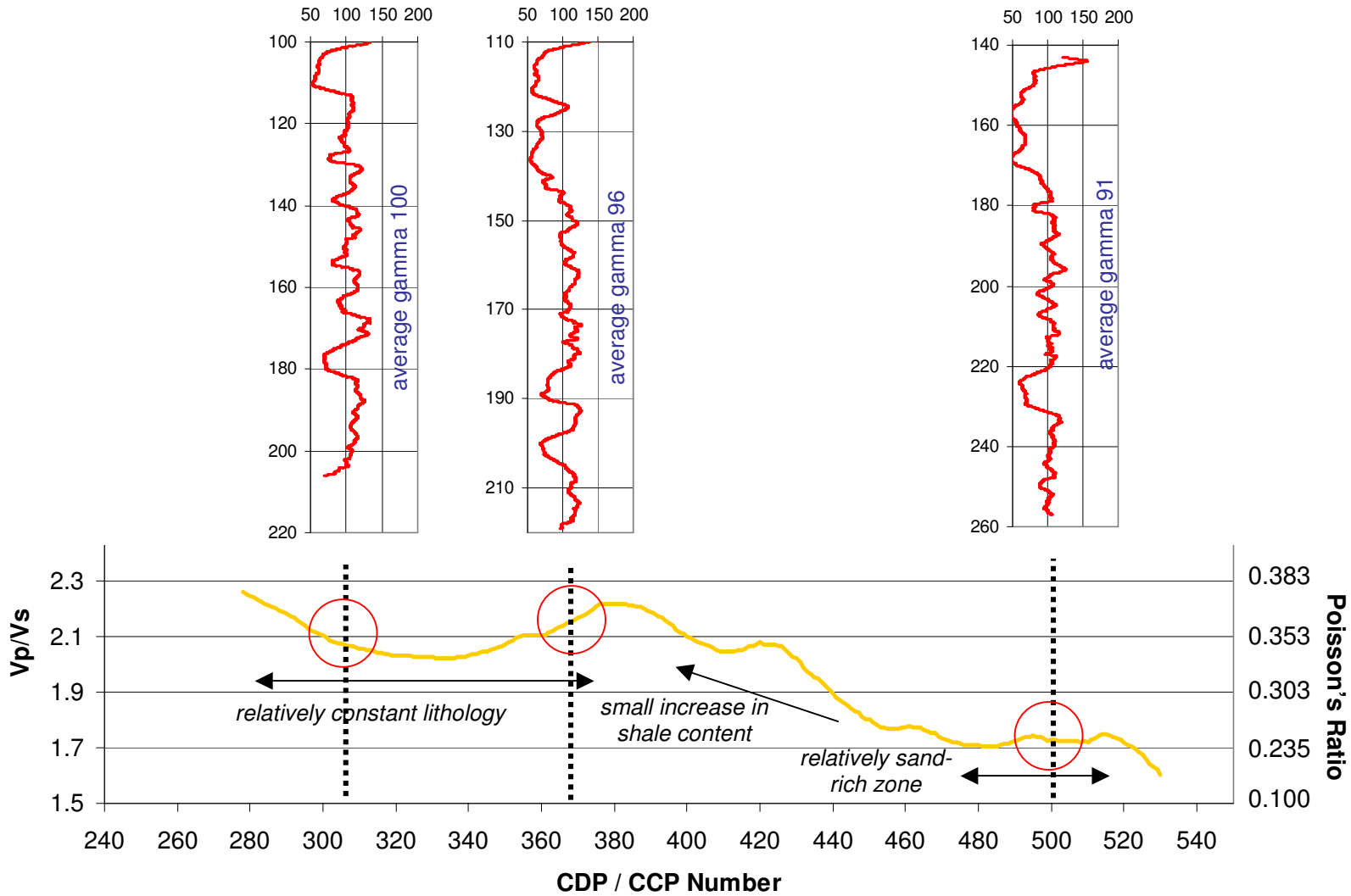


Figure 9.3 (b) V_p/V_s interpretation for Interval 2 from Trial #3. The predicted V_p/V_s values (or equivalent Poisson's Ratio values) are displayed. Italicised comments highlight the interpretation results. Portions of smoothed gamma logs corresponding to this interval are displayed for each borehole along the seismic line (log display: vertical axis – depth (m); horizontal axis – API).

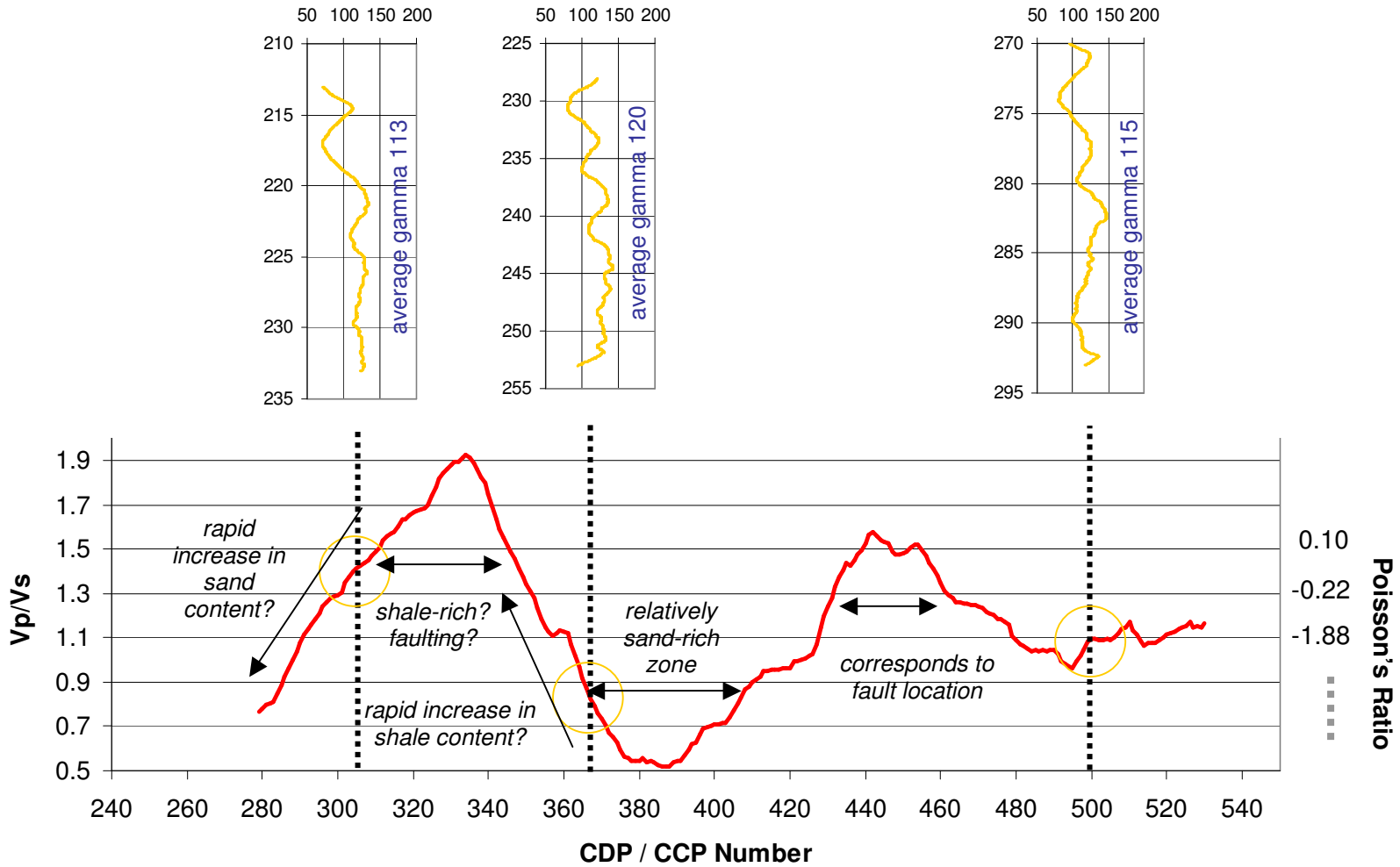


Figure 9.3 (c) V_p/V_s interpretation for Interval 3 from Trial #3. The predicted V_p/V_s values (or equivalent Poisson's Ratio values) are displayed. Italicised comments highlight the interpretation results. Portions of smoothed gamma logs corresponding to this interval are displayed for each borehole along the seismic line (log display: vertical axis – depth (m); horizontal axis – API).

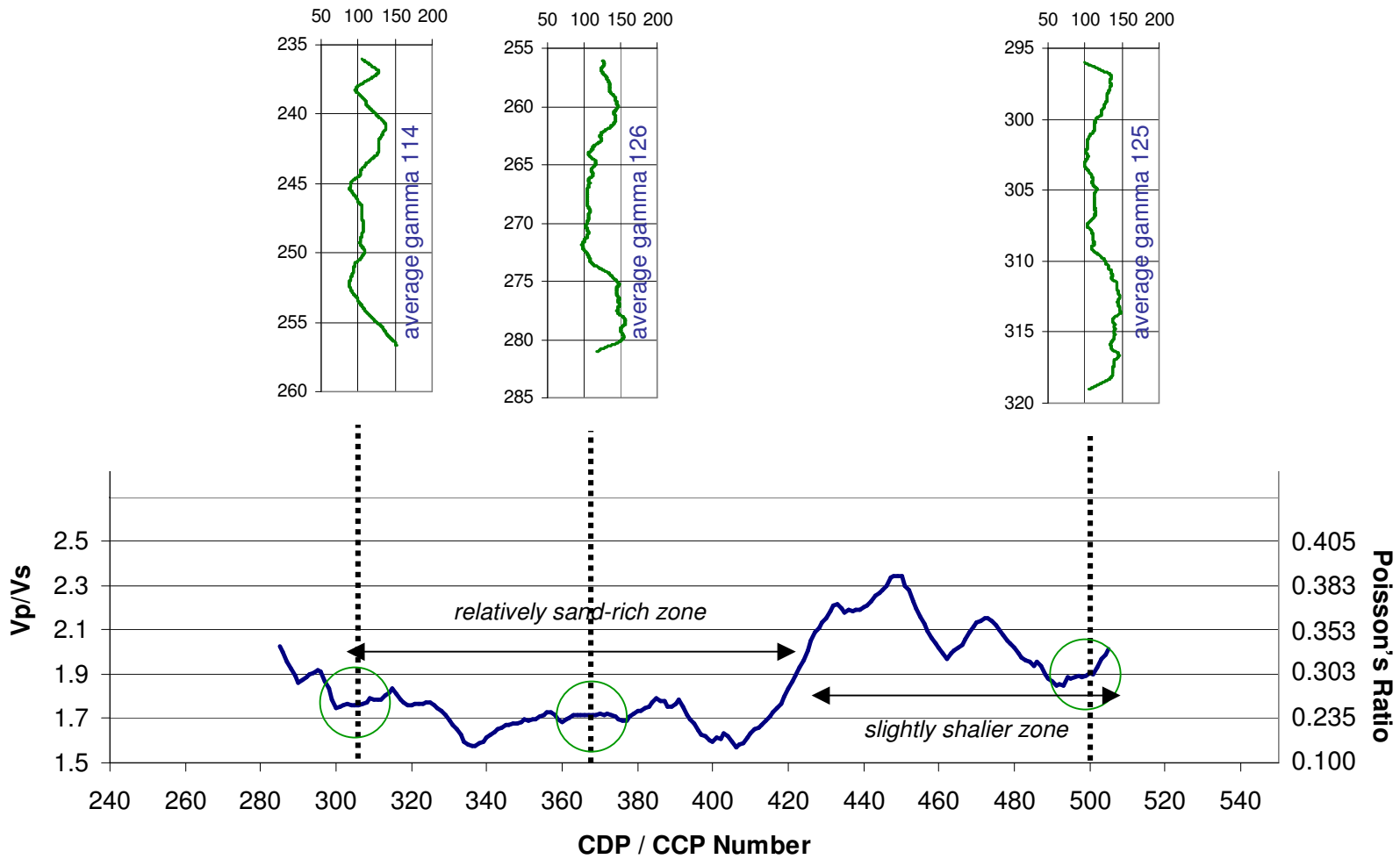


Figure 9.3 (d) V_p/V_s interpretation for Interval 4 from Trial #3. The predicted V_p/V_s values (or equivalent Poisson's Ratio values) are displayed. Italicised comments highlight the interpretation results. Portions of smoothed gamma logs corresponding to this interval are displayed for each borehole along the seismic line (log display: vertical axis – depth (m); horizontal axis – API).

CHAPTER TEN

INTEGRATED PROCESSING OF THE HORIZONTAL COMPONENTS OF DATA

10.1 Introduction

To date, we have only considered the inline component of our 3C data (i.e. the horizontal component parallel to line of recording) to derive our converted-wave seismic images. This is because in the absence of lateral heterogeneities, seismic wave theory predicts that most of the converted-wave seismic energy will have particle motion parallel to the source-receiver azimuth. We have, however, observed in our real 3C seismic data irregular occurrences of PS energy on the crossline component of data (i.e. the horizontal component 90° clockwise from the inline component). The work presented in this chapter begins to examine whether this crossline PS energy can contribute to our converted-wave imaging and/or supply us with additional information about the sub-surface. A number of basic ideas relating to integrated processing of the inline and crossline components of data are discussed, and a preliminary examination of one of our 3C seismic datasets is undertaken.

10.2 Seismic Energy on the Crossline Component

In general, there are three reasons we can expect PS energy to be recorded on the crossline component of a 2D-3C seismic dataset:

- (i) the 3C geophones are misaligned and poorly planted so that the inline component does not lie along the source-receiver azimuth;
- (ii) the 2D survey line is not straight; and
- (iii) the earth is laterally heterogeneous (e.g. reflector dips, structures, and/or anisotropy are present).

With respect to (i) above, we are confident that our geophone-planting and subsequent cross-checking procedures, for the most part, prevent misalignment of our 3C geophones. Isolated geophones may suffer from misalignment. However, this would certainly not be responsible for PS energy being recorded on the crossline component of successive geophones.

With respect to (ii) above, the 3C seismic data we are considering here have been acquired along straight survey lines. Note however, if a 2D seismic line is not straight, it is possible to mathematically rotate the recorded signal using the physical source-receiver azimuth to ensure the desired PS energy sits on the 'inline component' used to produce the PS stack (Velseis, 2003).

With respect to (iii) above, we do not see evidence of the geological dips and structures necessary for contamination of the crossline component with significant out-of-plane P and PS energy. We do, however, expect that seismic anisotropy exists in our 3C seismic survey areas. Anisotropy is the large-scale manifestation of small-scale heterogeneity which has a preferred orientation (e.g. finely-layered sediments, aligned stress fractures etc). Anisotropy can cause S waves to begin to

vibrate out of the source-receiver azimuth plane, into planes perpendicular and parallel to the preferred directions of the rock. This propagation behaviour is referred to as shear-wave splitting (SWS).

Thus, of the potential sources of converted-wave energy on the crossline component of our 2D-3C data, we currently believe SWS is responsible for the anomalous PS energy we observe. This suggests that consideration of the PS energy on the crossline component may reveal new information about anisotropy in the sub-surface. Furthermore, understanding the nature of the PS energy on the crossline component may help us take advantage of it to improve our PS images. SWS is discussed in more detail in the following section.

10.3 Shear-Wave Splitting (SWS)

Shear-wave splitting (SWS), where shear waves split into two approximately orthogonally-polarised shear waves with different velocities, is characteristic of propagation in media with some form of anisotropy (Crampin, 1981). Figure 10.1 shows the classic schematic illustration of SWS. There are, in general, two types of anisotropy that can result in SWS.

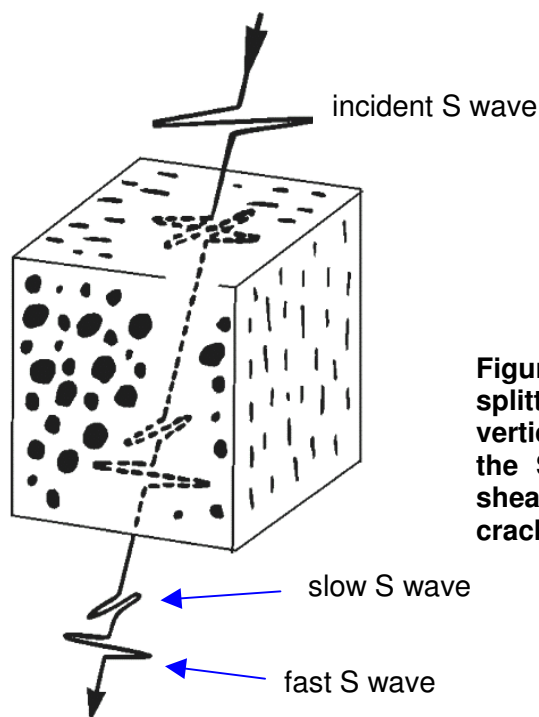


Figure 10.1 Schematic illustration of shear-wave splitting occurring in a rock characterised by near-vertical cracks. For near-vertical propagation of the S wave, the polarisation of the faster split shear wave will be parallel to the strike of the cracks (after Crampin and Chastin (2003)).

Polar anisotropy is related to finely layered sedimentary strata or the alignment of intergranular platelets of mica and other minerals in shales, clays and mudstones. Rocks with polar anisotropy can have vertical and horizontal moveout velocities that differ by up to 30% (Crampin and Chastin, 2003). This can cause severe problems with data processing. Polar anisotropy is the type of anisotropy that the modified CCP-binning algorithm discussed in Section 4.3 would attempt to

accommodate. The only real geological information that can be extracted from the measurement of polar anisotropy is that a rock was laid down in some sort of sedimentary process.

Azimuthal anisotropy is generally related to the presence of near-vertical, aligned fractures and cracks. Below a critical depth (usually 500 – 1000 ms), cracks open normal to the minimum stress, which is typically horizontal – so cracks are usually vertical, striking approximately parallel to the maximum horizontal stress (Crampin and Chastin, 2003). A shear wave propagating below the critical depth will split into a fast S wave with a polarisation approximately parallel to the direction of maximum horizontal stress, and a slower S wave with a polarisation approximately parallel to the direction of minimum horizontal stress. Typically the velocity differential between the fast and slow S waves is 1.5 – 4.5%. If we can determine the polarisation direction of the fast S wave, and measure the time delay between the fast and slow S wave, we can extract information about (a) the dominant fracture direction in the sub-surface, and (b) the density of the fracturing. It is also possible to produce a “fast PS-wave stack” that can show improved temporal resolution compared to the conventional inline PS stack (e.g. Granger *et al.*, 2001).

In the oil and gas industry, where exploration depths are typically well below 500 m, SWS is exploited to help delineate reservoir fracturing. Note however, in order to interpret the results of SWS analysis in terms of fractures, it must be assumed that any observed SWS is due solely to the mechanical anisotropy induced by aligned cracks. The presence of lithological-related (polar) anisotropy and/or strong heterogeneity in the reservoir rock will limit the resolvability of SWS analysis. In addition, as S waves are recorded at the surface, they will suffer phase and amplitude changes that make the recovery of absolute polarisation directions from surface reflection data difficult (Crampin, 1985). Nevertheless, case histories in the oil and gas industry suggest that SWS analysis can be used in conjunction with other structural and stratigraphic information to successfully indicate relative lateral variations in azimuthal anisotropy and provide valuable insights into local geological models (e.g. Granger *et al.*, 2001; Gaiser and Van Dok, 2001).

By analogy, it may be possible to exploit SWS in our 3C coal-seismic data to reveal information about relative changes in sub-surface anisotropy. Note however, we are generally working at depths less than 500 m. In this instance, crack distribution is believed to be controlled more by stress-release and lithological phenomena, and has the potential to be very disturbed (Crampin and Chastin, 2003). We have found no published case studies discussing SWS analysis of shallow surface reflection data. Thus, little is understood about the relevance of information that could be extracted from our 3C seismic data. It is possible that SWS analysis will enable the detection of anomalous zones of fractures that, in turn, could highlight small faults and flexures, and other areas of potential weakness. The following section gives details of a preliminary coal-seismic SWS analysis trial designed to investigate the type of information that we may be able to extract from the integrated interpretation of the two horizontal components of data.

10.4 Real-Data Analysis

Given the highly experimental nature of this SWS analysis trial, we have opted to use the 3C seismic dataset that provides the most obvious example of PS energy on the crossline component. For reasons yet to be understood, data from our commercial 2D-3C mini-SOSIE experiments satisfy this criterion. We are able to include data from these trials here.

Figure 10.2 displays a number of inline- and crossline-component shot records from one of our 3C mini-SOSIE seismic lines (Line C). Typically our crossline component records are similar to the record shown in Figure 10.2(b), where only a very weak trace of PS energy is visible on the crossline data. However, we do get irregular occurrences of significant crossline PS energy, as shown in Figure 10.2(d). Note that, the crossline records in Figure 10.2 also contain significant SS energy related to the surface mini-SOSIE source. However, we are not considering this pure-mode energy at this time.

Figure 10.3 shows the PS-wave sections generated from the inline and crossline components of Line C. The two seismic sections have been produced using exactly the same PS processing flow (Section 4.6). It is apparent from these PS stacks that the crossline component of data only contains coherent PS energy over a very small portion of the seismic line (stations 500 – 650). This seems to correspond with the deepest target coal reflectors. This is likely to be related to the need for a sufficiently thick layer of anisotropic material to exist so that the fast and slow S waves can separate properly. [We therefore cannot assume that anisotropy does not exist along the full length of the line. The remainder of the line may just be too shallow to allow SWS to fully develop.]

We have implemented a two-component rotation / cross-correlation method (Lou *et al.*, 2001) to detect SWS along the small portion of the line that has energy on both the inline and crossline components. As well as requiring that PS energy is consistent on both the inline and crossline components, this SWS analysis method assumes that the fast and slow S waves have a similar waveform. This method can operate on both pre-stack and post-stack data. Here we choose to conduct SWS analysis on the CCP stacks (using the data window marked in Figure 10.3). Recall that, if we can determine the polarisation direction of the fast S wave we can compute the implied fracture orientation along the line (or at least, the dominant orientation of the local anisotropic fabric). A measure of the time delay between the fast and slow S wave is supposed to indicate relative fracture density (or, to be more general, the degree of anisotropy).

Figures 10.4 and 10.5 show the derived fracture orientations and S-wave time delays for the data window under consideration. Ignoring zones of obvious noise contamination, it seems that the dominant fracture orientation can be interpreted as being approximately $\pm 10^\circ$ from the inline direction (52.5° E of N). This is consistent with the fact that dominant thrust structures in the area run perpendicular to the 2D line (i.e. maximum horizontal stress is expected to be approximately parallel to the inline direction). Note that, there are two zones for which implied fracture orientations deviate significantly from this direction – stations 585-590 and stations 612-618. The latter zone is located where a normal fault has been interpreted on the P section, but no structure

has been interpreted on the corresponding PS section. It may be that SWS is the manifestation of this fault in the PS data. The former zone does not correspond to any interpreted structures. It is possible that this zone contains minor faulting that cannot be detected via standard seismic interpretation methods. Attempts to construct a “fast PS-wave stack” using the polarisations in Figure 10.4 did not produce an improved PS image. Interpretation of the time delay curve in Figure 10.5 suggests that the degree of anisotropy varies along the line. Interestingly, the two zones of anomalous fracture orientations marked in Figure 10.4 appear to correspond to reductions in delay times. This implies a relative decrease in the degree of anisotropy which is inconsistent with the interpretation of these anomalies as zones of fracturing / minor faulting. Recall however, that at depths less than 500 m, anisotropy is expected to be strongly influenced by lithology and it may be that S-wave delay times do not behave as expected based on examples from the oil and gas industry. More coal-scale case studies will help clarify the significance of these results.

10.5 Discussion

While PS reflection events are not consistently present on our crossline component of data, we do observe sporadic occurrences of significant PS energy on the crossline component. To the best of our understanding, SWS is responsible for this crossline PS energy. The upwards travelling S wave splits into two, approximately orthogonal polarisations travelling with different velocities, due to the combined effect of polar and azimuthal anisotropy.

Our preliminary real-data investigations have found that our 3C mini-SOSIE data appears to contain more crossline-component PS energy than our dynamite data. It is not clear whether this is a function of the seismic source (and related seismic pulse), or just the geological environment in which the data were acquired. It seems that SWS is only apparent at depths greater than approximately 100 m. An initial attempt to conduct SWS analysis on stacked data has derived average orientation results that are consistent with local geology. This seems to suggest that the polarisation of the fast S wave can be meaningfully interpreted in terms of physical geology. However, further 3C datasets need to be analysed to generalise this conclusion given the uncertainty of crack distribution at depths less than 500 m. Of the two zones of significant variation in our pseudo-fracture orientations, only one corresponds to an interpreted fault. Hence, the ability of SWS to help identify zones of relative change in anisotropy (e.g. fractures associated with minor faulting) is still undetermined. The significance of the corresponding time-delay curve could not be established.

Obviously further work is required to better understand what controls the distribution of PS energy on the crossline components of our 3C seismic datasets. A preliminary attempt at SWS analysis has not invalidated the method for coal-seismic data. Thus, further research on mapping relative changes in anisotropy and extracting crossline PS energy to enhance our converted-wave stacks via SWS analysis is warranted.

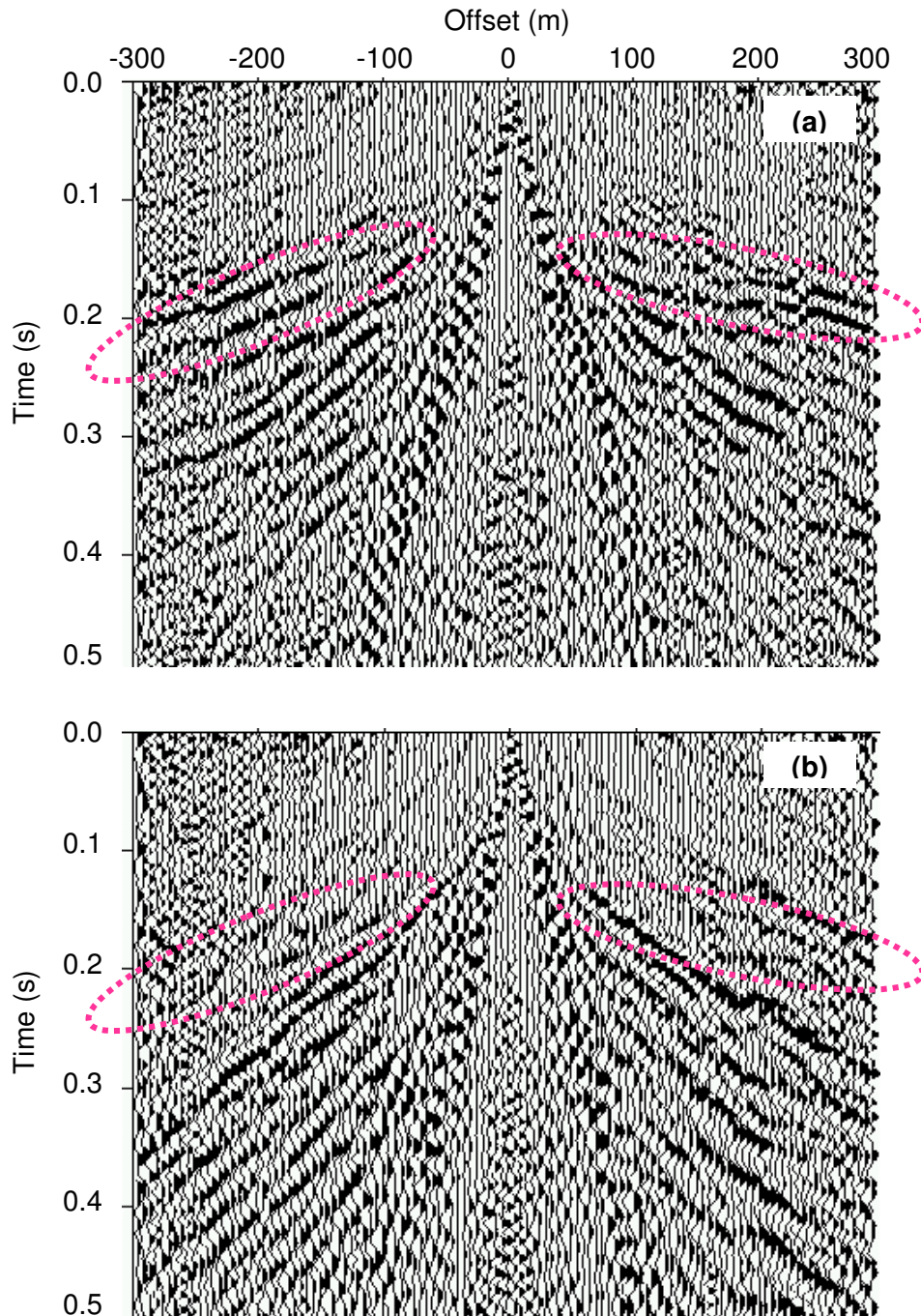


Figure 10.2 (a) Inline component and (b) crossline component of a representative shot record (Shot #430) from one of our 3C mini-SOSIE seismic lines (Line C). PS reflection energy on the inline-component record is highlighted. The corresponding crossline record shows only a very weak trace of PS reflection energy. The strong, coherent energy on the crossline component is SS energy related to the surface mini-SOSIE source. This pure-mode S energy is not being considered at this time.

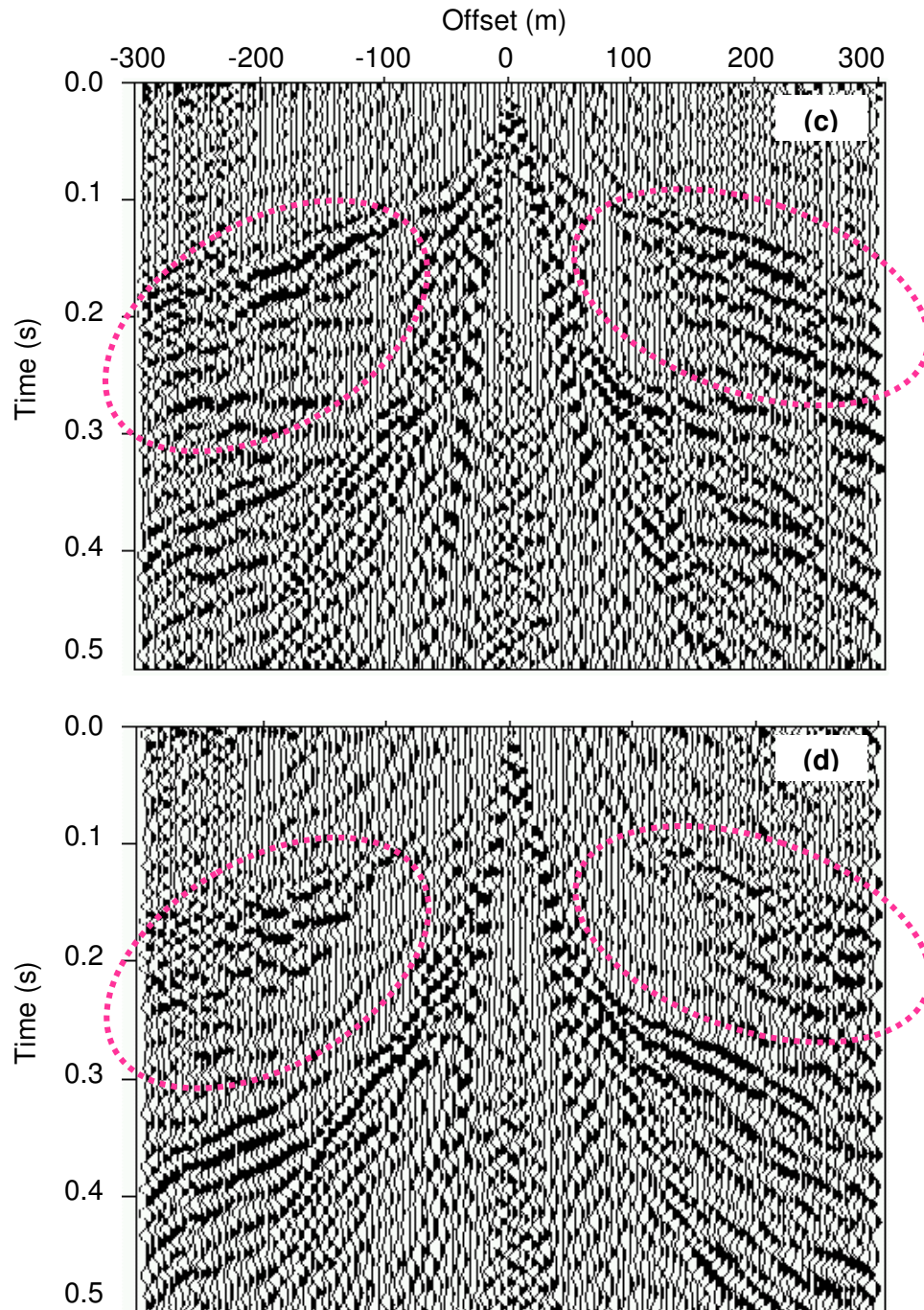


Figure 10.2 (c) Inline component and (d) crossline component of a representative shot record (Shot #590) from one of our 3C mini-SOSIE seismic lines (Line C). PS reflection energy on the inline- and crossline-component records is highlighted. While the PS energy on the crossline component is significant, it still suffers from a poorer signal-to-noise ratio than the corresponding inline PS energy. Note that, the later-arriving coherent energy on the crossline component is SS energy related to the surface mini-SOSIE source. This pure-mode S energy is not being considered at this time.

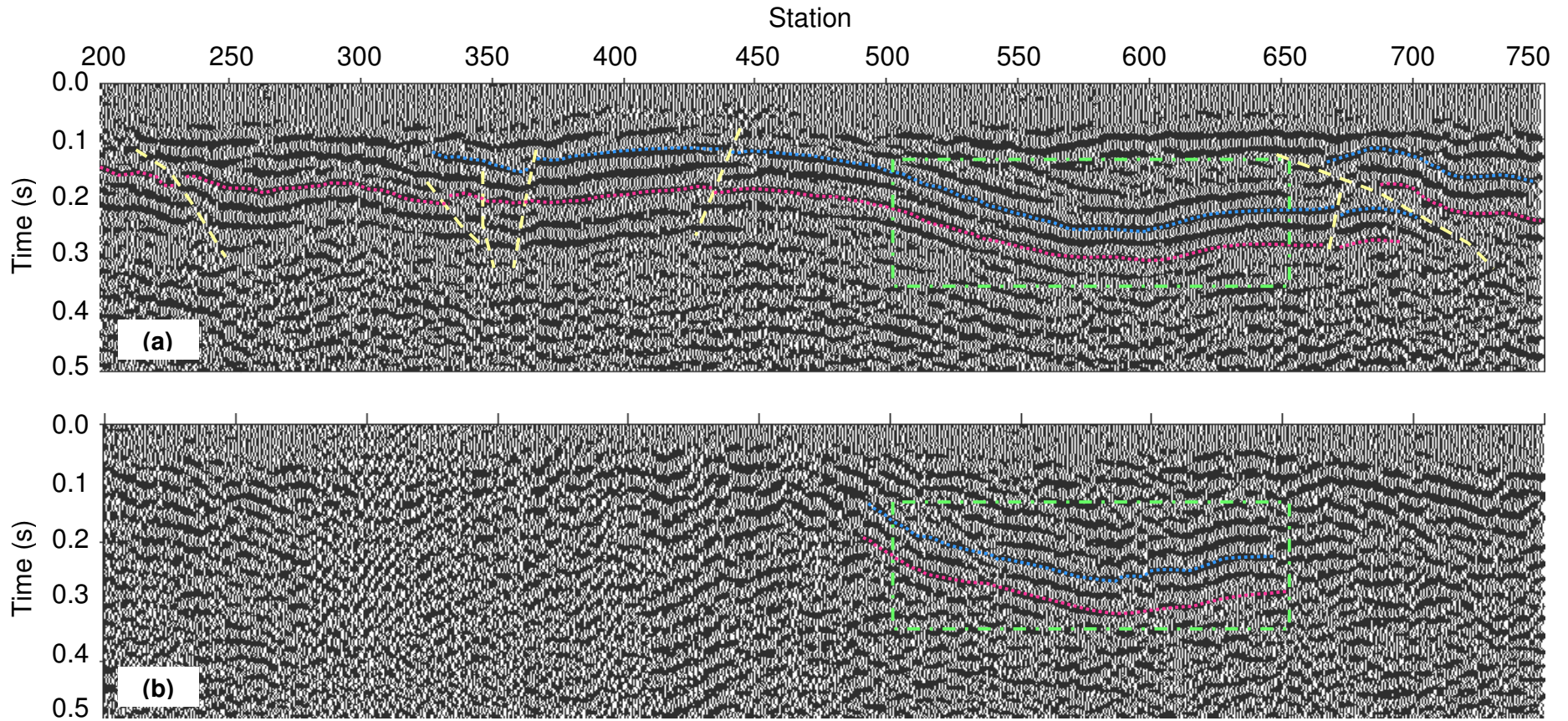


Figure 10.3 PS seismic sections for Line C derived from (a) the inline component and (b) the crossline component of data. Reflection events associated with the two target coal seams are marked. Dashed yellow lines indicate interpreted structure. The green box highlights the zone of significant crossline PS energy (stations 500 – 650). This data window has been used for subsequent shear-wave splitting analysis (see results in Figures 10.4 and 10.5).

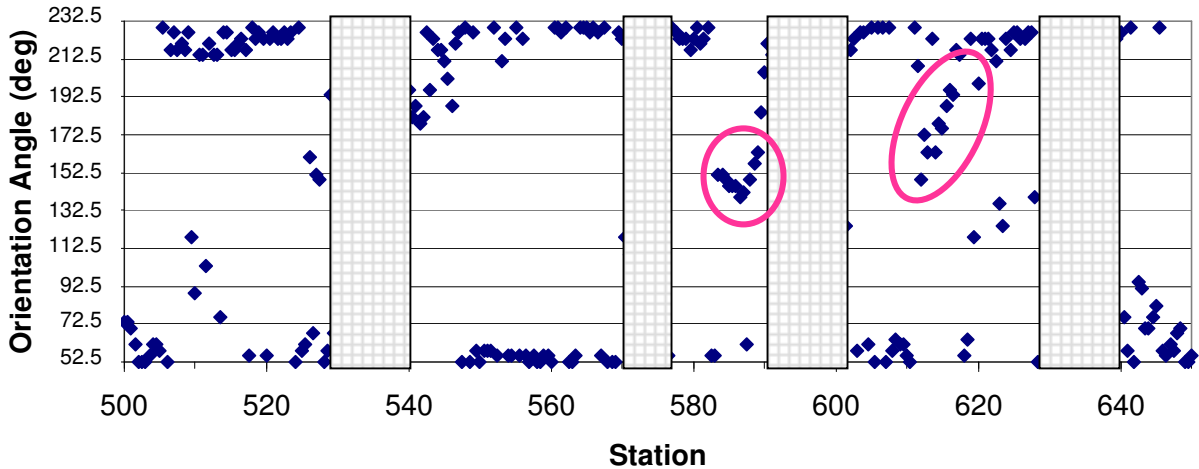


Figure 10.4 Polarisation of the fast S wave computed via integrated processing of the data window marked in Figure 10.3. These polarisations are interpreted in terms of dominant fracture orientation (measured clockwise from North at 0°). Zones of noisy crossline PS data produce spurious results. These have been blocked out by the hatched boxes. The remaining data indicates that the dominant fracture orientation is approximately $\pm 10^\circ$ from the inline direction. Two zones of relatively significant variation in the orientation angles are marked. The zone on the right corresponds to an interpreted fault location.

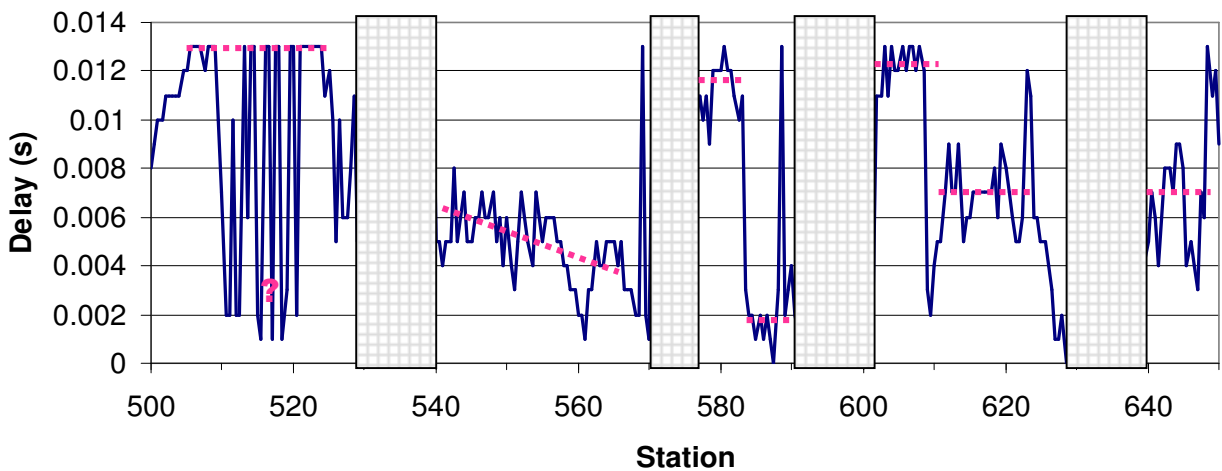


Figure 10.5 Computed traveltme delay between the fast and slow PS waves derived via shear-wave splitting analysis of the data window marked in Figure 10.3. Zones of noisy crossline PS data produce spurious results. These have been blocked out by the hatched boxes. The remaining data indicates that the relative degree of anisotropy varies along the line.

CHAPTER ELEVEN

DISCUSSION AND CONCLUSIONS

11.1 Motivation for this Research

Seismic reflection has become a vital exploration tool for underground coal-mining operations. A total of approximately 45 3D seismic surveys have been acquired in the Bowen and Sydney Basins since 1997. Many more 2D coal-seismic surveys add to the volumes of seismic data that are helping reduce exploration costs, delineate geological structures, improve mine productivity and create safer workplaces in the Australian coal industry.

Ongoing research into coal-seismic exploration is driven by the desire to locate and characterise increasingly subtle structures, and extract more lithological detail using seismic data. Over the past five years Velseis Pty Ltd has contributed to the evolution of coal-seismic imaging through its research and development of converted-wave seismic technologies. The motivation for utilising converted-wave seismic exploration is largely provided by the success of multi-component seismic experiments in the petroleum sector. In terms of petroleum scale-exploration, PS images have provided the opportunity to independently validate structural interpretation results and yield predictions of lithology, porosity, fracturing and the presence of fluids. By analogy, multi-component seismic methods in the coal environment have the potential to enhance the delineation of structural features, highlight zones of potential weakness/fracturing, and map lithology away from borehole locations.

ACARP Project C10020 (completed June 2003) successfully developed converted-wave seismic acquisition and processing methodologies appropriate for the coal environment, and demonstrated the feasibility of producing structural images of target coal seams using PS data.

The current project has focused on the advancement of PS imaging technologies to improve our converted-wave seismic sections, and the design and implementation of integrated P/PS processing and interpretation tools to extract lithological information from multi-component coal-seismic data. The key outcomes of this research, together with recommendations for future research and development into converted-wave seismic technologies, are presented in the following sections.

11.2 Summary of Conclusions

Acquisition

Strong PS energy can be recovered below 40 Hz if low-frequency energy is allowed to be captured by the recording system. This low-frequency PS signal can help reduce the 'ringiness' of reflection events in PS sections that don't contain significant PS signal above 50 – 60 Hz. Thus, geophones with a low natural frequency (e.g. 10 Hz or 14 Hz) are believed to be more suitable than geophones with a natural frequency of 40 Hz for acquiring 3C coal-seismic data in the future.

Processing

PS images derived for Trial #2 and Line C confirm that modifications to our S-wave statics method, CCP-binning algorithm and post-stack noise removal techniques have significantly improved the outcomes of our converted-wave imaging. However, results from Trials #2 and #3 indicate that we are losing considerable high-frequency PS information during the PS stacking process. There is evidence to suggest that S-wave receiver statics are not the most critical factor controlling this loss of resolution in the PS sections. Investigations into PS-wave behaviour suggest that high-frequency PS information might be better maintained if anisotropy is accommodated in the PS processing flow.

Vector processing, designed to extract pure S energy from the inline- and vertical-component records, has enhanced the PS image for Trial #1. However, this experiment did not incorporate our most recent advances in PS processing methodology. Therefore, the necessity of including vector processing routinely in the PS processing flow is still under consideration.

Interpretation

The diodic behaviour of the positive- and negative-offset PS stacks for Trials #2 and #3 has highlighted the presence of anomalous sandstone units not detected by the corresponding P-wave data. These case studies suggests that, in situations where significant lateral heterogeneities are expected, consideration of the un-migrated positive- and negative-offset PS sections might positively contribute to the interpretation results.

The recovery of absolute V_p/V_s values (or equivalently Poisson's Ratio) is unlikely in the coal environment. However, synthetic data trials have demonstrated that, provided the width of a geological anomaly is greater than the lateral resolution limit of the seismic data, and the lithological variation is significant, the V_p/V_s attribute can give an indication of relative changes in lithology. To avoid spurious V_p/V_s values associated with processing artefacts, seismic noise and structure, we recommend that real-data V_p/V_s analysis should only use well-defined seismic reflection events and smoothed two-way time (TWT) picks. In addition, practical V_p/V_s analysis cannot place significance in amplitude variations about structures or on very small amplitude variations in the V_p/V_s curves. V_p/V_s interpretation results from Trials #2 and #3 are mixed, but don't entirely negate the proposition that integrated P/PS processing could identify broad zones of significant lithological variation. However, V_p/V_s analysis will certainly not have the ability to remotely acquire high-resolution geological detail about the roof and floor of a coal seam.

Irregular occurrences of PS energy in our crossline-component data are believed to be the result of shear-wave splitting (SWS). A preliminary test to quantify this behaviour along Line C suggests that fast S-wave polarisations can be interpreted in terms of local stress fields (i.e. direction of maximum horizontal stress derived from seismic data via SWS analysis is approximately perpendicular to strike of thrust faults in area). Attempts to correlate deviations in these derived fast S-wave polarisation measurements with local structures are yet to be validated. To date, no useful information has been extracted from the corresponding S travel-time delay curve.

11.3 Future Research and Development

Acquisition

Typically, for older 10 Hz or 14 Hz geophones, only frequencies up to approximately 150 – 180 Hz will be reliably measured. Thus, using 3C geophones with a 10 Hz natural frequency should have no impact on the higher P-wave frequencies typically acquired using a mini-SOSIE source. However, there is the potential that the higher P-wave frequencies of a dynamite survey could be compromised. This needs to be fully investigated before future 3C coal-seismic surveys are routinely acquired using geophones with a lower natural frequency. It may be necessary to consider using geophone elements especially designed to accommodate a broader frequency bandwidth when recording dynamite 3C coal-seismic data.

Processing

PS waves are extremely sensitive to inhomogeneities in the earth. This manifests itself as differences in PS wave behaviour as a function of direction of travel. To improve compensation for this diodic behaviour during PS data processing, a CCP-binning scheme that accommodates anisotropy and post-stack PS migration are required. The implementation of these two processing procedures is seen as a priority for helping to improve the resolution and structural integrity of our PS seismic sections.

Vector processing uses wavefield particle motion, together with frequency and slowness information, to separate different wave types. To date, our vector processing experiments have been designed to extract P and S energy. Vector processing can also be designed to extract dominant noise wavefields from 3C data records. This may be relevant in terms of removing significant groundroll energy from our 3C seismic data if geophones with a lower natural frequency continue to be used. P and PS stacks following vector processing need to be assessed (subsequent to any further PS processing development) to determine whether or not vector processing should be considered an integral part of the P and/or PS processing flow.

Ultimately, it is expected that converted-wave technology will be exploited as an enhancement to 3D coal-seismic surveys. 3D converted-wave acquisition will necessarily require some adjustments to the field logistics developed for the 2D trials undertaken so far. Most significantly, 3D multi-component data will require a number of modifications to the processing procedures established throughout our research to date. It is expected that significant effort will be required to adapt processing algorithms in order to derive a 3D PS stacked seismic volume.

Interpretation

To date, little validation of structural information recovered from PS data has been undertaken. A structure on a PS image is generally considered 'probable' if it coincides with a structure on the corresponding P section. However, there are situations where a 'fault' is clearly imaged in the PS section but not the P section – even when the PS data exhibit overall poorer resolution. An example of this is seen with the Trial #2 results. Further investigation is required to ascertain the reliability of these types of anomalies – do they actually represent structures, other geological

features that effect only S waves, or are they processing artefacts? Proactive validation will improve future interpretation of PS data.

This project presents the first attempts to map lithology away from boreholes in the coal environment using integrated P/PS interpretation methodologies adapted from the petroleum sector. These initial trials give mixed results. Additional field trials will help generalise conclusions about the relevance and resolution of information that can be extracted via V_p/V_s analysis, and will help streamline practical interpretation procedures. The usefulness of this type of information for mine-site applications needs to be assessed. Note that, ideally, the outcomes of V_p/V_s interpretation should be re-visited subsequent to the successful implementation of the PS processing developments recommended above.

Our current understanding is that PS energy on the crossline components of our 3C seismic datasets results from anisotropy in the sub-surface. However, it is still not clear what the primary control factors are for the irregular distribution of the crossline PS energy (e.g. variations in vertical stress-aligned fractures, local structures, lithology etc). Efforts to further understand the underlying cause of our crossline PS energy, and ongoing investigation into methods that can use the crossline PS energy to extract relevant information about these physical control factors, will contribute to the geological information we derive via integrated processing of the two horizontal components of data. Note also, that alternative ways to take advantage of crossline PS energy in order to enhance the signal-to-noise ratio of target reflectors in the final PS image should be explored.

11.4 Conclusions

The overall outcomes of this project have been to enhance PS processing, obtain a greater understanding of the influence of geology on PS-wave propagation, and determine to what extent integrated P/PS interpretation can contribute to our geological knowledge of the sub-surface. Prior to this study, only the viability of extracting structural information about the target coal seam from PS data had been tested. The results achieved in this project clearly demonstrate that joint use of the P and PS sections recovers more geological detail about the sub-surface than using P-wave data alone. It remains to be determined how useful this additional lithological information will be to mine-site operations.

The continued development of a robust and cost-effective PS processing methodology is seen as the key to the future use of converted-wave seismic in the coal environment. Corresponding enhancements to the PS sections are expected to yield more robust and higher-resolution structural and lithological information. Such research may see an even greater amount of geological detail extracted from coal-seismic data than has been achieved to date, and will most certainly help continue the transfer of converted-wave seismic technologies away from purely experimental work to more production seismic-imaging projects.

REFERENCES

- Cary, P.W., and Eaton, D.W.S., 1993. A simple method for resolving large converted-wave (P-SV) statics: *Geophysics* **58**, 429-433.
- Cerjan, C., Kosloff, D., Kosloff, R., and Reshef, M., 1985. A nonreflecting boundary condition for discrete acoustic and elastic wave equations: *Geophysics* **50**, 705-708.
- Crampin, S., 1981. A review of wave motion in anisotropic and cracked elastic-media: *Wave Motion* **3**, 343-391.
- Crampin, S., 1985. Evaluation of anisotropy by shear-wave splitting: *Geophysics* **50**, 142-152.
- Crampin, S., and Chastin, S., 2003. A review of shear wave splitting in the crack-critical crust: *Geophysical Journal International* **155**, 221-240.
- Cohen, J.K., and Stockwell, Jr. J.W., 2002. CWP/SU Seismic Unix Release 36 – a free package for seismic research and processing: Centre for Wave Phenomena, Colorado School of Mines.
- DeAngelo, M.V., Backus, M., Hardage, B.A., Murray, P., and Knapp, S., 2003. Depth registration of P-wave and C-wave seismic data for shallow marine sediment characterisation, Gulf of Mexico: *The Leading Edge* **22**, 96-105.
- Domenico, S.N., 1984. Rock lithology and porosity determination from shear and compressional wave velocities: *Geophysics* **49**, 1188-1195.
- Freire, S.L.M., and Ulrych, T.J., 1988. Application of singular value decomposition to vertical seismic profiling: *Geophysics* **53**, 778-785.
- Gaiser, J., and Van Dok, R., 2001. Green River basin 3-D/3-C case study for fracture characterisation: Analysis of PS-wave birefringence: SEG 71st Ann. Int. Mtg., Expanded Abstracts.
- Granger, P-Y., Bonnot, J-M, Gresillaud, A., and Rollet, A., 2001. C-wave resolution enhancement through birefringence compensation at the Valhall Field: SEG 71st Ann. Int. Mtg., Expanded Abstracts.
- Granli, J.R., Arnsten, B., Sollid, A., and Hilde, E., 1999. Imaging through gas-filled sediments using marine shear-wave data: *Geophysics* **64**, 668-677.
- Grant, F.S., and West, G.F., 1965. *Interpretation Theory in Applied Geophysics*: McGraw-Hill Book Company, Sydney.
- Hendrick, N., 2001. Integration and Demonstration of Parametric Techniques for Multi-Component Seismic Wavefield Separation: PhD, The University of Queensland.

Hendrick, N., and Brand, E., 2006. Practical evaluation of P- and S-wave separation via elastic wavefield decomposition: *Exploration Geophysics* **37**, 339-350.

Levander, A.R., 1988. Fourth-order finite-difference P-SV seismograms: *Geophysics* **53**, 1425-1436.

Li, X-Y, MacBeth, C., Hitchen, K., and Hanßen, P., 1998. Using converted shear-waves for imaging beneath basalt in deep water plays: SEG 68th Ann. Int. Mtg., Expanded Abstracts.

Li, X-Y, Dai, H., Mueller, M.C., and Barkved, O.I., 2001. Compensating for the effects of gas clouds on C-wave imaging: A case study from Valhall: *The Leading Edge* **20**, 1022-1028.

Lou, M., Zhang, Y., and Don Pham, L., 2001. Shear-wave splitting and fracture orientation analysis from PS waves – examples from synthetic and field OBC data: SEG 71st Ann. Int. Mtg., Expanded Abstracts.

Mittet, R., 2002. Free-surface boundary conditions for elastic staggered-grid modelling schemes: *Geophysics* **67**, 1616-1623.

Sheriff, R.W., 1991. *Encyclopedic Dictionary of Exploration Geophysics*, Society of Exploration Geophysicists, Oklahoma, USA.

Stewart, R.R., 2003. *Converted-Wave Seismic Exploration: Methods & Applications: Short Course*, ASEG 16th Geophysical Conference & Exhibition, Adelaide, Australia.

Sun, R., 1999. Separating P- and S-waves in prestack 2-dimensional elastic seismograms: 61st Conference and Technical Exhibition, EAGE, Extended Abstracts, #6-23.

Sun, R., and McMechan, G.A., 1986. Prestack reverse-time migration for elastic waves with application to synthetic offset vertical seismic profiles: *Proceedings of the IEEE* **74**, 457-465.

Sun, R., Chow, J., and Chen, K-J., 2001. Phase correction in separating P- and S-waves in elastic data: *Geophysics* **66**, 1515-1518.

Sun, R., McMechan, G.A., Hsiao, H-H., and Chow, J., 2004. Separating P- and S-waves in prestack 3D elastic seismograms using divergence and curl: *Geophysics* **69**, 286-297.

Tatham, R.H., 1982. V_p/V_s and lithology: *Geophysics* **47**, 336-344.

Thomsen, L., 1999. Converted-wave reflection seismology over inhomogeneous, anisotropic media: *Geophysics* **64**, 678-690.

Thomsen, L., 2002. Understanding Seismic Anisotropy in Exploration and Exploitation: SEG/EAGE Distinguished Instructor Short Course #5, Society of Exploration Geophysicists, Oklahoma, USA.

Velseis, 2003. Investigation of converted-wave seismic reflection for improved resolution of coal structures: Final Report: Australian Coal Association Research Program (ACARP) Project C10020.

Virieux, J., 1986. P-SV wave propagation in heterogeneous media: velocity-stress finite-difference method: *Geophysics* **51**, 889-901.

Yilmaz, O., 1987. *Seismic Data Processing*: Society of Exploration Geophysicists, Oklahoma, USA.

Zhang, Y., 1996. Nonhyperbolic converted-wave velocity analysis and normal moveout: SEG 66th Ann. Int. Mtg., Expanded Abstracts, 1555-1558.

Zhe, J., and Greenhalgh, S.A., 1997. Prestack multicomponent migration: *Geophysics* **62**, 598-613.

GLOSSARY

This glossary contains explanations of technical terms and acronyms commonly used to describe multi-component seismic processing and interpretation. More comprehensive explanations can be found in standard seismic texts and reference books (e.g. Sheriff, R.E. (1991) Encyclopedic Dictionary of Exploration Geophysics, Society of Exploration Geophysicists, Oklahoma).

2D	two-dimensional
3D	three-dimensional
3C	three-component; typically refers to the vertical and two orthogonal horizontal components of ground motion recorded by a 3C geophone
AGC	automatic gain control; data dependent scaling designed to normalise trace amplitude within a running time window
anisotropy	variation of seismic velocity depending on the direction in which it is measured; a sequence of sedimentary bedding produces polar anisotropy (where seismic velocities are symmetric about axis perpendicular to the bedding); non-horizontal fracturing and microcracks produces azimuthal anisotropy (where seismic velocities are symmetric about the axis perpendicular to the fracturing)
angle of incidence	the angle (with respect to the vertical axis) at which seismic energy arrives at a geological boundary
bandpass filter	attenuation of seismic energy outside of a user-defined frequency bandwidth
binning	the process by which all traces sharing the same sub-surface reflection point are grouped together; typically referred to as CMP binning for conventional P data, and CCP binning for PS data
CCP stacking	the summation of all traces within a CCP gather
CMP stacking	the summation of all traces within a CMP gather
common conversion point (CCP) gather	a collection of (usually horizontal component) seismic traces sharing the same sub-surface P-to-S conversion point; the location of the wavefield conversion point is a function of V_p/V_s and the depth of the boundary at which the conversion occurs
common midpoint (CMP) gather	the set of (usually vertical component) seismic traces that share the same midpoint between their sources and receivers
common receiver gather (CRG)	a collection of seismic traces recorded at the same geophone (receiver) location, generated by sources at a variety of locations
converted waves	seismic waves that travel down to a geological boundary as a P wave, get partially converted to S energy at the boundary, and then travel back to the surface as an S wave; also referred to as PS waves

CRG stack	the resultant seismic section produced by summing all traces within each CRG, and displaying the summed traces in receiver-location order
crossline component	seismic energy recorded using a geophone that measures the horizontal component of ground motion perpendicular to the line of recording
dominant frequency	the predominant frequency of a seismic dataset determined by measuring the time between successive peaks or troughs of the recorded seismic pulse, and taking the reciprocal
dominant wavelength	the seismic wavelength associated with the dominant frequency; for P waves, equivalent to V_p divided by the dominant frequency; for S waves a more complicated expression involving both V_p and V_s , and P- and S-wave dominant frequencies is required
Fresnel zone	in reality, seismic energy is reflected from a zone on a geological boundary – within this zone any two or more reflecting points are considered indistinguishable from the earth's surface; this circular zone is called the Fresnel zone, the radius of which is defined as approximately equal to $\sqrt{(z\lambda)/2}$, where z is the depth of the reflector, $\lambda = v/f_D$ is the dominant wavelength of the data, v is the average seismic velocity, and f_D is the dominant frequency of the seismic signal.
frequency	the repetition rate of a periodic waveform, measured in 'per second' or Hertz (Hz)
frequency bandwidth	range of frequencies over which the recorded seismic signal has maximum power
geophone	the recording device or receiver used to transform seismic energy into an electrical voltage for input into the seismic recording system; a single vertically-oriented geophone is used for conventional seismic acquisition; three mutually orthogonal geophones are used when recording 3C data
geophone array	see receiver array
groundroll	a type of seismic wave that travels along or near the surface of the ground; characterised by relatively low velocity, low frequency and high amplitude; seen as a steeply dipping, linear event on a seismic shot record
inline component	seismic energy recorded using a geophone that measures the horizontal component of ground motion parallel to the line of recording
lithological interpretation	used here to describe efforts to extract more detailed geological character in terms of lithology, fluids and fractures etc
magnitude spectrum	amplitude of seismic recording as a function of frequency
multi-component acquisition polarity standard	right-handed coordinate system where z (vertical direction) is positive downward; x (inline direction) is positive in the forward line direction for a 2D survey; and y (crossline direction) is positive in the direction 90° clockwise from x .
multi-component recording	seismic recording that measures both the vertical and horizontal components of ground motion at the receiver; also referred to as 3-C recording

mute	elimination of unwanted energy from seismic traces; typically used over certain time intervals to remove groundroll or noise bursts out of the final stack
normal moveout (NMO)	the variation of the arrival time of reflection energy with offset; NMO corrections compensate for this variation in travelttime so that reflection energy from each geological boundary is properly aligned prior to stacking; for horizontal reflectors, P-wave NMO can be described as hyperbolic; the NMO for PS-waves is always non-hyperbolic
octave	the interval between two frequencies having a ratio of 2
offset	the distance from the source point to the receiver location
P waves	longitudinal or compressional seismic waves; characterised by particle motion in the direction of travel; acquired using conventional (single-component) seismic acquisition surveys
receiver array	a group of geophones planted in a linear or areal pattern connected to a single recording channel; generally used to attenuate unwanted surface-wave noise and boost the signal-to-noise ratio
residual static corrections	corrective time shifts applied to the data to compensate for remnant statics associated with incomplete weathering static corrections
resolution	the ability to separate two features which are very close together
resolution limit	for discrete seismic reflectors, the minimum separation so that one can ascertain that more than one interface is involved; the commonly used Rayleigh resolution limit is defined as one quarter the dominant wavelength; the Widess limit is defined as one eighth the dominant wavelength
S waves	transverse or shear seismic waves; characterised by particle motion perpendicular to the direction of travel; acquired using multi-component (3C) seismic acquisition
seismic waves	sound waves that propagate through the earth
seismic modelling	generation of a synthetic seismic record given an earth model
seismic reflection	a geophysical method to image the sub-surface using artificially-generated sound waves; typically the arrival times of various seismic waves are used to map sub-surface structure
seismic source	an artificial device that releases energy or seismic waves into the ground; typical coal-seismic sources include small dynamite explosions, mini-SOSIE and Vibroseis
seismic velocity	the propagation rate of a seismic wave through a particular material
shot record	a collection of seismic traces recorded from the release of seismic energy at a single source location

signal-to-noise ratio (S/N)	the ratio of desired signal to all other recorded energy (noise) in a seismic recording; difficult to determine in practice
single-component recording	conventional seismic acquisition that records only the vertical component of ground motion at the receiver
spherical divergence correction	a scaling correction to compensate for decrease in wave strength with distance as a result of geometric spreading
stacking	process by which a set of seismic traces are summed
static corrections	corrective time shifts applied to seismic data to compensate for the effects of variations in elevation, weathering thickness, weathering velocity or reference to datum; the objective is to determine the arrival times which would have been observed if all measurements had been made on a flat plane with no weathering or low-velocity material present
structural interpretation	involves the mapping of geological interfaces and discontinuities (such as faults)
surface waves	see groundroll
trim statics	corrective time shifts applied to NMO-corrected CMP or CCP gathers prior to stacking; designed to optimally align flattened reflection events
TWT	two-way travelttime; refers to the time it takes for seismic energy to travel from the seismic source, down to a reflector, and back to the surface receiver
vector processing	simultaneous use of two or more components of multi-component seismic data to separate P and S energy
velocity analysis	calculation of a velocity that will accurately compensate for the effects of NMO; typically involves flattening reflection events in a CMP or CCP gather
vertical component	the seismic energy recorded using a geophone that measures the vertical component of ground motion
V_p	P-wave seismic velocity
V_s	S-wave seismic velocity
V_p/V_s	ratio of P-wave to S-wave seismic velocity; directly related to Poisson's Ratio
wavelength	the distance (in metres) between two successive similar points on two adjacent cycles of a seismic wave, measured perpendicular to the wave front; often represented by the symbol λ

APPENDIX A

S-WAVE RECEIVER STATIC CORRECTIONS

Near-surface lateral velocity variations and topographical changes cause time anomalies in seismic reflection events that can be approximated as surface-consistent static time shifts. Consider a particular trace at source = i , receiver = j , ccp = k , and offset = l . The total static time shift of this trace, δt_{ijkl} , can be described by the surface-consistent model:

$$\delta t_{ijkl} = \delta t_i + \delta t_j + \delta t_k + \delta t_l, \quad (\text{A-1})$$

where δt_i is the time anomaly associated with the near-surface at the source, δt_j is the time anomaly associated with the near-surface at the receiver, δt_k is the time anomaly associated with the CCP (i.e. a time anomaly associated with structure along the line), and δt_l is the time anomaly associated with the offset (i.e. a time anomaly associated with the normal-moveout of the reflection event).

Equation (A-1) can be re-written in matrix form as:

$$\mathbf{t} = \mathbf{A} \mathbf{s}, \text{ or} \quad \begin{pmatrix} \delta t_{1111} \\ \delta t_{2111} \\ \vdots \\ \delta t_{1211} \\ \vdots \\ \delta t_{2311} \\ \vdots \end{pmatrix} = \begin{pmatrix} 1 & 0 & 0 & 0 & \cdots & 1 & 0 & 0 & 0 & \cdots & 1 & 0 & 0 & 0 & \cdots & 1 & 0 & 0 & 0 & \cdots \\ 0 & 1 & 0 & 0 & \cdots & 1 & 0 & 0 & 0 & \cdots & 1 & 0 & 0 & 0 & \cdots & 1 & 0 & 0 & 0 & \cdots \\ \vdots & \vdots \\ 1 & 0 & 0 & 0 & \cdots & 0 & 1 & 0 & 0 & \cdots & 1 & 0 & 0 & 0 & \cdots & 1 & 0 & 0 & 0 & \cdots \\ \vdots & \vdots \\ 0 & 1 & 0 & 0 & \cdots & 0 & 0 & 1 & 0 & \cdots & 1 & 0 & 0 & 0 & \cdots & 1 & 0 & 0 & 0 & \cdots \\ \vdots & \vdots \end{pmatrix} \cdot \begin{pmatrix} \delta t_{S1} \\ \delta t_{S2} \\ \delta t_{S3} \\ \vdots \\ \delta t_{R1} \\ \delta t_{R2} \\ \delta t_{R3} \\ \vdots \\ \delta t_{C1} \\ \delta t_{C2} \\ \delta t_{C3} \\ \vdots \\ \delta t_{O1} \\ \delta t_{O2} \\ \delta t_{O3} \\ \vdots \end{pmatrix}. \quad (\text{A-2})$$

Here, \mathbf{t} is the vector of total observed time shifts for each trace in the seismic dataset, and \mathbf{s} is the vector of static shifts associated with individual sources, receivers, CCPs and offsets. Provided the above set of linear equations is over-determined (i.e. there are more known variables than unknown), the individual timing anomalies associated with the sources, receivers, CCPs and offsets can be solved for in a least-squares sense. In practice, singular value decomposition (SVD) is used to solve for the unknown vector \mathbf{s} in equation (A-2). (Care must be taken to ensure the system of equations is over-determined since SVD will still yield a solution for an under-determined set of equations that may or may not be physically meaningful.) Note that, in the case of computing S-wave receiver static corrections for converted-wave seismic data, we assume that

$\delta t_{S1} = \delta t_{S2} = \dots = \delta t_{SN} = 0$ (i.e. $\delta t_i = 0$ for all sources), since the P-wave source static corrections can be computed independently from the P-wave data and applied prior to computing the S-wave receiver statics. This reduces the number of unknowns in equation (A-2), and hence reduces the non-uniqueness of the solution. Any variations in the observed time shifts associated with structure and normal moveout (and error in the source static corrections) will dominate the δt_k and δt_i terms when we solve equation A-2. The desired S-wave receiver static correction is derived from the recovered receiver term δt_j .

In practice, our S-wave statics method determines the observed time shifts for each trace by picking the two-way traveltime (TWT) for a selected PS reflection event on every possible trace on every common-offset receiver section, and computing the difference between this TWT and some reference time. This approach to measuring δt_{ijkl} takes advantage of the fact that we expect very strong P-to-S conversion from the top of a coal seam, and can therefore consistently identify PS reflection events on raw common-offset receiver sections.

The benefits of this S-wave receiver statics method over our original statics method include:

- (a) the ability to handle the effect of structure and dip on the PS reflection events, and
- (b) the ability to avoid the time-consuming and ambiguous task of V_p/V_s analysis on common-receiver gathers (CRGs).

We believe the S-wave receiver static corrections computed via this new approach are more accurate and reliable than those derived from our original statics method. Note however, this statics approach will perform poorly across zones of very poor data quality if the observed TWT picks are inconsistent. In this instance, stacking of adjacent offset sections may help. If no reliable solution for the receiver static can be computed, we set $\delta t_j = 0$ for all relevant receivers, and rely on CCP trim statics to correct for any time shifts associated with the near-surface.

APPENDIX B CCP BINNING

The following pseudo-code summarises the practical implementation of our modified common-conversion point (CCP) binning algorithm.

```
READ: Inline shot records
READ:  $V_p/V_s$  function
READ:  $V_p$  function
LOOP: CCP
  Interpolate  $V_p$  and  $V_p/V_s$  for this CCP
  Compute minimum  $V_p/V_s$  for this CCP
  LOOP: all traces
    Compute asymptotic approximation of CCP location (ACCPX) for this trace
    using minimum  $V_p/V_s$ 
    IF (current CCPX lies between ACCPX of trace and receiver location of trace) THEN
      {this trace can contribute to current CCP}
      LOOP: time samples
        Compute SAMPLE_CCPX for current sample
        IF (SAMPLE_CCPX lies within current CCP bin) THEN
          Stack sample into current CCP gather
        ENDIF
      END: time sample loop
    ENDIF
  END: trace loop
END: CCP loop
Normalise stacked CCP gather traces
OUTPUT: CCP gathers
```

APPENDIX C

POST-STACK EIGENVECTOR FILTERING

Let \mathbf{D} be the $N \times M$ matrix of stacked seismic data comprising M traces and N samples per trace. The singular value decomposition (SVD) of \mathbf{D} is given by:

$$\mathbf{D} = \mathbf{U}\mathbf{\Sigma}\mathbf{V}^T = \sum_{i=1}^M \sigma_i \mathbf{u}_i \mathbf{v}_i^T, \quad (\text{C-1})$$

where \mathbf{U} and \mathbf{V} are the left and right eigenvector matrices, respectively, and $\mathbf{\Sigma}$ is the matrix of singular values. In the summation representation, the σ_i are the individual singular values, generally ordered so that $\sigma_1 > \sigma_2 > \dots > \sigma_M$.

In equation (C-1) the factor $\mathbf{u}_i \mathbf{v}_i^T$ is an $N \times M$ matrix of unitary rank which is called the i^{th} eigenimage of \mathbf{D} . Owing to the orthogonality of the eigenvectors \mathbf{v}_i , the eigenimages form an orthogonal basis for the representation of \mathbf{D} . Clearly, the contribution of a particular eigenimage in the reconstruction of \mathbf{D} is proportional to the magnitude of the associated singular value.

In the event that all M traces of the stacked data are linearly independent (i.e. no trace may be represented in terms of a linear combination of the other $M-1$ traces), \mathbf{D} is of full rank M , and all the singular values are non-zero. In this case, the perfect reconstruction of \mathbf{D} requires all eigenimages. On the other hand, in the case where all M traces are equal to within a scale factor, all traces are linearly dependent, and \mathbf{D} is of rank one. \mathbf{D} can then be perfectly represented by the first eigenimage $\sigma_1 \mathbf{u}_1 \mathbf{v}_1^T$. In the general case, \mathbf{D} may be reconstructed using the first 10% or so of eigenimages (i.e. the most dominant eigenimages). This will recover data with the maximum trace-to-trace coherence. Random noise is dispersed equally amongst all of the eigenimages. Hence, keeping only the most dominant eigenimages will attenuate noise with respect to desired signal (see Freire and Ulrych (1988) for further details).

APPENDIX D

ELASTIC WAVEFIELD DECOMPOSITION

Typically, a P-wave image is produced via scalar processing of the vertical component of data, and the corresponding PS image is obtained from scalar processing of the horizontal component(s). This conventional component-selection approach to processing multi-component data however, ignores the potential cross-contamination of P-wave energy on to the horizontal components and S-wave energy on to the vertical component. Basic ray-parameter concepts dictate that such cross-contamination is likely to be observed on far-offset traces, particularly in areas with relatively high-velocity surface layers (e.g. areas with surface basalts).

True vector-processing techniques take advantage of the actual wavefield particle motion to distinguish between wave types, and have the potential to produce cleaner P- and S-wave records in areas prone to significant wavefield cross-contamination. One such method, here referred to as Elastic Wavefield Decomposition (EWD), has received some attention in recent geophysical literature (e.g. Sun *et al*, 200; Sun *et al*, 2004). However, to date no real-data examples demonstrating P/S separation via EWD have been described. We believe the application of EWD to Trial Dataset #1 (Chapter 5) is the first published real-data example of the vector-processing method.

The theoretical formulation of EWD uses the equation of motion that describes the propagation of stresses through a medium:

$$\rho \frac{\partial^2 \mathbf{u}}{\partial t^2} = (\lambda + \mu) \nabla \theta + \mu \nabla^2 \mathbf{u} , \quad (\text{D-1})$$

where $\mathbf{u} = (u_x, u_z)$ is the vector of horizontal and vertical displacements recorded over time (t) in the two-dimensional plane defined by the horizontal and vertical spatial coordinates x and z , $\theta = \nabla \cdot \mathbf{u}$ is dilatation, ρ is density, and μ and λ are the Lamé constants (e.g., Grant and West, 1965).

Application of the divergence and curl operators to equation (D-1) yields separate equations for the propagation of P- and S-waves, respectively. In these equations the propagating entities are the dilatation:

$$\theta = \nabla \cdot \mathbf{u} = \frac{\partial u_x}{\partial x} + \frac{\partial u_z}{\partial z} , \quad (\text{D-2})$$

and rotation:

$$\varphi = \nabla \times \mathbf{u} = \frac{\partial u_x}{\partial z} - \frac{\partial u_z}{\partial x} . \quad (\text{D-3})$$

It follows that application of the divergence operator ($\nabla \cdot$) to a real multi-component seismic record will effectively recover P energy from the vector data, while the S wavefield can be extracted via the curl operator ($\nabla \times$).

In order to recover P- and S-wave records via equations (D-2) and (D-3), the spatial derivatives of the recorded displacement data with respect to x and z must be computed. Since only surface recorded data are typically available for seismic exploration applications, it is necessary to determine additional information about the wavefield at depth to enable computation of the vertical derivatives. Here downward continuation of the elastic data in the time domain via a finite-difference approach is used to extract seismic displacement at depth. This follows the examples of Sun (1999) and Zhe and Greenhalgh (1997).

Downward continuation of surface vector data can be considered the inverse of elastic forward modelling. Here, an explicit second-order time and fourth-order space, finite-difference scheme is implemented to perform the downward continuation. This is based on the velocity-stress staggered-grid formulation of Virieux (1986). In order to drive the reverse-time propagation, the vertical and horizontal components of the input seismic record are inserted as time-varying surface boundary conditions on the vertical-component and horizontal-component finite-difference grids, respectively (Sun and McMechan, 1986). Note that, the recorded wavefields may need to be interpolated to match the spacing of the computational grid used for the downward continuation, which, in turn, is chosen to meet stability and grid-dispersion criteria (e.g., Levander, 1988; Virieux, 1986). To initiate the reverse-time recursion process, it is assumed that beyond the maximum time of recording there is no significant energy. In practice, tapering of the data is recommended to help satisfy this assumption and reduce artefacts associated with the finiteness of the seismic data. To prevent artificial reflections from the bottom and sides of the finite-difference grids during downward continuation, the absorbing boundary conditions of Cerjan *et al.* (1985) have been implemented.

Note that the spatial derivatives in equations (D-2) and (D-3) introduce a $\pi/2$ phase shift between the input displacement data and the output dilatation and rotation. Sun *et al.* (2001) demonstrate that this phase shift can be corrected by performing a Hilbert transform with respect to time on the separated P and S records. Note that, for real seismic data, we are typically working with velocity rather than displacement data. In this instance, the displacement, dilatation, and rotation in equations (D-1) to (D-3) should be replaced with their individual time derivatives. The phase correction still remains valid.

APPENDIX E

CONVERTED-WAVE PROCESSING OF TRIAL DATASET #1

The inline component data from Trial Dataset #1 were reprocessed using the best-available technology at the time. Note that, there has been significant development in our PS processing flow since then, and the data would be manipulated differently now. However, the focus of this reprocessing trial is the inclusion of the vector-processing step into the PS processing flow.

Reformat

Field data were reformatted from SEGY to the Seismic Unix internal C-binary format.

Geometry

Geometry details, including source and receiver locations, elevation, offsets, P-wave CDP numbers and P-wave source statics, were assigned to trace headers.

Trace Editing

Dead or noisy traces were removed from field records.

Vector Processing

Separation of P- and S-wave energy via Elastic Wavefield Decomposition (EWD) (Appendix D). Relevant processing parameters are as follows:

$$V_p = 1400 \text{ m/s}$$

$$V_s = 700 \text{ m/s}$$

$$\text{downward continuation depth} = 12.5 \text{ m}$$

$$dx = dz = 1.0 \text{ m}$$

$$\text{dominant P-wave frequency} = 70 \text{ Hz}$$

Polarity Reversal

The polarity of all inline traces with negative offsets was reversed.

P-wave Source Static + Residual Source Static Correction

Static corrections are applied to the seismic data to compensate for the effects of variations in elevation, weathering thickness and weathering velocity. The objective is to determine the arrival times of reflection events that would have been observed if seismic acquisition had been undertaken on a flat plane with no weathering or low-velocity material present. The P-wave statics for the downgoing portion of the converted-wave raypath can be obtained from conventional P-wave processing. The total P-wave source statics, together with the residual source statics were applied to the inline data.

Brute V_p/V_s Analysis – 1st Iteration

A V_p/V_s function that could approximately flatten PS reflection events on common-receiver gathers (CRGs) was picked to produce a CRG stack for subsequent S-wave receiver static computation. Note that, a constant V_p of 3000 m/s was assumed.

S-wave Receiver Static Corrections – 1st Iteration

Static corrections associated with the upwards travelling S wave passing through the weathering layer were computed using the manual CRG stack method described in Section 4.2. Note that, an attempt to accommodate structure along the PS reflection event was made by flattening the PS CRG stack along the predicted PS two-way time (TWT) surface (predicted using the P-wave CRG stack). Remaining time variations in the PS CRG stack could then be attributed to true receiver static shifts.

Brute V_p/V_s Analysis – 2nd Iteration

A second-pass V_p/V_s function that could approximately flatten PS reflection events on CRGs following application of the 1st pass of receiver static corrections was picked. The improved CRG stack was required for a second iteration of S-wave receiver statics. Again, a constant V_p of 3000 m/s was assumed.

S-wave Receiver Static Corrections – 2nd Iteration

A second iteration of S-wave receiver static computation was undertaken to yield the optimally smoothed CRG stack (and therefore, in theory, the best S-wave receiver statics). As before, structure was accommodated in the calculation by predicting the PS TWT structure using the P-wave CRG stack (and a constant V_p/V_s of 1.6).

V_p/V_s Analysis

A series of constant V_p/V_s common-conversion point (CCP) stacks were computed to extract a spatially-variant V_p/V_s function for PS-wave normal-moveout correction and CCP binning. For each trial V_p/V_s value, the CCP gathers are regenerated via 'horizon-based' CCP binning. Note that, only traces with either positive OR negative offsets are considered at any one time to work around the diodic nature of the PS reflection events observed in the CCP gathers. A constant V_p of 3000 m/s was assumed to determine the final V_p/V_s function.

CCP Binning

CCP binning is the process of gathering inline traces that share the same sub-surface P-to-S conversion point. CCP gathers were created using 'horizon-based' CCP binning and the final V_p/V_s function as determined in the previous processing step.

Normal Moveout Correction

The arrival time of a reflection event will vary with offset as a result of the changing raypath. Normal moveout (NMO) corrections compensate for this variation in traveltime so that reflection energy from effectively the same P-to-S conversion point on each geological boundary is properly aligned prior to stacking.

Stretch Mute

A 50% stretch mute was applied to eliminate refractors and stretch caused by normal moveout corrections.

Offset Mute

Very little converted-wave energy is observed on the near-offset traces of a CCP gather. This is consistent with PS amplitudes predicted by wave-equation theory. Consequently, all traces with offsets less than 120 m were eliminated.

CCP Trim Static Correction

Trim static corrections are corrective time shifts applied to NMO-corrected CCP gathers prior to stacking to ensure reflection events are optimally flattened. Computing the static correction involves the correlation of each trace within the CCP gather with a pilot trace for that gather. Here, the pilot trace was the resultant stacked trace for that CCP gather (either positive or negative offset traces), following bandpass filtering and a 9-trace running mix. The correlation window was 150 ms about the target reflection event. Trim static corrections were limited to a maximum of 8 ms.

Pre-Stack AGC

An automatic gain function (AGC) was applied using a 150 ms window to help strengthen the amplitude of the reflection event with respect to background noise.

CCP Stack

All traces that share a CCP location were stacked. The post-stack trace was scaled by the square root of the sum of fold for each sample in the trace. Note that, to work around the non-symmetric moveout of PS reflection events in the CCP gathers, only traces with either positive or negative offsets are generally summed. For this dataset, negative offset traces were used for all CCPs in the range 250-660, and positive-offset traces were used for all CCPs in the range 661-800.

FX-Deconvolution

Coherent seismic reflectors in the PS-wave stack were enhanced using *fx*-deconvolution to attenuate random noise. Relevant processing parameters are as follows:

Frequency bandwidth:	15-180 Hz
Number of traces in analysis window:	200
Window Length:	450 ms
Number of traces in filter:	10

Post-Stack AGC

An automatic gain function (AGC) was applied using a 250 ms window to help strengthen the amplitude of the stacked reflection event with respect to background noise.

Bandpass Filter

The final stack was filtered using a zero-phase bandpass filter 17/25 – 90/120Hz.

APPENDIX F

CONVERTED-WAVE PROCESSING OF TRIAL DATASET #2

The inline component data from Trial Dataset #2 were reprocessed using our most recently developed processing algorithms. Comparison of this processing flow with the original Trial #2 processing flow detailed in Velseis (2003) highlights the significant improvements that have been made in the processing of converted-wave coal seismic data over the past three years.

Reformat

Field data were reformatted from SEGY to the Seismic Unix internal C-binary format.

Geometry

Geometry details, including source and receiver locations, elevation, offsets, P-wave CDP numbers and P-wave source statics, were assigned to trace headers.

Trace Editing

Dead or noisy traces were removed from field records.

Polarity Reversal

The polarity of all inline traces with negative offsets was reversed.

Spherical Divergence Correction

A time-varying scale factor was applied to each trace to compensate for the effects of amplitude loss due to geometrical spreading. The conventional P-wave spherical divergence correction of $[t \times v \times v]^{-1}$, where t is the two-way time and v is the average P-wave velocity, was applied to each time sample in the data. The average P-wave velocity function used to apply this correction was:

Time (s)	Velocity (m/s)
0	1600
0.05	2400
0.3	3500
0.7	4700

P-wave Source Static + Residual Source Static Correction

Static corrections are applied to the seismic data to compensate for the effects of variations in elevation, weathering thickness and weathering velocity. The objective is to determine the arrival times of reflection events that would have been observed if seismic acquisition had been undertaken on a flat plane with no weathering or low-velocity material present. The P-wave statics for the downgoing portion of the converted-wave raypath can be obtained from conventional P-wave processing.

The high-frequency component of the P-wave source statics, together with the residual source statics were applied to the inline data. (Note that, the high frequency component of the P-wave

source statics are derived by subtracting a smoothed version of the conventional P-wave refraction static corrections from the total correction. The smoothed static corrections are created by running a 51-point averaging window across the statics.) This effectively moves the data to an interim processing datum. The remaining P-wave static correction is applied as part of the 'CCP Static Correction' at the end of the processing sequence to shift the data to the final datum of 200 m ASL.

Deconvolution

The recorded seismic signal can be considered as the convolution of the source signal with the instruments, the geophones and the response of the earth. The objective of deconvolution is to estimate these effects as linear filters, and then design and apply inverse filters to whiten (or spike) the data.

A non surface-consistent predictive deconvolution operator was applied to the data. The relevant processing parameters are as follows:

Minimum Lag:	0.001 s
Maximum Lag:	0.20 s
Correlation Window:	0.15 – 0.65 s

0.001% white noise was added to the autocorrelogram before an inverse whitening filter was designed.

Pre-Stack Zero-Phase Spectral Whitening

Spectral whitening was applied to equalise all frequency components of the seismic signal. The signal magnitude spectrum was divided into three panels (10/20-50/60Hz; 50/60-90/100 Hz, and 90/100-130/150 Hz), and balanced using a 50ms sliding window.

S-wave Receiver Static Corrections

Static corrections associated with the upwards travelling S wave passing through the weathering layer are computed using traveltimes for a specific PS reflection event on each common-offset receiver section. The time picks are fed into the surface-consistent statics model, and the receiver static component is solved for in a least-squares sense. Only the high-frequency components of the S-wave receiver static corrections are applied to the data. This effectively completes the shift of the data to an interim processing datum. The remaining S-wave static correction is applied as part of the 'CCP Static Correction' at the end of the processing sequence to shift the data to the final datum of 200m ASL.

Vp/Vs Analysis

A series of constant Vp/Vs CCP stacks were computed to extract a spatially- and time-variant Vp/Vs function for PS-wave normal-moveout correction and CCP binning. For each trial Vp/Vs value, the CCP gathers are regenerated via dynamic CCP binning. Note that, only traces with either positive OR negative offsets are considered at any one time to work around the diodic

nature of the PS reflection events observed in the CCP gathers. A constant V_p of 3000 m/s was assumed to determine the final V_p/V_s function.

CCP Binning

CCP binning is the process of gathering inline traces that share the same sub-surface P-to-S conversion point. The location of the conversion point is a function of V_p/V_s and the depth of the boundary at which the conversion occurs.

CCP gathers were created using dynamic CCP binning and the final V_p/V_s function as determined in the previous processing step.

Normal Moveout Correction

The arrival time of a reflection event will vary with offset as a result of the changing raypath. Normal moveout (NMO) corrections compensate for this variation in traveltime so that reflection energy from effectively the same P-to-S conversion point on each geological boundary is properly aligned prior to stacking.

Stretch Mute

A 60% stretch mute was applied to eliminate refractors and stretch caused by normal moveout corrections.

Offset Mute

Very little converted-wave energy is observed on the near-offset traces of a CCP gather. This is consistent with PS amplitudes predicted by wave-equation theory. Consequently, an inner trace mute was applied to eliminate near-offset traces from the stacking process. The mute design was:

Offset	Time (s)
-350	0.65
-300	0.22
-120	0.2
-80	0.0
120	0.0
120	0.2
350	0.28
450	0.65

CCP Trim Static Correction

Trim static corrections are corrective time shifts applied to NMO-corrected CCP gathers prior to stacking to ensure reflection events are optimally flattened. Computing the static correction involves the correlation of each trace within the CCP gather with a pilot trace for that gather. Here, the pilot trace was the resultant stacked trace for that CCP gather (either positive or negative offset traces), following f_x -deconvolution, bandpass filtering and AGC. The correlation

window was 200 ms about one of the target reflection events. Trim static corrections were limited to a maximum of 15 ms.

Pre-Stack AGC

An automatic gain function (AGC) was applied using a 650 ms window to help strengthen the amplitude of reflection events with respect to background noise.

CCP Stack

All traces that share a CCP location were stacked. The post-stack trace was scaled by the square root of the sum of fold for each sample in the trace. Note that, to work around the non-symmetric moveout of PS reflection events in the CCP gathers, only traces with either positive or negative offsets are generally summed. For this dataset, only positive offset traces were used to create the final PS stack.

Post-Stack Zero-Phase Spectral Whitening

Spectral whitening was applied to equalise all frequency components of the seismic signal. The signal magnitude spectrum was divided into three panels (10/20-40/50Hz; 40/50-80/90 Hz, and 80/90-120/150 Hz), and balanced using a 50ms sliding window.

FX-Deconvolution

Coherent seismic reflectors in the PS-wave stack were enhanced using *fx*-deconvolution to attenuate random noise. Relevant processing parameters are as follows:

Frequency bandwidth:	10-150 Hz
Number of traces in analysis window:	20
Window Length:	450 ms
Number of traces in filter:	10

Eigenvector Filtering

Eigenvector filtering uses Karhunen-Loeve theory to decompose the data traces into eigenimages through the use of eigenvectors. The data can be reconstructed using just the dominant eigenvectors to remove random noise and improve the signal-to-noise ratio. Here a trace window width of 200 was used to decompose the data into eigenimages. The first 20 eigenimages were used to reconstruct the seismic section.

FX-Deconvolution

A second-pass of *fx*-deconvolution was used to attenuate random noise. Relevant processing parameters are as follows:

Frequency bandwidth:	10-180 Hz
Number of traces in analysis window:	20
Window Length:	450 ms
Number of traces in filter:	10

Bandpass Filter

The final stack was filtered using a zero-phase bandpass filter 12/17 – 120/150Hz.

Post-Stack AGC

An automatic gain function (AGC) was applied using a 250 ms window to help strengthen the amplitude of stacked reflection events with respect to background noise.

CCP Static Correction

The low-frequency components of the source and receiver static corrections were applied to the post-stack data to shift the section to the final datum (200 m ASL). (Note that the S-wave elevation static correction assumes an S-wave replacement velocity of half the P-wave replacement velocity i.e. $V_{\text{replacement}} = 1500 \text{ m/s}$)

APPENDIX G

PROCESSING OF TRIAL DATASET #3

The conventional P-wave seismic section is produced by applying standard seismic-processing algorithms to the data recorded on the vertical component of the 3C geophone. The converted-wave (PS-wave) stack is typically generated via processing of the data acquired on the inline component of the 3C geophone.

G.1 P-Wave Processing

The vertical component data were processed by Velseis Processing Pty Ltd using ProMAX processing software. Details of the P-wave processing sequence are given below.

Reformat

Field data were reformatted from SEGY to ProMAX internal data format.

Geometry

Geometry details, including source and receiver locations, elevation, offsets and CDP numbers, were assigned to trace headers.

Trace Editing

Dead or noisy traces were removed from field records.

Spherical Divergence Correction

A time-varying scale factor was applied to each trace to compensate for the effects of amplitude loss due to geometrical spreading. The gain applied to each sample was $[t \times v \times v]^{-1}$, where t is the two-way time, and v is the average P-wave velocity (here set to 3500 m/s).

Refraction Static Corrections

Refraction static corrections are applied to the seismic data to compensate for the effects of variations in elevation, weathering thickness and weathering velocity. The objective is to determine the arrival times of reflection events that would have been observed if seismic acquisition had been undertaken on a flat plane with no weathering or low-velocity material present.

First arrival times of recorded refracted energy were picked, edited and loaded into trace headers in order to compute refraction static corrections. The weathering velocity (v_0) was computed directly from uphole times. A replacement velocity of 3000 m/s, and a datum of 300 m ASL were used. The high-frequency components of the source and receiver static corrections were then applied to the data. (Note that, the high-frequency components of the static corrections are derived by subtracting a smoothed version of the static corrections from the total correction. The smoothed static corrections are created by running a 51-point averaging window across the static corrections.) This effectively moves the data to an interim processing datum. The remaining

static correction is applied as a 'CDP Static Correction' following stacking, to shift the data to the final datum of 300 m ASL.

Deconvolution

The recorded seismic signal can be considered as the convolution of the source signal with the instruments, the geophones and the response of the earth. The objective of deconvolution is to estimate these effects as linear filters, and then design and apply inverse filters to whiten (or spike) the data.

The optimal spiking operators were produced from a decomposition of the source, receiver and offset components of the seismic wavelet, and an application of the source and receiver operators only. The design window was:

Offset (m)	Window Start (ms)	Window End (ms)
3	53	990
620	373	990

0.1% white noise was added to the autocorrelogram before an inverse whitening filter was designed. The total operator length was 160 ms.

Pre-Stack Zero-Phase Spectral Whitening

Spectral whitening was applied to equalise all frequency components of the seismic signal. The signal magnitude spectrum was divided into two panels, and balanced using a 50ms sliding window. Following scaling, the individual frequency bands of data were summed and weighted to maintain the mean amplitude. The output spectrum was 20/30 – 350/400 Hz.

Velocity Analysis

First pass stacking velocities were picked interactively every 50 CDPs. Supergathers, comprising traces from 11 CDPs centred about each analysis point, were used to produce velocity spectra, moveout-corrected gathers and stacked panels to assist with the careful interpretation of stacking velocities.

Residual Static Corrections

Residual static corrections are corrective time shifts applied to the data to compensate for remnant statics associated with incomplete weathering static corrections. Surface-consistent residual static corrections were calculated and applied using Maximum Power Autostatics.

Pilot traces were formed for a 250 ms analysis window by flattening all NMO-corrected traces along the autostatics horizon, and summing traces from 9 consecutive CDP gathers. A 3-trace mix (with weighting factors 1,8,1) was applied prior to summation.

Each trace from the active CDP gather was time shifted relative to the relevant pilot trace and summed with it. The power of the subsequent stack was measured for each time shift. This shift-

power trace was then summed with other traces having the same source and receiver, in their respective domains. On completion of the shift spectra for the entire line, time shifts were picked at the maximum of the power shift spectra and stored as static values. A maximum static correction of 12 ms was allowed. The static corrections were applied, the pilot traces were updated, and the process was repeated. For this dataset, these calculations were repeated for 9 iterations, or until the RMS of the change in the computed statics was less than 0.05 ms.

Velocity Analysis

Second pass stacking velocities were picked interactively every 25 CDPs. Supergathers, comprising traces from 11 CDPs centred about each analysis point, were used to produce velocity spectra, moveout-corrected gathers and stacked panels to assist with the careful interpretation of stacking velocities.

Residual Static Corrections

To optimise shot and receiver residual static corrections, a second pass of surface consistent residual static corrections were computed and applied to the data following second-pass velocity analysis. This time the pilot traces were formed for a 350 ms analysis window by flattening all NMO-corrected traces along the autostatics horizon, and summing traces from 7 consecutive CDP gathers. As before, a maximum static correction of 12 ms was allowed. The calculations were repeated for 9 iterations, or until the RMS of the change in the computed statics was less than 0.05 ms.

Normal Moveout Correction

The arrival time of a reflection event will vary with offset as a result of the changing raypath. Normal moveout (NMO) corrections compensate for this variation in traveltime so that reflection energy from effectively the same point on each geological boundary is properly aligned prior to stacking. The normal moveout correction is defined by:

$$t_x^2 = \frac{t_0^2 + x^2}{v^2} ,$$

where t_x =time at offset x , t_0 =time at zero offset, x =offset of trace (m), and v =stacking velocity at time t .

Stretch Mute

A 25% stretch mute was applied to eliminate refractors and stretch caused by normal moveout corrections.

CDP Trim Static Correction

Trim static corrections are corrective time shifts applied to NMO-corrected CDP gathers prior to stacking to ensure reflection events are optimally flattened. Computing the static correction involves the correlation of each trace within the CDP gather with a pilot trace for that gather. Here, the pilot trace was the resultant stacked trace for that CDP gather, following second-pass

residual statics, fx -deconvolution, eigenvector filtering, bandpass filtering and AGC. The correlation window was defined by:

CDP	Window Start (ms)	Window End (ms)	Window Length (ms)
200	44	255	211
410	56	291	235
515	63	306	243
600	60	318	258

Trim static corrections were limited to a maximum of 4 ms.

Pre-Stack AGC

An automatic gain function (AGC) was applied using a 150 ms window to help strengthen the amplitude of reflection events with respect to background noise.

CDP Stack

All traces that share a CDP location were stacked. The post-stack trace was scaled by the square root of the sum of fold for each sample in the trace.

CDP Static Correction

The low-frequency components of the source and receiver static corrections were applied to the post-stack data to shift the section to the final datum (300 m ASL).

FX-Deconvolution

Coherent seismic reflectors in the P-wave stack were enhanced using fx -deconvolution to attenuate random noise. Relevant processing parameters are as follows:

Frequency bandwidth:	20-350 Hz
Number of traces in analysis window:	300
Window Length:	500 ms
Number of traces in filter:	100

Eigenvector Filtering

Eigenvector filtering uses Karhunen-Loeve theory to decompose the data traces into eigenimages through the use of eigenvectors. The data can be reconstructed using just the dominant eigenvectors to remove random noise and improve the signal-to-noise ratio. Here a trace window width of 400 was used to decompose the data into eigenimages. The first 40 eigenimages were used to reconstruct the seismic section.

Migration

Fast explicit finite-difference time migration was used to help map seismic reflectors to their correct spatial position. The maximum migration frequency was set to 350 Hz. The migration velocity model was derived from 95% of the smoothed stacking velocities.

Post-Stack Zero-Phase Spectral Whitening

Spectral whitening was applied to equalise all frequency components of the seismic signal. The signal magnitude spectrum was divided into two panels, and balanced using a 50ms sliding window. Following scaling, the individual frequency bands of data were summed and weighted to maintain the mean amplitude. The output spectrum was 20/30 – 300/350 Hz.

Eigenvector Filtering

A second pass of eigenvector filtering was used to help reduce random noise in the seismic section. Again, a trace window width of 400 was used to decompose the data into eigenimages. The first 40 eigenimages were used to reconstruct the seismic section.

Bandpass Filter

The final stack was filtered using a Ormsby Bandpass Filter 20/30 – 300/350Hz.

G.2 PS-Wave Processing

The inline component data were processed by the R&D Division of Velseis using proprietary processing software developed and implemented within the Seismic Unix framework (Cohen and Stockwell, 2002). Details of the PS-wave processing sequence are given below.

Reformat

Field data were reformatted from SEG Y to the Seismic Unix internal C-binary format.

Geometry

Geometry details, including source and receiver locations, elevation, offsets, P-wave CDP numbers and P-wave source statics, were assigned to trace headers.

Trace Editing

Dead or noisy traces were removed from field records.

Polarity Reversal

The polarity of all inline traces with negative offsets was reversed.

Spherical Divergence Correction

A time-varying scale factor was applied to each trace to compensate for the effects of amplitude loss due to geometrical spreading. The conventional P-wave spherical divergence correction of $[t \times v \times v]^{-1}$, where t is the two-way time, and v is the average P-wave velocity (here set to 3500 m/s) was applied to each time sample in the data.

P-wave Source Static + Residual Source Static Correction

Static corrections are applied to the seismic data to compensate for the effects of variations in elevation, weathering thickness and weathering velocity. The objective is to determine the arrival times of reflection events that would have been observed if seismic acquisition had been undertaken on a flat plane with no weathering or low-velocity material present. The P-wave

statics for the downgoing portion of the converted-wave raypath can be obtained from conventional P-wave processing.

The high-frequency component of the P-wave source statics, together with the residual source statics were applied to the inline data. (Note that, the high frequency component of the P-wave source statics are derived by subtracting a smoothed version of the conventional P-wave refraction static corrections from the total correction. The smoothed static corrections are created by running a 51-point averaging window across the statics.) This effectively moves the data to an interim processing datum. The remaining P-wave static correction is applied as part of the 'CCP Static Correction' at the end of the processing sequence to shift the data to the final datum of 300 m ASL.

Deconvolution

The recorded seismic signal can be considered as the convolution of the source signal with the instruments, the geophones and the response of the earth. The objective of deconvolution is to estimate these effects as linear filters, and then design and apply inverse filters to whiten (or spike) the data.

A non surface-consistent predictive deconvolution operator was applied to the data. The relevant processing parameters are as follows:

Minimum Lag:	0.001 s
Maximum Lag:	0.320 s
Correlation Window:	0.1 – 0.65 s

0.001% white noise was added to the autocorrelogram before an inverse whitening filter was designed.

Pre-Stack Zero-Phase Spectral Whitening

Spectral whitening was applied to equalise all frequency components of the seismic signal. The signal magnitude spectrum was divided into three panels (10/20-40/50Hz; 40/50-80/90 Hz, and 80/90-120/130 Hz), and balanced using a 50ms sliding window.

S-wave Receiver Static Corrections

Static corrections associated with the upwards travelling S wave passing through the weathering layer are computed using traveltimes picks for a specific PS reflection event on each common-offset receiver section. The time picks are fed into the surface-consistent statics model, and the receiver static component is solved for in a least-squares sense. Only the high-frequency components of the S-wave receiver static corrections are applied to the data. This effectively completes the shift of the data to an interim processing datum. The remaining S-wave static correction is applied as part of the 'CCP Static Correction' at the end of the processing sequence to shift the data to the final datum of 300m ASL.

Figure G.1 compares the high- and low-frequency components of the P-wave and S-wave receiver statics for Trial #3. With the introduction of the new S-wave receiver statics method we are finding that the general trends in the P-wave and S-wave statics are comparable. As expected, however, the S-wave receiver statics are generally larger in magnitude than the P-wave statics. This is due to the S-wave velocities being significantly lower than P-wave velocities in the weathering layer.

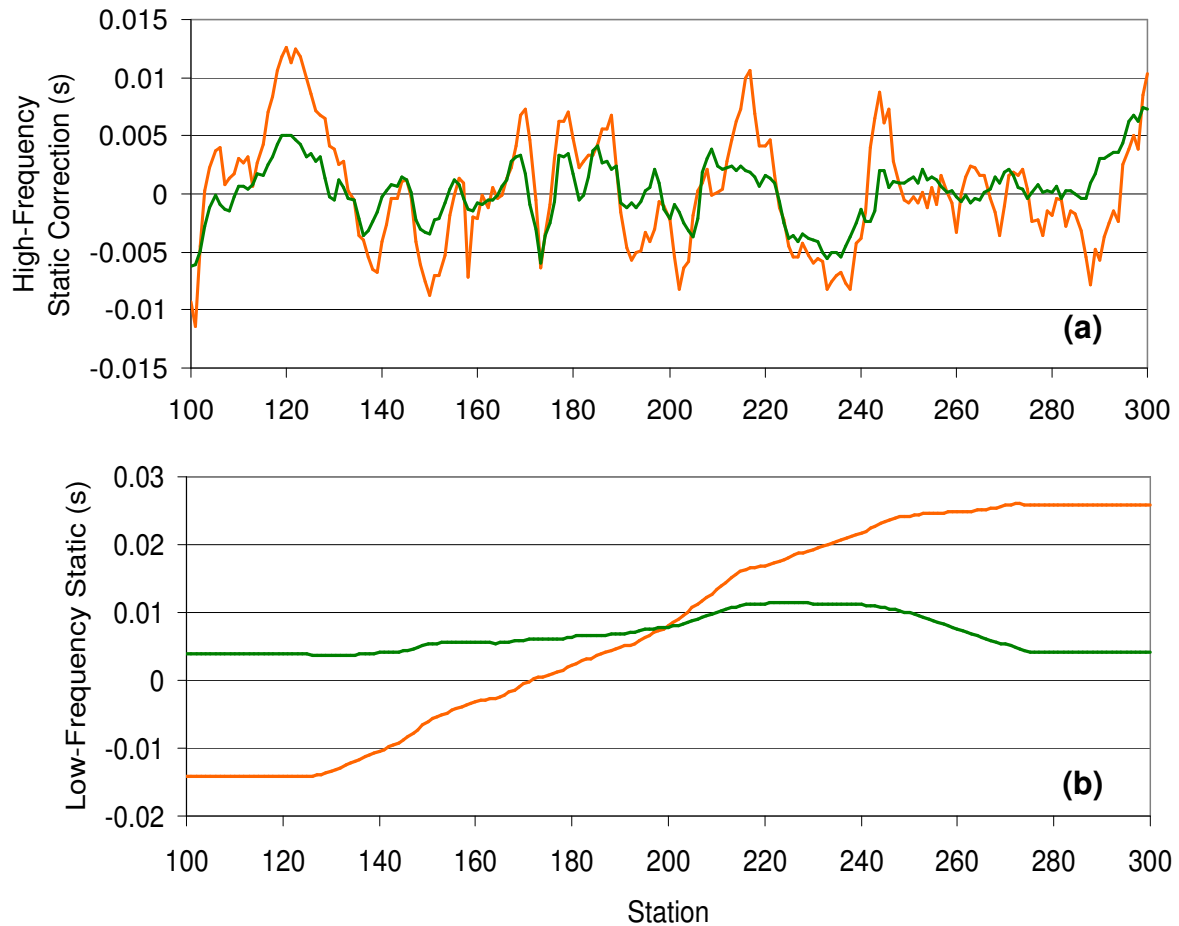


Figure G.1 Comparison of the (a) high-frequency components of the P (green) and S (orange) receiver static corrections for Trial #3, and (b) low-frequency components of the P (green) and S (orange) receiver statics for Trial #3.

V_p/V_s Analysis

A series of constant V_p/V_s CCP stacks were computed to extract a spatially- and time-variant V_p/V_s function for PS-wave normal-moveout correction and CCP binning. For each trial V_p/V_s value, the CCP gathers are regenerated via dynamic CCP binning. Note that, only traces with either positive OR negative offsets are considered at any one time to work around the diodic nature of the PS reflection events observed in the CCP gathers. A constant V_p of 2900 m/s was assumed to determine the final V_p/V_s function.

CCP Binning

CCP binning is the process of gathering inline traces that share the same sub-surface P-to-S conversion point. The location of the conversion point is a function of V_p/V_s and the depth of the boundary at which the conversion occurs.

CCP gathers were created using dynamic CCP binning and the final V_p/V_s function as determined in the previous processing step.

Normal Moveout Correction

The arrival time of a reflection event will vary with offset as a result of the changing raypath. Normal moveout (NMO) corrections compensate for this variation in traveltime so that reflection energy from effectively the same P-to-S conversion point on each geological boundary is properly aligned prior to stacking.

Stretch Mute

A 60% stretch mute was applied to eliminate refractors and stretch caused by normal moveout corrections.

Offset Mute

Very little converted-wave energy is observed on the near-offset traces of a CCP gather. This is consistent with PS amplitudes predicted by wave-equation theory. Consequently, an inner trace mute was applied to eliminate near-offset traces from the stacking process. The mute design was:

Offset	Time (s)
-800	0.65
-500	0.54
-240	0.3
-100	0.0
100	0.0
240	0.3
500	0.54
800	0.65

CCP Trim Static Correction

Trim static corrections are corrective time shifts applied to NMO-corrected CCP gathers prior to stacking to ensure reflection events are optimally flattened. Computing the static correction involves the correlation of each trace within the CCP gather with a pilot trace for that gather. Here, the pilot trace was the resultant stacked trace for that CCP gather (either positive or negative offset traces), following f_x -deconvolution, bandpass filtering and AGC. The correlation window was 220 ms about one of the target reflection events. Trim static corrections were limited to a maximum of 15 ms.

Pre-Stack AGC

An automatic gain function (AGC) was applied using a 650 ms window to help strengthen the amplitude of reflection events with respect to background noise.

CCP Stack

All traces that share a CCP location were stacked. The post-stack trace was scaled by the square root of the sum of fold for each sample in the trace. Note that, to work around the non-symmetric moveout of PS reflection events in the CCP gathers, only traces with either positive or negative offsets are generally summed. For this dataset, negative offset traces were used for all CCPs in the range 200-511, and positive-offset traces were used for all CCPs in the range 512-580.

Post-Stack Zero-Phase Spectral Whitening

Spectral whitening was applied to equalise all frequency components of the seismic signal. The signal magnitude spectrum was divided into three panels (10/20-40/50Hz; 40/50-80/90 Hz, and 80/90-120/150 Hz), and balanced using a 50ms sliding window.

FX-Deconvolution

Coherent seismic reflectors in the PS-wave stack were enhanced using *fx*-deconvolution to attenuate random noise. Relevant processing parameters are as follows:

Frequency bandwidth:	10-150 Hz
Number of traces in analysis window:	10
Window Length:	450 ms
Number of traces in filter:	5

Eigenvector Filtering

Eigenvector filtering uses Karhunen-Loeve theory to decompose the data traces into eigenimages through the use of eigenvectors. The data can be reconstructed using just the dominant eigenvectors to remove random noise and improve the signal-to-noise ratio. Here a trace window width of 200 was used to decompose the data into eigenimages. The first 25 eigenimages were used to reconstruct the seismic section.

FX-Deconvolution

A second-pass of *fx*-deconvolution was used to attenuate random noise. Relevant processing parameters are as follows:

Frequency bandwidth:	10-180 Hz
Number of traces in analysis window:	100
Window Length:	450 ms
Number of traces in filter:	10

Bandpass Filter

The final stack was filtered using a zero-phase bandpass filter 12/17 – 120/150Hz.

Post-Stack AGC

An automatic gain function (AGC) was applied using a 250 ms window to help strengthen the amplitude of stacked reflection events with respect to background noise.

CCP Static Correction

The low-frequency components of the source and receiver static corrections were applied to the post-stack data to shift the section to the final datum (300 m ASL). (Note that the S-wave elevation static correction assumes an S-wave replacement velocity of half the P-wave replacement velocity i.e. $V_{\text{replacement}} = 1500 \text{ m/s}$)

APPENDIX H SEISMIC RESOLUTION

H.1 Measurements of Resolution

There are a number of quasi-theoretical measures of vertical resolution which are often used to determine the vertical resolving power of P-wave seismic data.

The 'detectable limit' is defined as the minimum layer thickness required to produce an observable seismic reflection (Sheriff, 1991). This is generally taken to be of the order of $\lambda_D/30$, where λ_D is the dominant wavelength of the P wave:

$$\lambda_D = \frac{V_{int}}{f_D}, \quad (H-1)$$

f_D is the dominant frequency of the seismic wave, and V_{int} is the interval velocity of the geological layer being considered. The dominant frequency in a seismic record is equivalent to $1/T$, where T is the time between adjacent peaks on a display of the seismic data (Figure H.1). Note of course, that detection of a geological layer presupposes a sufficiently strong density and velocity contrast across the layer interfaces.

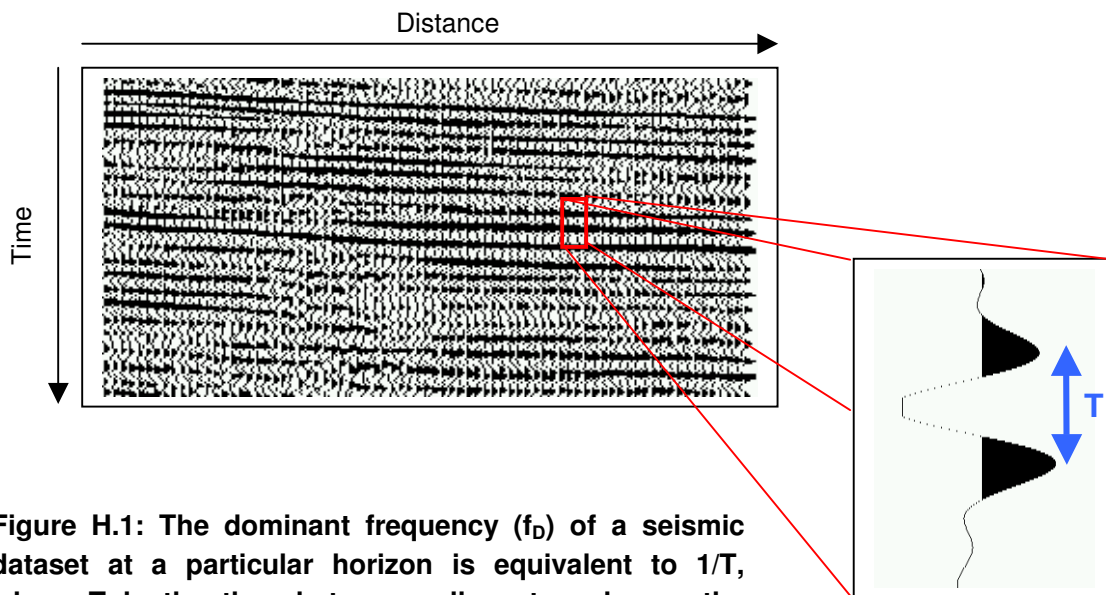


Figure H.1: The dominant frequency (f_D) of a seismic dataset at a particular horizon is equivalent to $1/T$, where T is the time between adjacent peaks on the display of the seismic reflection event.

The commonly used 'Rayleigh resolution limit', defined as the minimum separation of discrete seismic reflectors at which one can ascertain more than one interface is present (Sheriff, 1991), is $\lambda_D/4$. The 'Widess limit' is an alternative, and more optimistic definition, which states that two interfaces are resolvable if their separation is greater than or equal to $\lambda_D/8$ (Sheriff, 1991).

Note that these rule-of-thumb measures for P-waves are approximate, and strictly derived for resolution issues relating to layer thickness. Nevertheless, they do provide some indication of the ability of a P-wave section to resolve other geological features (e.g. faults). Obviously these resolution measurements become over-optimistic in the presence of significant noise.

H.2 P versus PS Resolution

According to the above discussion the vertical resolution of a P image is related to the interval velocity of the layer of interest, and the dominant frequency of the data. This also holds true for PS data, although it is necessary to take into account both V_p/V_s and the dominant P and PS frequencies when determining relevant resolution limits. It can be shown that the PS resolution limit is equivalent to the P resolution limit scaled by:

$$\frac{2}{\left(1 + \frac{V_p}{V_s}\right)} \cdot \frac{f_{Dp}}{f_{Dps}}, \quad (\text{H-2})$$

where f_{Dp} and f_{Dps} are the dominant frequencies of the P and PS reflection events of interest, respectively. Note that, V_p/V_s will always be larger than one. Thus, for P and PS images exhibiting the same frequency content, the scale factor in equation (H-2) will always be less than one and the PS image will be able to resolve thinner geological layers than the P-wave data. In the case where the dominant frequency of the PS energy is lower than for the corresponding P energy, it is still possible for the PS image to have greater vertical resolution. Based on the scale factor given by equation (H-2), the dominant frequency of the PS data need only satisfy:

$$f_{Dps} \geq \frac{2f_{Dp}}{\left(1 + \frac{V_p}{V_s}\right)} \quad (\text{H-3})$$

for the PS section to better or equal the vertical resolution of the P image.

H.3 Resolution of P and PS Stacks for Trial Dataset #2

Figure 6.4 shows representative stacked-trace spectra for the final P and PS sections from Trial #2. The average dominant frequencies for the stacked P and PS data across the target reflectors are 130 Hz and 40 Hz, respectively. The average P- and S-wave interval velocities of the coal seams are approximated to be 2300 m/s and 920 m/s, respectively. Using equation (H-1), the dominant wavelength for the P-wave section is 18 m, and the Rayleigh resolution limit is 4.5 m. From equation (H-2) we can determine that the corresponding PS Rayleigh resolution limit is approximately 8.5 m. Thus, as we observe in Figure 6.1, the PS stack has poorer vertical resolution than the P stack.

H.4 Resolution of Raw P and PS Data for Trial Dataset #3

Figure 7.4 shows representative frequency spectra for vertical- and inline- component traces from Trial Dataset #3. The average dominant frequencies of the P and PS reflection energy are 75 Hz and 55 Hz, respectively. The average P- and S-wave interval velocities of the coal seams are approximated to be 2300 m/s and 920 m/s, respectively. Using equation (H-1), the dominant wavelength for the P-wave energy is 30 m, and the Rayleigh resolution limit is 7.5 m. From equation (H-2) we can determine that the corresponding PS Rayleigh resolution limit for the raw PS data is approximately 5.8 m. Based on this resolution analysis, it is feasible that the final PS section for Trial #3 could exhibit greater vertical resolution than the conventional P-wave section.

H.5 Resolution of P and PS Stacks for Trial Dataset #3

Figure 7.6 shows representative stacked-trace spectra for the final P and PS sections from Trial #3. The average dominant frequency of the stacked P data is approximately 160 Hz. The average dominant frequency of the stacked PS data is approximately 35 Hz. The average P- and S-wave interval velocities of the coal seams are approximated to be 2300 m/s and 920 m/s, respectively. Using equation (H-1), the dominant wavelength for the P-wave section is 14.5 m, and the Rayleigh resolution limit is 3.6 m. From equation (H-2) we can determine that the corresponding PS Rayleigh resolution limit is approximately 9.5 m. Thus, despite the raw data indicating that the PS section could have greater resolution than the P section (Section H.4), the final PS stack suffers from much lower resolution than the P stack. In fact, the Rayleigh resolution limit of the PS data has become larger as a result of the PS processing flow. Understanding the reason behind this behaviour, and attempting to compensate for it, will be the topic of future research.

APPENDIX I

SYNTHETIC SEISMIC MODELLING

The synthetic seismic data used for this research project have been generated via the 2D second-order time, second-order space elastic finite-difference modelling technique of Virieux (1986). The free-surface boundary conditions of Mittet (2002) are enforced along the upper surface of the earth model. Non-reflecting conditions along the other three edges of the two-dimensional earth model are created using the boundary conditions of Cerjan *et al.* (1985). A causal, mixed-phase pulse (the derivative of a Gaussian pulse) with a dominant frequency of 90 Hz is used to approximate an explosive seismic source.

Acquisition of the synthetic seismic data involves computing vertical- and inline-component shot records at regular intervals along the specified earth model. The resultant P and PS seismic sections are produced using approximately the same processing sequences required to process real multi-component data. This helps ensure that synthetic data trials highlight issues relevant to our real-data experiments.